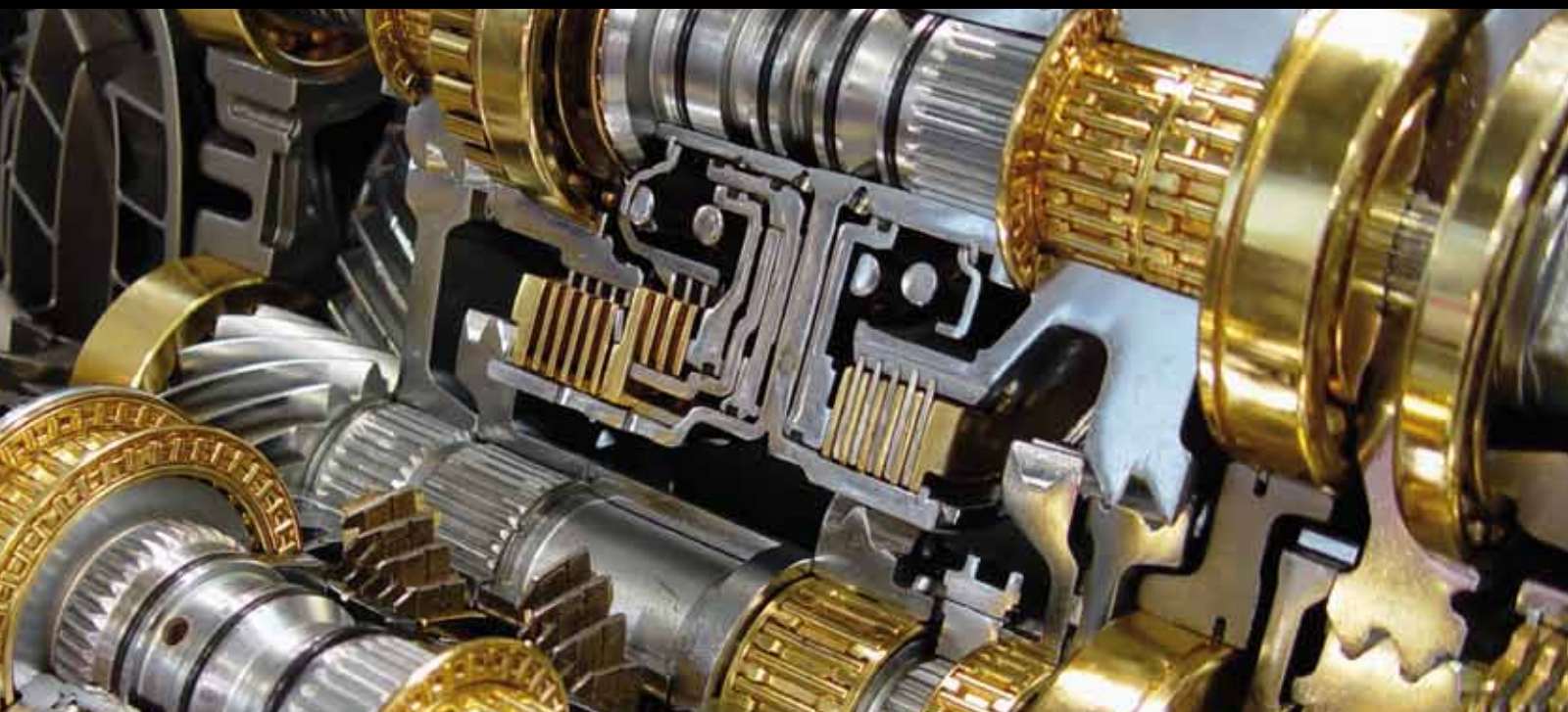


HEAT TRANSFER IN NANOFUIDS 2012

GUEST EDITORS: YOGESH JALURIA, ORONZIO MANCA, DIMOS POULIKAKOS,
KAMBIZ VAFAI, AND LIQIU WANG





Heat Transfer in Nanofluids 2012

Advances in Mechanical Engineering

Heat Transfer in Nanofluids 2012

Guest Editors: Yogesh Jaluria, Oronzio Manca,
Dimos Poulikakos, Kambiz Vafai, and Liqiu Wang



Copyright © 2012 Hindawi Publishing Corporation. All rights reserved.

This is a special issue published in "Advances in Mechanical Engineering." All articles are open access articles distributed under the Creative Commons Attribution License, which permits unrestricted use, distribution, and reproduction in any medium, provided the original work is properly cited.

Editorial Board

Koshi Adachi, Japan
Mehdi Ahmadian, USA
Rehan Ahmed, UK
Claude Bathias, France
Adib Becker, UK
Leonardo Bertini, Italy
L. A. Blunt, UK
Marco Ceccarelli, Italy
Hyung Cho, Republic of Korea
Seung Bok Choi, Korea
Bogdan I. Epureanu, USA
M. R. Eslami, Iran
A. Faghri, USA
Ali Fatemi, USA
Siegfried Fouvry, France
Ian Frigaard, Canada
M. I. Friswell, UK
Yuebin Guo, USA
Zhen Huang, China
Thomas H. Hyde, UK

Jiin Yuh Jang, Taiwan
Zhongmin Jin, UK
Essam Eldin Khalil, Egypt
Xianwen Kong, UK
Jaw-Ren Lin, Taiwan
Cheng-Xian Lin, USA
Oronzio Manca, Italy
Aristide F. Massardo, Italy
Kim Choon Ng, Singapore
C. T. Nguyen, Canada
Hiroshi Noguchi, Japan
Andrew Ooi, Australia
Hakan F. Oztop, Turkey
Duc Truong Pham, UK
Homer Rahnejat, UK
S. Rakheja, Canada
John E. Renaud, USA
Robert L. Reuben, UK
Bidyut Baran Saha, Singapore
Dik Schipper, The Netherlands

Steven R. Schmid, USA
A. Seshadri Sekhar, India
C. S. Shin, Taiwan
Yung C. Shin, USA
Ray W. Snidle, UK
Christian Soize, France
Margaret M. Stack, UK
Neil Stephen, UK
Kumar K. Tamma, USA
Yaya Tan, China
Cho W. Solomon To, USA
Yoshihiro Tomita, Japan
Shandong Tu, China
Moran Wang, USA
Fengfeng Xi, Canada
Hiroshi Yabuno, Japan
Wei Mon Yan, Taiwan
Byeng D. Youn, USA
Zhongrong Zhou, China

Contents

Heat Transfer in Nanofluids 2012, Yogesh Jaluria, Oronzio Manca, Dimos Poulikakos, Kambiz Vafai, and Liqiu Wang

Volume 2012, Article ID 972973, 2 pages

Molecular Dynamics Simulations of Pressure-Driven Flows and Comparison with Acceleration-Driven Flows, Quy Dong To, Thanh Tung Pham, Guy Lauriat, and Céline Léonard

Volume 2012, Article ID 580763, 10 pages

Measurement and Model Validation of Nanofluid Specific Heat Capacity with Differential Scanning Calorimetry, Harry O'Hanley, Jacopo Buongiorno, Thomas McKrell, and Lin-wen Hu

Volume 2012, Article ID 181079, 6 pages

Experimental Study of the Freezing Point of γ -Al₂O₃/Water Nanofluid, Thierry Maré, Ousmane Sow, Salma Halelfadl, Sylvain Lebourlout, and Cong Tam Nguyen

Volume 2012, Article ID 162961, 7 pages

Numerical Investigation on Mixed Convection in Triangular Cross-Section Ducts with Nanofluids,

Oronzio Manca, Sergio Nardini, Daniele Ricci, and Salvatore Tamburrino

Volume 2012, Article ID 139370, 13 pages

Water-Based Fe₂O₃ Nanofluid Characterization: Thermal Conductivity and Viscosity Measurements and Correlation, L. Colla, L. Fedele, M. Scattolini, and S. Bobbo

Volume 2012, Article ID 674947, 8 pages

Numerical Study of Laminar Confined Impinging Slot Jets with Nanofluids, Giuseppe Di Lorenzo, Oronzio Manca, Sergio Nardini, and Daniele Ricci

Volume 2012, Article ID 248795, 15 pages

Remarks on Constitutive Modeling of Nanofluids, Mehrdad Massoudi and Tran X. Phuoc

Volume 2012, Article ID 927580, 6 pages

Natural Convection of Nanofluids in a Square Enclosure with a Protruding Heater, J. Guet, M. Reggio, and P. Vasseur

Volume 2012, Article ID 167296, 11 pages

Editorial

Heat Transfer in Nanofluids 2012

Yogesh Jaluria,¹ Oronzio Manca,² Dimos Poulikakos,³ Kambiz Vafai,⁴ and Liqiu Wang⁵

¹ School of Engineering, Rutgers, The State University of New Jersey, 98 Brett Road, Piscataway, NJ 08854-8058, USA

² Dipartimento di Ingegneria Aerospaziale e Meccanica, Seconda Università degli Studi di Napoli, Viale Beneduce 10, Via Roma 29, 81031 Aversa, Italy

³ Laboratory of Thermodynamics in Emerging Technologies, Swiss Federal Institute of Technology, 8092 Zurich, Switzerland

⁴ Department of Mechanical Engineering, University of California, Riverside, A363 Bourns Hall, Riverside, CA 92521-0425, USA

⁵ Department of Mechanical Engineering, The University of Hong Kong, Pokfulam Road, Hong Kong

Correspondence should be addressed to Oronzio Manca, oronzio.manca@unina2.it

Received 9 February 2012; Accepted 9 February 2012

Copyright © 2012 Yogesh Jaluria et al. This is an open access article distributed under the Creative Commons Attribution License, which permits unrestricted use, distribution, and reproduction in any medium, provided the original work is properly cited.

Heat transfer enhancement determines the need for new and innovative coolants with improved performance. The novel concept of “nanofluids” has been proposed as a route to surpassing the performance of heat transfer fluids currently available. These heat exchange fluids present interesting heat transfer features compared to more conventional coolants. There is considerable research on the superior heat transfer properties of nanofluids especially on thermal conductivity and convective heat transfer. Nowadays, a fast growth of research activity in this heat transfer area has arisen. In fact, applications of nanofluids in industries such as heat exchanging devices appear promising with these characteristics. Several reviews, surveys, [1, 2] and benchmarks [3–5] and critical synthesis [5] on nanofluids with respect to thermal and rheological properties, different modes of heat transfer including boiling and on their development and applications [6–8] have been reported. However, it should be underlined that nanofluids present several factors such as long-term stability, higher pumping power and pressure drop, their thermal performance in turbulent flow and fully developed region, lower specific heat of nanofluids, and higher production cost. Moreover, the study in nanofluids involves different scales from the molecular scale to the system-scale.

The fast growth of research activity in this heat transfer area is significantly increasing. In fact, the exponential increase in the number of research articles dedicated to this subject thus far shows a noticeable growth and the importance of heat transfer enhancement technology in general. Just to give some recent data, the number of papers from 1993 to 2012 (up to January) found in SCOPUS under

“Nanofluids,” “Nanofluids AND Heat Transfer” and “Nanofluids AND Properties” is reported in Figure 1. Moreover, in SCOPUS under “Nanofluids and Review” about 87 papers were given as result. The data confirms the intensive interest and activity in research and engineering applications of nanofluids.

The aim of this special issue is to collect basic, applied and review articles on the most recent developments and research efforts in this field, with the purpose of providing guidelines for future research directions. The issue includes with experimental investigations on thermophysical properties measurements and numerical studies on convective heat transfer. A robust experimental methodology for measuring the heat capacity of nanofluids is presented and employed to measure the property of two nanofluids by H. O’Hanley et al. An experimental measurement of thermal conductivity and dynamic viscosity of water-based nanofluids containing iron oxide is presented by L. Colla et al. The freezing point measurements to study the supercooling point made of alumina is performed by T. Maré et al. A constitutive modeling of the stress tensor for nanofluids containing multi-walled carbon nanotubes is proposed by M. Massoudi and T. Phuoc. A molecular dynamics method for simulating pressure-driven flows in channels is discussed by Q. Y. To et al. A numerical investigation is made based on the lattice Boltzmann method to solve natural convection from a protruding heater located at the bottom of a square cavity by J. Quiet et al. The heat transfer in a confined impinging slot jet and the effect of buoyancy in forced convection in a duct with triangular cross section in water/alumina nanofluids are

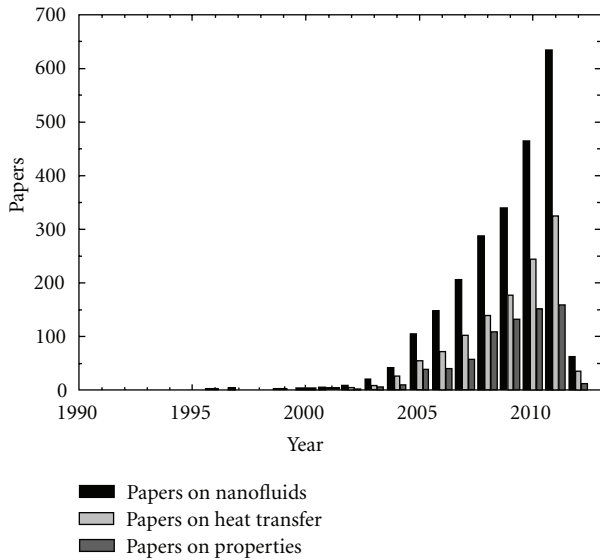


FIGURE 1: Number of papers published on nanofluids, heat transfer in nanofluids, and nanofluids properties.

studied numerically employing a single-phase model by G. Di Lorenzo et al. and O. Manca et al.

The present volume is the second special issue on heat transfer in nanofluids and we hope that it may be the beginning of a series that will periodically stimulate researchers to publish the highlights and original articles reporting how nanofluids bring new advances to heat transfer engineering.

Yogesh Jaluria
Oronzio Manca
Dimos Poulikakos
Kambiz Vafai
Liqiu Wang

References

- [1] A. Ghadimi, R. Saidur, and H. S. C. Metselaar, "A review of nanofluid stability properties and characterization in stationary conditions," *International Journal of Heat and Mass Transfer*, vol. 54, no. 17-18, pp. 4051–4068, 2011.
- [2] I. M. Mahbubul, R. Saidur, and M. A. Amalina, "Latest developments on the viscosity of nanofluids," *International Journal of Heat and Mass Transfer*, vol. 55, no. 4, pp. 874–885, 2012.
- [3] J. Buongiorno, D. C. Venerus, N. Prabhat et al., "A benchmark study on the thermal conductivity of nanofluids," *Journal of Applied Physics*, vol. 106, no. 9, Article ID 094312, 2009.
- [4] D. C. Venerus, J. Buongiorno, R. Christianson et al., "Viscosity measurements on colloidal dispersions (Nanofluids) for heat transfer applications," *Applied Rheology*, vol. 20, Article ID 44582, 2010.
- [5] K. Khanafer and K. Vafai, "A critical synthesis of thermophysical characteristics of nanofluids," *International Journal of Heat and Mass Transfer*, vol. 54, no. 19-20, pp. 4410–4428, 2011.
- [6] L. Q. Wang and J. Fan, "Nanofluids research: key issues," *Nanoscale Research Letters*, vol. 5, no. 8, pp. 1241–1252, 2010.
- [7] S. M. S. Murshed, C. A. N. D. Castro, M. J. V. Loureno, M. L. M. Lopes, and F. J. V. Santos, "A review of boiling and convective heat transfer with nanofluids," *Renewable and Sustainable Energy Reviews*, vol. 15, no. 5, pp. 2342–2354, 2011.
- [8] R. Saidur, K. Y. Leong, and H. A. Mohammad, "A review on applications and challenges of nanofluids," *Renewable and Sustainable Energy Reviews*, vol. 15, no. 3, pp. 1646–1668, 2011.

Research Article

Molecular Dynamics Simulations of Pressure-Driven Flows and Comparison with Acceleration-Driven Flows

Quy Dong To, Thanh Tung Pham, Guy Lauriat, and Céline Léonard

Laboratoire Modélisation et Simulation Multi Echelle, UMR-CNRS 8208, Université Paris-Est, 5 boulevard Descartes, 77454 Marne-la-Vallée Cedex 2, France

Correspondence should be addressed to Guy Lauriat, lauriat@univ-mlv.fr

Received 1 July 2011; Revised 6 December 2011; Accepted 15 December 2011

Academic Editor: Yogesh Jaluria

Copyright © 2012 Quy Dong To et al. This is an open access article distributed under the Creative Commons Attribution License, which permits unrestricted use, distribution, and reproduction in any medium, provided the original work is properly cited.

We use molecular dynamics to simulate fluid flows between two parallel plates with constant wall temperature. Unlike the usual approach in molecular dynamics, instead of applying an external force on the molecules, the periodic boundary conditions are modified to create a pressure difference between the inlet and the outlet sections of the computational domain. The simulation results include velocity, pressure, density, and temperature profiles obtained by the new method. These results are compared with approximate solutions for nonisothermal Poiseuille flows. The method is also applied to simulate a flow in a rib-roughened channel.

1. Introduction

Over the past decades, nano/microfluidic systems have seen a rapid development and contribute to a revolution in many areas such as biotechnology and medicines. At the same time, calculation methods are also needed to analyze the reliability of the systems. The main challenge of the nano/microfluidics computations is that the studied system has a considerable surface/volume ratio so that the surface phenomena become highly important. These size effects cannot be solved by the traditional computational method for fluid dynamics.

Depending on the nature of the problem, there are different suitable computational methods, such as those based on the Navier-Stokes and energy equations, the Burnett or super-Burnett models [1–3], and the direct simulation Monte Carlo methods [4]. For nanoflows, the molecular dynamics (MD) method is one of the most accurate methods since realistic interactions between particles or between particles and boundaries may be accounted for.

One of the fundamental and practical problems in fluid mechanics is the steady-state flow between two parallel plates, the plane Poiseuille flow. Under the incompressibility assumption, the problem has a straightforward analytical solution. It is also studied extensively by other methods (Karniadakis et al. [5]). Most of the molecular dynamic

simulations reported in the literature ([6–9], e.g.) concern flows driven by acceleration body force, rather than pressure driven flow. These limitations are due to the usage of the periodic boundary conditions which cannot generate pressure gradient inside the simulation domain. Several authors (Lupkowski and Van Swol [10], Li et al. [11], and Sun and Ebner [12]) have developed new techniques to mimic flows induced by pressure difference. Lupkowski and Van Swol [10] placed two rigid walls at the inlet and outlet and applied external forces on them. Li et al. [11] used a fictitious membrane which allows atoms to pass from one direction and forces atoms from the other direction to be elastically reflected with a given probability. Sun and Ebner [12] simulated 2D fluid flows in a long box while controlling the temperature at the two ends.

The present paper aims at presenting a new molecular dynamics approach based on pressure differences. Section 2 gives the problem statement and presents some approximate analytical solutions reported in the archival literature for Poiseuille flows. The pressure expression and the pressure difference from the atomistic point of view are also discussed. Section 3 is focused on the implementation of periodic boundary conditions linked to the pressure difference concept and its implementation in an MD code. The results of

simulations are then compared with approximate analytical solutions of the Navier-Stokes and energy equations in Section 4. The application of the present method to fluids other than ideal gases and to rib-roughened channels is also discussed. Finally, some conclusions and perspectives are given in Section 5.

2. Problem Description and Theoretical Background

2.1. Problem Description. The objective of the present work is to study the fluid flows through a nanochannel. In the cartesian coordinate system $Oxyz$, we assume that the flow direction is along the x -axis. The length, width, and height of the channel are denoted by L , B , and H in directions x , y , and z , respectively. The channel width B being very large with respect to the other dimensions, it will be treated as infinite. To produce a fluid flow from the inlet to the outlet, we keep the inlet pressure p_i at higher level than the outlet p_o . The fluid can exchange energy with the channel walls which are maintained at constant temperature, T_w .

The Knudsen number, Kn , is a quantity to identify the fluid flow regime: from continuum (small Kn) to molecular flow regime (high Kn). The range of Kn chosen in the present study, $0.02 \leq Kn \leq 0.1$, belongs to the slip flow regime according to [5], that is, the fluid continuum mechanics is still useful provided that slip boundary conditions are applied at the walls. The validity of the Navier-Stokes equations, as shown by many authors (see [7], e.g.), can therefore be extended to Poiseuille and Couette flows for the present range of Kn . The Knudsen number is defined as

$$Kn = \frac{\lambda}{H}, \quad (1)$$

where λ is the mean free path, and H is a characteristic scale of the channel. In this work, λ is estimated by

$$\lambda = \frac{1}{\sqrt{2}n\pi\sigma^2}. \quad (2)$$

The quantities n and σ in (2) are the density number and the diameter of the fluid molecules, respectively. For Lennard Jones (LJ) fluids, the molecular diameter value σ is approximately taken equal to the σ parameter appearing in the LJ potential formula introduced in Section 4.1.

In what follows, the terms ‘‘pressure-driven flow’’ and ‘‘acceleration-driven flow’’ are employed to define two particular cases: (i) the body force $\rho\gamma$ applied on a unit fluid volume is zero, and the pressure p decreases along the flow direction, $\rho\gamma = 0$, $dp/dx \neq 0$; (ii) the inverse situation where $\rho\gamma \neq 0$, $dp/dx = 0$. We shall also consider some available analytical solutions of the Navier-Stokes equations reported in the literature. For both flows, the fluid velocity v in a cross-section which accounts for slip effects (Navier boundary conditions) at the wall admits the parabolic form

$$v(\hat{z}) = v(0)[1 - a_2\hat{z}^2], \quad \hat{z} = \frac{z}{H}, \quad (3)$$

where a_2 is a positive dimensionless constant related to pressure gradient (or body force), viscosity, slip length,

and so forth. It is noted that (3) is generally obtained for incompressible fluids, but it is also valid for compressible fluid flows in a long channel [13]. In the latter case, v and a_2 are functions of the streamwise coordinate x .

An approximation solution of the energy equation can be obtained by neglecting the convective term [14]. The temperature T becomes then a quartic function of the coordinate z ,

$$T(z) = T_w[b_0 - b_4\hat{z}^4]. \quad (4)$$

Equation (4) is based on the incompressibility assumption. For compressible fluid flows in a long channel, Cai et al. [15] used a perturbation technique to derive the following temperature distribution:

$$T(x, z) = T_w[c_0 - c_2\hat{z}^2 - c_4\hat{z}^4]. \quad (5)$$

The dimensionless coefficients c_i, b_i in (4) and (5) are related to pressure gradient (or body force), viscosity, conductivity, specific heat, and so forth. In (5), the coefficients c_i depend on the position x . We also note that for acceleration-driven flow, Todd and Evans [6] suggested a correction to the temperature profile given by (4) as a sextic function of z ,

$$T(z) = T_w[d_0 - d_2\hat{z}^2 - d_4\hat{z}^4 - d_6\hat{z}^6]. \quad (6)$$

In Section 4, MD simulations are used to reexamine the validity of the velocity and temperature profiles given by (3)–(6) and to determine the coefficients a_i, b_i, c_i , and d_i by curve fitting.

2.2. Pressure Tensor and Pressure Difference. Before proceeding the molecular dynamics simulation, let us look at the definition of pressure tensor from the atomistic point of view. Using statistical mechanic theory, Irving and Kirkwood [16] derived the following pressure tensor decomposition (IK):

$$\mathbf{P} = \mathbf{P}_K + \mathbf{P}_V. \quad (7)$$

The kinetic term \mathbf{P}_K depends on the molecular square velocity, while the potential term \mathbf{P}_V depends on pairwise interactions between molecules. In a system of N molecules, \mathbf{P}_K and \mathbf{P}_V read

$$\begin{aligned} \mathbf{P}_K(\mathbf{r}) &= \sum_{i=1}^N \langle m(\mathbf{v}_i - \bar{\mathbf{v}}) \otimes (\mathbf{v}_i - \bar{\mathbf{v}}) \delta(\mathbf{r}_i - \mathbf{r}) \rangle, \\ \mathbf{P}_V(\mathbf{r}) &= -\frac{1}{2} \sum_i^N \sum_{j \neq i}^N \langle \mathbf{r}^{(ij)} \otimes \mathbf{f}^{(ij)} O_{ij} \delta(\mathbf{r}_i - \mathbf{r}) \rangle. \end{aligned} \quad (8)$$

The term inside the angular bracket $\langle \cdot \rangle$ denotes the ensemble average, and \otimes denotes the dyadic product. The terms \mathbf{r}_i , \mathbf{v}_i , and $\bar{\mathbf{v}}$ are respectively the position vector, the velocity of the particle i , and the mean velocity. The distance vector and interaction force vector between two molecules (i) and (j) are denoted, respectively, as $\mathbf{r}^{(ij)}$ and $\mathbf{f}^{(ij)}$. For LJ fluids, the two vectors $\mathbf{r}^{(ij)}$ and $\mathbf{f}^{(ij)}$ are colinear, and the force magnitude $f^{(ij)}$ is derived from the interaction potential in function of the distance between the two molecules

$$\mathbf{f}^{(ij)} = \frac{\partial \mathcal{V}(r^{(ij)})}{\partial \mathbf{r}^{(ij)}}, \quad r^{(ij)} = \|\mathbf{r}_i - \mathbf{r}_j\|. \quad (9)$$

In (8), the notation $\delta(\mathbf{r}_i - \mathbf{r})$ is used for the delta Dirac function at \mathbf{r}_i , and the expression of the operator O_{ij} reads

$$O_{ij} = 1 - \frac{1}{2!} \mathbf{r}^{(ij)} \frac{\partial}{\partial \mathbf{r}} + \dots + \frac{1}{n!} \left[-\mathbf{r}^{(ij)} \frac{\partial}{\partial \mathbf{r}} \right]^{n-1} + \dots \quad (10)$$

Equations (10) and (8) show that the derivation of IK pressure tensor involves an infinite sum of high-order derivatives of the delta function and ensemble average, not suitable for MD computations. A more convenient form of the pressure tensor and an associated calculation method, the method of plane (MOP), was proposed by Todd et al. [17] and by Evans and Morriss [18]. When the fluid density is uniform, the operator O_{ij} is reduced to unity, and (8) becomes (see [17, 19–22])

$$\begin{aligned} \mathbf{P}_K(\mathbf{r}) &= \frac{1}{V} \sum_i m(\mathbf{v}_i - \bar{\mathbf{v}}) \otimes (\mathbf{v}_i - \bar{\mathbf{v}}), \\ \mathbf{P}_V(\mathbf{r}) &= -\frac{1}{V} \sum_{i < j} \mathbf{r}^{(ij)} \otimes \mathbf{f}^{(ij)}, \end{aligned} \quad (11)$$

where V is the volume of the fluid element located at \mathbf{r} . In the literature, (11) is sometimes referred to as IK1 pressure [17, 18]. In (8) and (11), the pressure can be decomposed into two scalar quantities p_K and p_V as follows:

$$p = p_K + p_V, \quad p_K = \frac{1}{3} \text{tr} \mathbf{P}_K, \quad p_V = \frac{1}{3} \text{tr} \mathbf{P}_V. \quad (12)$$

It is clear that for low-density fluids, high temperature, and small interaction energy ϵ , the pressure is reduced to the kinetic part p_K , as for ideal gases. For the other fluids, the potential part p_V cannot be neglected. The pressure difference Δp between two points at distance Δl reads

$$\Delta p = \Delta p_K + \Delta p_V = k_B \Delta(nT) + \Delta p_V. \quad (13)$$

The pressure components P_{xx} , P_{yy} , P_{zz} , number density n , and stream velocity $\bar{\mathbf{v}}$ are invariant in direction y . From a microscopic point of view, taking $\Delta l = \Delta y$, we must have

$$\begin{aligned} \Delta \langle v_x^2 \rangle &= \Delta \langle v_y^2 \rangle = \Delta \langle v_z^2 \rangle = 0, \\ \Delta \langle v_x \rangle &= \Delta \langle v_y \rangle = \Delta \langle v_z \rangle = 0. \end{aligned} \quad (14)$$

As it will be discussed in the following, all these conditions are satisfied in our MD simulation algorithm if we apply periodicity for the boundary conditions in the y direction. However, n , p , and T can all vary in the flow direction x . We note that in the steady-state regime, all quantities like T , p , p_V , and n are stable with time, and thus their differences ΔT , Δp , Δp_V , and Δn are also stable. In particular, (13) shows that the finite variation of temperature ΔT along x is related to those of other quantities via the expression

$$\Delta T = \frac{\Delta p - \Delta p_V - k_B T \Delta n}{k_B n + k_B \Delta n}. \quad (15)$$

If the stream velocity is much smaller than the thermal velocity, we can obtain a simplified expression for the temperature difference as

$$\Delta T = \frac{m}{3k_B} \Delta \langle \mathbf{v}^2 - \bar{\mathbf{v}}^2 \rangle \simeq \frac{m}{3k_B} \Delta \langle \mathbf{v}^2 \rangle. \quad (16)$$

The objective of the MD method discussed in what follows is to maintain the differences in squared velocity and, thus in temperature, in direction x . By that way, we can indirectly generate the pressure difference Δp . In the case where density ρ is invariant in x -direction (incompressible flow assumption), the temperature difference is proportional, for an ideal gas, to the pressure difference since

$$\Delta p = \frac{\rho}{3} \Delta \langle v^2 \rangle \quad (17)$$

3. Numerical Procedure

In molecular dynamics, periodic boundary conditions (PBC) applied to velocities are powerful techniques to reduce the study of a large system to a smaller one far from the edge. Considering a simulation domain as a cube, PBC requires that if a molecule passes through one face, it reappears on the opposite face with the same velocity. Obviously, there is no difference in pressure, density, or temperature between any two opposite faces of the simulation domain. Consequently $\Delta p = 0$, as it will be shown in the next section.

3.1. Modified Periodical Boundary Conditions. In our problem, all the virial pressure components P_{xx} , P_{yy} , and P_{zz} do not vary along y , which can be satisfied by the traditional PBC applied on the faces $y = \pm B/2$. However, to create a pressure difference along the x -axis, we must develop a strategy that produces a constant difference between the squared velocity of the molecules crossing the face $x = 0$ and those crossing the face $x = L$.

Usually, to keep unchanged the total number of molecules in the domain whenever a molecule goes out of the domain, we must insert another molecule inside. Thus, if we relax the PBC constraints, there are many ways to assign velocities to ingoing molecules, either independent of or dependent on the outgoing ones. In this paper, we generalize the PBC to account for the pressure difference by maintaining the difference in squared velocity at the two opposite faces $x = 0$ and $x = L$.

From (15) and (16), we know that a constant pressure difference is related to a constant difference in squared velocity. A constant parameter δ is thus used to create a constant difference in squared velocity between the inlet and outlet faces (see Figure 1). In order to apply a velocity square difference equal to a constant $3\delta L$ between the faces $x = 0$ and $x = L$, we modify the periodic boundary conditions so that if a molecule goes through the face $x = L$ with a velocity \mathbf{v} , we insert a molecule at $x = 0$ with a velocity \mathbf{v}' satisfying the following conditions:

$$\mathbf{v}' = \alpha \mathbf{v}, \quad \alpha = \sqrt{1 + \frac{3\delta L}{v^2}}. \quad (18)$$

Analogously, if a molecule crosses the face $x = 0$ with a velocity \mathbf{v} , it reappears at $x = L$ with a velocity \mathbf{v}' so that

$$\mathbf{v}' = \alpha \mathbf{v}, \quad \alpha = \sqrt{1 - \frac{3\delta L}{v^2}}. \quad (19)$$

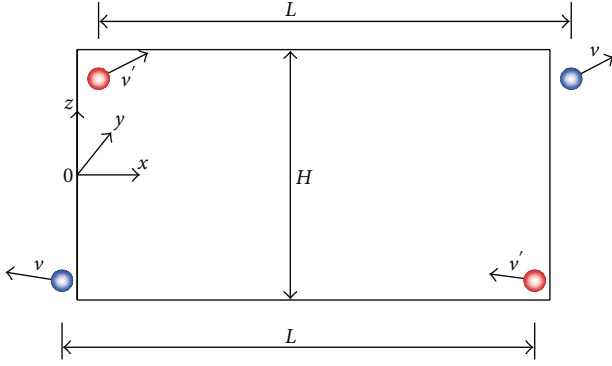


FIGURE 1: Modified periodic boundary conditions. The velocity v between the outgoing molecules is different from the ingoing molecules ((18) and (19)).

TABLE 1: Summary of the boundary conditions applied on the simulation domain.

	Boundary conditions
Faces x	Equations (18)-(19)
Faces y	PBC
Faces z	Thermal walls

Since $3\delta L$ is positive, it may happen that $v^2 - 3\delta L < 0$. It is then impossible to find v' satisfying (19). The boundary conditions applied to the simulation domain are summarized in Table 1. However, this effect can be assumed negligible for flows with relatively small speed (of the order 1% of the thermal speed), as seen in most MEMS/NEMS devices. In the present simulations, the number of molecules that do not satisfy (19) were found less than 1% of the outgoing molecules. In order to simulate low-speed flows, small values of δ were used.

4. Results

4.1. *Molecular Dynamic Simulations of Ideal Gas Flows.* To model the interaction between the molecules, the 6–12 Lennard Jones potential is used

$$\mathcal{V}(r) = 4\epsilon \left[\left(\frac{\sigma}{r} \right)^{12} - \left(\frac{\sigma}{r} \right)^6 \right], \quad (20)$$

where ϵ is the depth of the potential well, σ is the finite distance at which the interparticle potential is zero, and r is the distance between the particles.

The potential well depth parameter is $\epsilon = 0.1\epsilon_0$ with ϵ_0 being the reference potential well depth. Two cutoff distances were used in this study: $r_c = 2^{1/6}\sigma$ [17] corresponds to repulsive interactions between molecules, while $r_c = 2.5\sigma$ [21, 23–25] corresponds to attractive-repulsive interactions. In general, the present method is valid for any pair potential. However, the simulation conditions of Table 2, that is, ($\epsilon = 0.1\epsilon_0$, $r_c = 2^{1/6}\sigma$), lead to a very small potential part of the pressure p_V (less than 1% of the kinetic part p_K) making the behavior of the fluid close to an ideal gas.

TABLE 2: Input data for the first series of MD simulations.

N	L [σ]	B [σ]	H [σ]	Kn	δ [$\epsilon_0/m\sigma$]	γ [$\epsilon_0/m\sigma$]
2400	86.2	6.5	43.1	0.05	10^{-3}	4.3×10^{-4}
600	43.1	6.5	21.5	0.1	2×10^{-3}	8.6×10^{-4}

(ϵ, r_c) = ($0.1\epsilon_0, 2^{1/6}\sigma$), $\bar{n} = 0.1\sigma^{-3}$, and $T = 2\epsilon_0/k_B$.

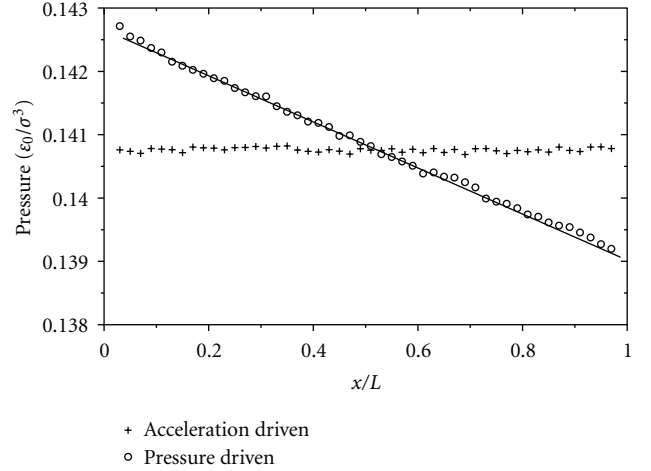


FIGURE 2: Pressure distribution ($\bar{p}(x)$) along the channel for pressure-driven flow case and acceleration-driven flow case (Kn = 0.05, $r_c = 2^{1/6}\sigma$, $\epsilon = 0.1\epsilon_0$, $\delta = 10^{-3}\epsilon_0/m\sigma$, and $\gamma = 4.3 \times 10^{-4}\epsilon_0/m\sigma$). The full line represents the linear fit and is used to determine the pressure gradient $\Delta p/\Delta x$. The pressure unit is [ϵ_0/σ^3].

The two walls are modeled as thermally diffusive walls at the same and constant temperature. Whenever a molecule arrives at a wall, it is reflected with the velocity corresponding to the wall temperature $T_w = 2\epsilon_0/k_B$ and with a random direction. In this work, we do not use thermostats, and the fluid can exchange energy with the wall due to the wall model used here.

In our simulations, the global number density \bar{n} is kept fixed, $\bar{n} = 0.1\sigma^{-3}$ in every configurations. Other geometric parameters like L , B , H , and the number of the molecules N are changed as shown in Table 2. The values of δ are chosen such that the difference of the square of the molecular velocity between the inlet and outlet is small enough so that the stream velocity is much smaller than the thermal speed. From the microscopic viewpoint, the local stream velocity is the local average velocity of the molecules, and from the macroscopic viewpoint, it is the flow speed v in the Navier-Stokes equations and thus connected to the pressure gradient ∇p (or volume force $\rho\gamma$). On the other hand, the thermal speed is the root mean square of the molecular velocity and is directly connected to the local temperature T . The slope of the simulated total pressure distribution along the channel (see Figures 2 and 3) is used to determine the pressure gradient $-\Delta p/\Delta x$ and the equivalent external acceleration $\bar{\rho}\gamma$ used in the acceleration-driven flow simulations. The quantity $\bar{\rho}$ is the average mass density of the system, $\bar{\rho} = m\bar{n}$.

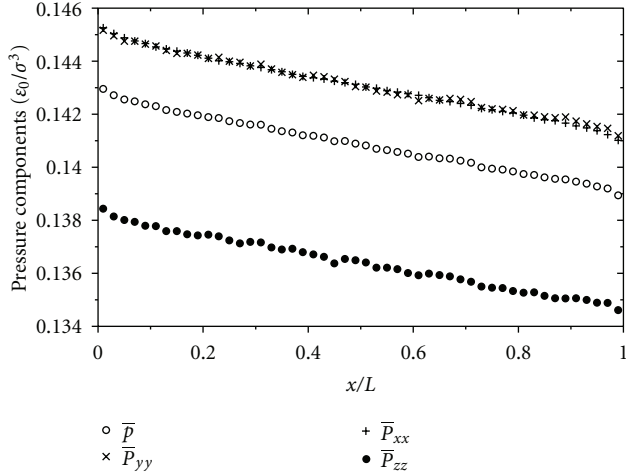


FIGURE 3: Distribution of pressure $\bar{p}(x)$ and pressure components $\bar{P}_{xx}(x)$, $\bar{P}_{yy}(x)$, and $\bar{P}_{zz}(x)$ along the channel for pressure-driven flow case ($\text{Kn} = 0.05$, $r_c = 2^{1/6}\sigma$, $\epsilon = 0.1\epsilon_0$, and $\delta = 10^{-3}\epsilon_0/m\sigma$). The pressure unit is $[\epsilon_0/\sigma^3]$.

The computation with Leap-Frog Verlet integration scheme is carried out for 10^8 time steps from equilibrium, each of which is equal to 0.005 unit time $\tau = \sqrt{m\sigma^2/\epsilon_0}$. The height and length of the channel are divided into 50 layers to determine accurately the distribution of local velocity \mathbf{v} , temperature T , and pressure tensor \mathbf{P} . The local velocity \mathbf{v} measured in one bin located at \mathbf{r} is given by

$$\mathbf{v}(\mathbf{r}) = \frac{1}{n_{\text{bin}}} \sum_{\mathbf{r}_i \in \text{bin}} \mathbf{v}_i, \quad (21)$$

n_{bin} being the particle number in the bin. The local pressure \mathbf{P} (IK1-model) is

$$\mathbf{P}(\mathbf{r}) = \frac{1}{V_{\text{bin}}} \times \left[\sum_{\mathbf{r}_i \in \text{bin}} m(\mathbf{v}_i - \bar{\mathbf{v}}) \otimes (\mathbf{v}_i - \bar{\mathbf{v}}) - \frac{1}{2} \sum_{\mathbf{r}_i \in \text{bin}} \mathbf{r}^{(ij)} \otimes \mathbf{f}^{(ij)} \right]. \quad (22)$$

The pressure components were also computed by using the method of plane [17, 26]. With α, β being x, y , or z , the pressure component $P_{\beta\alpha}$ along direction β and acting on the area element A_α normal to the axis α is defined by

$$P_{\beta\alpha}(\mathbf{r}) = \frac{1}{\tau A_\alpha} \sum_{\mathbf{r}_i \in A_\alpha} \frac{m(v_{i\beta} - \bar{v}_{i\beta})(v_{i\alpha} - \bar{v}_{i\alpha})}{v_{i\alpha}} + \frac{1}{\tau A_\alpha} \int dt \sum_{\mathbf{r}_{ij} \cap A_\alpha, i < j} f_\beta^{(ij)}. \quad (23)$$

In (23), the first sum is for all molecules crossing the area element A_α over the period τ , and the second sum is for all pairs whose distance vectors cut the area element A_α . The temperature T of one bin is then calculated by

$$T(\mathbf{r}) = \frac{m}{3k_B} \langle \|\mathbf{v} - \bar{\mathbf{v}}\|^2 \rangle_{\text{bin}}. \quad (24)$$

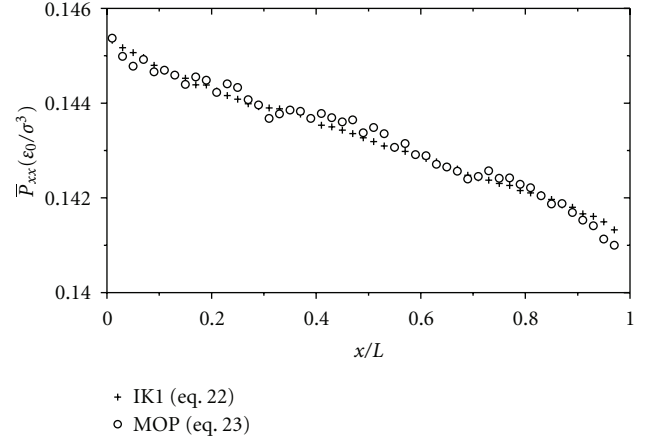


FIGURE 4: Distribution of pressure \bar{P}_{xx} along the channel for pressure-driven flow case ($\text{Kn} = 0.05$, $r_c = 2^{1/6}\sigma$, $\epsilon = 0.1\epsilon_0$, and $\delta = 10^{-3}\epsilon_0/m\sigma$) computed by (22) and (23). The pressure unit is $[\epsilon_0/\sigma^3]$.

In what follows, the x -distributions of pressure, temperature, and density correspond to an average on y and z of the local quantities $p(\mathbf{r})$ and $n(\mathbf{r})$. They are denoted as $\bar{p}(x) = \langle p(\mathbf{r}) \rangle_{y,z}$ and $\bar{n}(x) = \langle n(\mathbf{r}) \rangle_{y,z}$, respectively. Analogously, the profile along z of velocity, temperature, and density corresponds to an average on x and y of local quantities with the notations: $\bar{v}(z) = \langle v(\mathbf{r}) \rangle_{x,y}$, $\bar{T}(z) = \langle T(\mathbf{r}) \rangle_{x,y}$, and $\bar{n}(z) = \langle n(\mathbf{r}) \rangle_{x,y}$, respectively.

From the simulations, the axial pressure distribution is plotted in Figure 2 for the pressure-driven and the acceleration-driven flows with $\text{Kn} = 0.05$, $r_c = 2^{1/6}\sigma$. As expected, for the acceleration-driven flow case, the pressure is constant. In contrast, the pressure distribution for pressure-driven flow decreases linearly. We note here that the slope of the pressure curve, equal to $\Delta\bar{p}/\Delta x$, is used to compute the value γ in the acceleration flow simulation according to the formula $\gamma = -\Delta\bar{p}/(\bar{p}\Delta x)$. Under the simulation conditions $\bar{n} = 0.1\sigma^{-3}$, $T_w = 2\epsilon_0/k_B$, and $r_c = 2^{1/6}\sigma$, $\epsilon = 0.1\epsilon_0$, the kinetic part p_K of the pressure dominates.

In order to know how the pressure difference is distributed in the x -, y -, z -directions, the pressure components \bar{P}_{xx} , \bar{P}_{yy} , and \bar{P}_{zz} along x are plotted in Figure 3. All the three pressure components decrease with x , and the slopes are almost the same. The values of components \bar{P}_{xx} , \bar{P}_{yy} are very close, whereas the value of component \bar{P}_{zz} is smaller because the fluid is confined in the z -direction. Although the difference between the pressure components is small (less than 4%), it implies that the velocity distribution deviates from the equilibrium distribution. Because the pressure \bar{p} is the average value of \bar{P}_{xx} , \bar{P}_{yy} , \bar{P}_{zz} , the \bar{p} -curve lies between the others and has the same slope. It should be noted that (22) and (23) lead to relatively close results when considering the average axial pressure component \bar{P}_{xx} (see Figure 4). Figure 5 shows that the fluid density distribution $\bar{n}(z)$ across the channel width varies slightly around the average density \bar{n} , except near the walls where it can be as high as $1.4\bar{n}$. However, the phase diagram for LJ fluid [25] shows that the fluid near

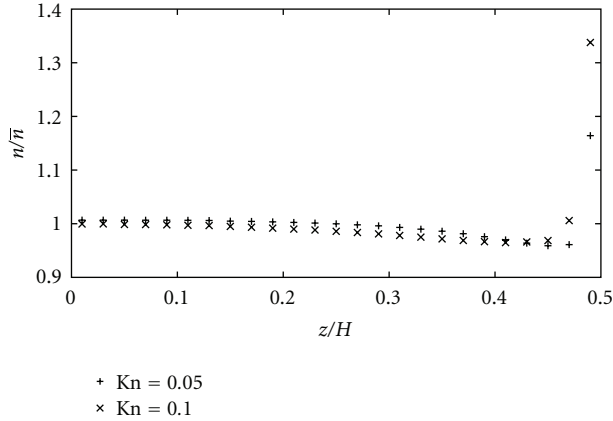


FIGURE 5: Dimensionless density profile ($\bar{n}(z)$) in half of the channel cross-section for pressure-driven simulations ($\text{Kn} = 0.05, 0.1$, $r_c = 2^{1/6}\sigma$, $\epsilon = 0.1\epsilon_0$, $\delta = 10^{-3}\epsilon_0/m\sigma$, and $2 \times 10^{-3}\epsilon_0/m\sigma$).

the wall is still in gas state. In our simulations, \bar{n} and ϵ are chosen to be very small ($\bar{n} = 0.1\sigma^{-3}$, $\epsilon = 0.1\epsilon_0$), and the fluid temperature near the wall is relatively large (the temperature of the wall is $T_w = 2\epsilon_0/k_B$). The fluctuation of the density profile shows that the incompressibility assumption is no longer valid, especially near the channel walls. However, the fluctuations being localized, it is interesting to check if the analytical solutions presented in Section 2 still agree with the MD solutions.

Figure 6 shows that acceleration and pressure-driven flows exhibit parabola-like velocity profiles in the center region of the channel, in agreement with (3). Near the wall where the Knudsen layer dominates, the velocity distribution tends to deviate from the solution given by (3), and a velocity slip at the wall is predicted. Based on the kinetic theories, different models have been derived to explain the slippage [5], and generally, the slip effect becomes important when the Knudsen number increases. The little difference in velocity profile between the two types of flow shows that, despite their different microscopic natures, volume forces can be seen as equivalent to pressure gradients at the macroscopic scale.

About the temperature profile across the channel width, there is no visible difference between acceleration and pressure-driven formulations whatever Kn (Figure 7). The temperature profile cannot be fitted by any of the three approximate analytical solutions ((4)–(6)). The temperature is minimal at the center of the channel and increases rapidly near the wall, which does not agree with the approximate solutions obtained with the incompressible assumption ((4)–(5)). With the simulation conditions reported in Table 2, this reverse trend cannot thus be explained by using the incompressible flow equations. This anomaly was also observed by using DSMC method [27] and super-Burnett (SB) method [28]. Note that the flow speeds in our simulations are very small, as in [27, 28].

Next, we study the influence of γ and δ on the temperature profile. By increasing the acceleration parameter γ or

TABLE 3: Input data for MD simulations in Section 4.2.

\bar{n} [σ^{-3}]	N	L [σ]	B [σ]	H [σ]	δ [$\epsilon_0/m\sigma$]	T_w [ϵ_0/k_B]
0.1	2400	86.2	6.5	43.1	1×10^{-3}	2
0.8	2400	86.2	3.2	43.1	1×10^{-3}	2

$$(\bar{n}, \epsilon, r_c) = (0.1\sigma^{-3}, \epsilon_0, 2.5\sigma), (0.8\sigma^{-3}, \epsilon_0, 2^{1/6}\sigma).$$

the δ -parameter (squared velocity), the stream velocity is increased. A change in the form of the temperature profile is observed in Figures 8 and 9 as γ (or δ) increases. At high values of γ (or δ), the temperature profiles seem to be closer to the approximate solutions which predict a maximum at the center of the channel and a minimum at the walls. At small values of γ (or δ), the temperature profiles for the two flow types differ just a little. However, at high values of γ (or δ), the discrepancy becomes more important: the curvature at the center of channel for the pressure-driven flow case is higher than that for the acceleration-driven flow case. Using a curve-fitting procedure, we find that the temperature profile of the pressure-driven flow case agrees quite well with the quartic expression (5). The temperature for the acceleration-driven flow case does not fit well with (4). To explain this discrepancy, Todd and Evans [6] argued that the transport coefficients are not constant and that an additional cross-coupling between strain rate and heat flux exists. They proposed a correction to (5) with a z^6 -extraterm for the temperature profile (see (6)). The dashed line drawn in Figure 9 shows that the sextic polynomial fits very well the present numerical results.

4.2. Applications to More General Cases and Rib-Roughened Channels. The application of the method to cases for which the fluid particles interact strongly, that is, the potential pressure p_V is of the order of p_K , is considered in that section. The case of rib-roughened channels is also briefly discussed.

With the algorithm developed in the previous section, two cases were considered with the same parameters, except for the cutoff distance r_c and density number \bar{n} . In the first case, $\bar{n} = 0.1\sigma^{-3}$, and the cutoff distance is set to $r_c = 2.5\sigma$ (attractive-repulsive interaction). In the second case, the fluid density is increased up to $\bar{n} = 0.8\sigma^{-3}$ while setting $r_c = 2^{1/6}\sigma$ as in the previous section. The well depths ϵ are the same in both cases and equal to the reference value, that is, $\epsilon = \epsilon_0$. All the parameters for these two cases are summarized in Table 3.

In the first case ($\bar{n} = 0.1\sigma^{-3}$), Figure 10 displays the kinetic part \bar{p}_K and the virial pressure \bar{p} according to (11) along the channel. Except a slight curvature in the \bar{p}_K curve, both pressure curves decrease continuously and linearly. The relative difference between the slopes of both curves is less than 1%, which means that the gradient of the potential part $\Delta\bar{p}_V/\Delta x$ is also small in comparison with the kinetic part $\Delta\bar{p}_K/\Delta x$ even if \bar{p}_V is not negligible ($|\bar{p}_V/\bar{p}_K| \simeq 0.2$). In the second case ($\bar{n} = 0.8\sigma^{-3}$), Figure 11 shows a totally reverse trend: both the virial pressure profile and its potential part decrease with x . The variation of the potential part

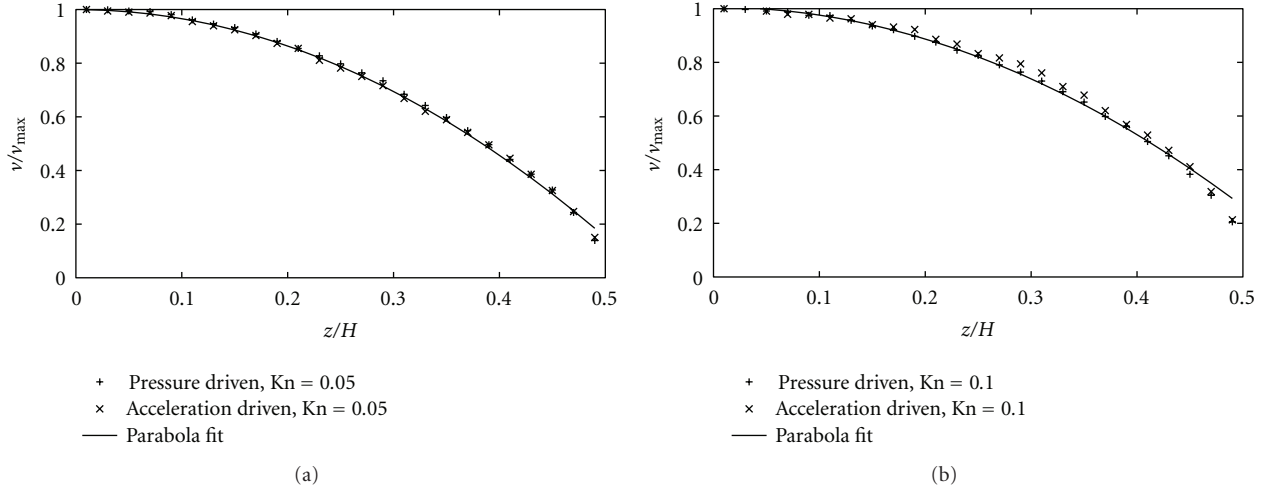


FIGURE 6: Dimensionless velocity profile in half of the channel cross-section for $\text{Kn} = 0.05$ and $\text{Kn} = 0.1$ ($r_c = 2^{1/6}\sigma$, $\epsilon = 0.1\epsilon_0$). The full lines represent equation $v(\hat{z}) = v(0)(1 - a_2\hat{z}^2)$ that best fit the numerical results ($a_2 = 0.18$ for $\text{Kn} = 0.05$ and $a_2 = 0.29$ for $\text{Kn} = 0.1$).

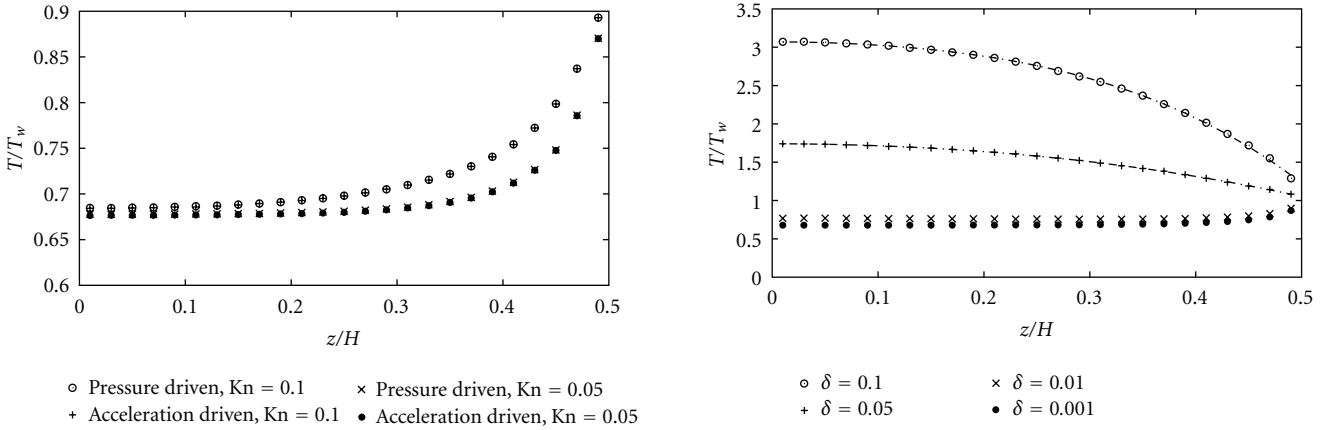


FIGURE 7: Dimensionless temperature profile ($\bar{T}(z)$) in half of the channel cross-section for two Kn values according to the flow model ($r_c = 2^{1/6}\sigma$, $\epsilon = 0.1\epsilon_0$).

FIGURE 8: Variation of temperature profile when increasing the pressure gradient or parameter δ ($\text{Kn} = 0.05$, $r_c = 2^{1/6}\sigma$, and $\epsilon = 0.1\epsilon_0$). The dashed lines are based on equation $c_0 - c_2\hat{z}^2 - c_4\hat{z}^4$ that best fits the numerical results. $c_0 = 3.07$, $c_2 = 4.16$, and $c_4 = 12.8$ for $\gamma = 0.1\epsilon_0/m\sigma$, $c_0 = 1.74$, $c_2 = 2.5$, and $c_4 = 1.0$ for $\gamma = 0.05\epsilon_0/m\sigma$.

contributes to 80% of the virial pressure variation with $\Delta\bar{p}/\Delta x = -0.0177$ and $\Delta\bar{p}_V/\Delta x = -0.0159$. We conclude that the method is convenient for generating virial pressure profiles which decrease in the axial direction.

Next, we consider the velocity profiles across the channel section for these two cases. The velocity profiles (Figure 12) agree then with (3). The slip length for the case $\bar{n} = 0.8\sigma^{-3}$ is smaller than for the case $\bar{n} = 0.1\sigma^{-3}$ because the mean free path is decreased when the density number is increased. When computing the average pressure component \bar{P}_{xx} along the channel, Figure 13 shows that there is no visible difference between (22) and (23).

It should thus be emphasized that the present method is relevant to generate various fluid flows even if we control only the difference between the inlet- and outlet-squared molecular velocities. The potential part p_V , which depends

on the interatomic interaction, can vary along the flow direction. As shown numerically, the variation of p_V contributes considerably to the pressure gradient.

The third case aimed at modeling the flow within a rib-roughened channel. The parameters are the same as in the second case ($\bar{n} = 0.8\sigma^{-3}$, $r_c = 2^{1/6}\sigma$), but the channel height is suddenly reduced in its middle part by inserting on both walls ribs of height h and length l . The rib-to-channel width ratio is equal to $h/H = 0.8$ and $l/L = 0.3$ (Figure 14). Figure 14 exhibits the onset of two vortices close to the rib corners at the upstream section. It is also shown that the fluid flow is highly nonuniform and characterized by wavy streamline patterns within the downstream region. From Figure 15, the axial pressure variations are rather different from those predicted for smooth channels. Although the

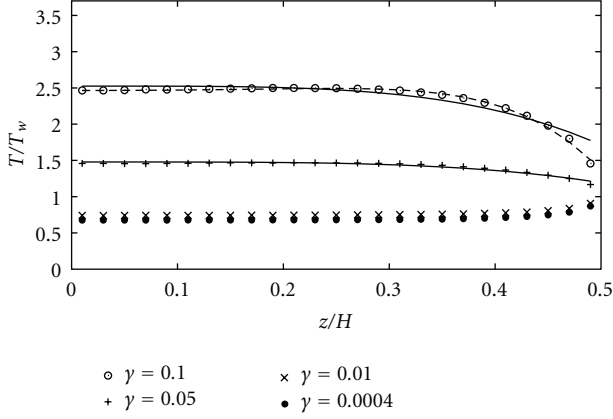


FIGURE 9: Changes in the temperature profile for various values of the acceleration parameter γ ($\text{Kn} = 0.05$, $r_c = 2^{1/6}\sigma$, and $\epsilon = 0.1\epsilon_0$). The solid and the dashed lines correspond to equations $b_0 - b_4 z^4$ and $d_0 - d_2 z^2 - d_4 z^4 - d_6 z^6$ that best fit the numerical results. $b_0 = 2.53$, $b_4 = 13.0$, $d_0 = 2.46$, $d_2 = 0.54$, $d_4 = 4.58$, and $d_6 = -97.8$ for $\gamma = 0.1\epsilon_0/m\sigma$ and $b_0 = 1.48$, $b_4 = 4.57$ for $\gamma = 0.05\epsilon_0/m\sigma$.

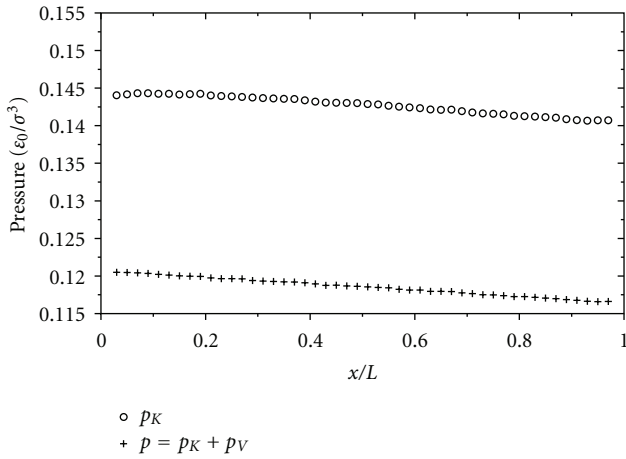


FIGURE 10: Axial variations of pressures $\bar{p}(x) = p_K + p_V$ and p_K for pressure-driven flow ($\bar{n} = 0.1\sigma^{-3}$, $r_c = 2.5\sigma$, and $\epsilon = \epsilon_0$). The pressure unit is $[\epsilon_0/\sigma^3]$.

variations of the axial pressure predicted by (22) and (23) are quite similar, there are considerable differences between them. The MOP pressure is 8% smaller than the IK1 pressure. The changes in pressure at the downstream and upstream sections display also smoother pressure variations. This considerable difference is due to the strong inhomogeneity of the fluid within the channel. Generally, the MOP, based on the hydrodynamics equation, must be used in such situation.

5. Conclusions

In this work, we have used a molecular dynamics method for simulating pressure-driven flows in channels. The main

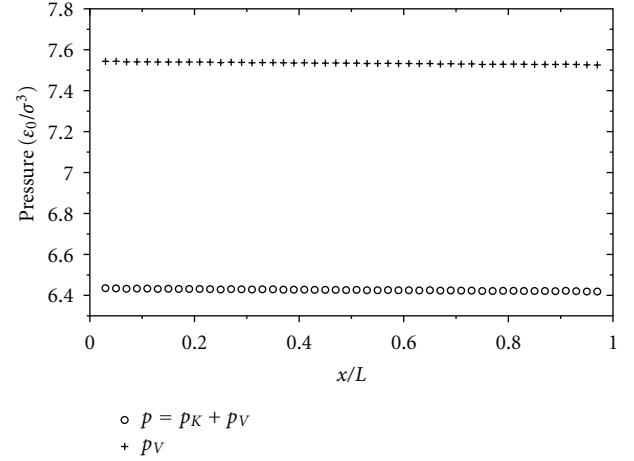


FIGURE 11: Axial variations of pressures $\bar{p}(x) = p_K + p_V$ and p_V for pressure-driven flow ($\bar{n} = 0.8\sigma^{-3}$, $r_c = 2^{1/6}\sigma$, and $\epsilon = \epsilon_0$). The pressure unit is $[\epsilon_0/\sigma^3]$.

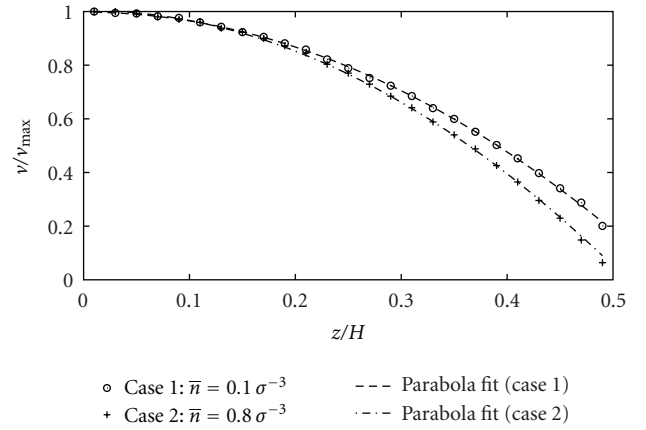


FIGURE 12: Dimensionless velocity profile in half of the channel cross-section for $\bar{n} = 0.1\sigma^{-3}$ and $\bar{n} = 0.8\sigma^{-3}$. The dashed lines represent the equations $a_0 - a_2 z^2$ that best fit the numerical results.

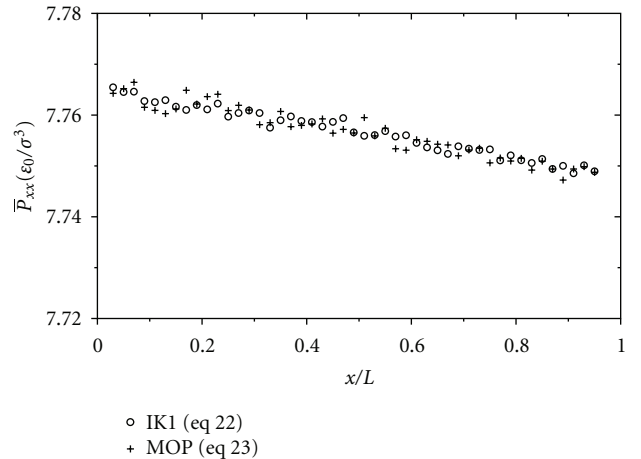


FIGURE 13: Axial variations of pressure component \bar{P}_{xx} computed by (22) and (23). The pressure unit is $[\epsilon_0/\sigma^3]$.

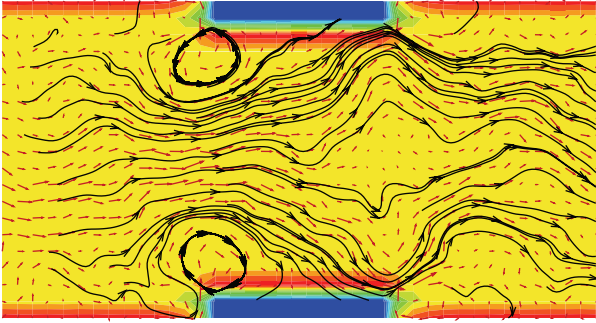


FIGURE 14: Streamlines in a rib-roughened channel. The color represents the fluid density field.

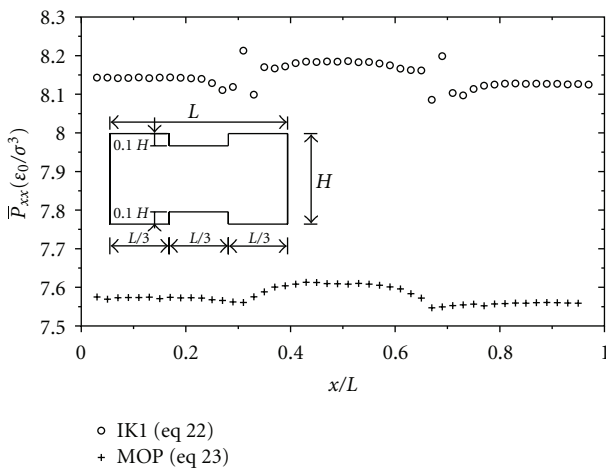


FIGURE 15: Distribution of pressure component \bar{P}_{xx} in a rib-roughened channel computed by (22) and (23). The pressure unit is $[\epsilon_0/\sigma^3]$.

novelty lies in the modification of the periodic inlet and outlet velocity conditions: the difference in squared velocity between the ingoing and outgoing molecules of the simulation domain is maintained constant.

Plane Poiseuille flows were simulated, and the results were compared with approximate analytical solutions of the Navier-Stokes and energy equations reported in the literature. This new method has been proven to be realistic and could be applied to many problems with a nonconstant axial pressure gradient: flows around obstacles or in rough channels, for example. The method appears thus relevant for modeling compressibility effects as well as temperature variations along the flow direction, a domain unfulfilled by the usual molecular dynamics methods.

References

[1] H. Struchtrup, *Macroscopic Transport Equations for Rarefied Gas Flows: Approximation Methods in Kinetic Theory*, Springer, New York, NY, USA, 2005.
 [2] W. W. Liou and Y. Fang, *Microfluid Mechanics*, McGraw-Hill, New York, NY, USA, 2003.

[3] S. Chapman, T. G. Cowling, and D. Burnett, *The Mathematical Theory of Non-Uniform Gases: An Account of the Kinetic Theory of Viscosity, Thermal Conduction, and Diffusion in Gases*, Cambridge University Press, Cambridge, UK, 1990.
 [4] G. A. Bird, *Molecular Gas Dynamics and the Direct Simulation of Gas Flows*, Clarendon Press, 1994.
 [5] G. Karniadakis, A. Beskok, and N. Aluru, *Microflows and Nanoflows: Fundamentals and Simulation*, Springer, New York, NY, USA, 2005.
 [6] B. D. Todd and D. J. Evans, “Temperature profile for Poiseuille flow,” *Physical Review E*, vol. 55, no. 3, pp. 2800–2807, 1997.
 [7] D. K. Bhattacharya and G. C. Lie, “Molecular-dynamics simulations of nonequilibrium heat and momentum transport in very dilute gases,” *Physical Review Letters*, vol. 62, no. 8, pp. 897–900, 1989.
 [8] J. L. Barrat and L. Bocquet, “Large slip effect at a nonwetting fluid-solid interface,” *Physical Review Letters*, vol. 82, no. 23, pp. 4671–4674, 1999.
 [9] Q. D. To, C. Bercegeay, G. Lauriat, C. Léonard, and G. Bonnet, “A slip model for micro/nano gas flows induced by body forces,” *Microfluidics and Nanofluidics*, vol. 8, no. 3, pp. 417–422, 2010.
 [10] M. Lupkowski and F. Van Swol, “Computer simulation of fluids interacting with fluctuating walls,” *The Journal of Chemical Physics*, vol. 93, no. 1, pp. 737–745, 1990.
 [11] J. Li, D. Liao, and S. Yip, “Coupling continuum to molecular-dynamics simulation: reflecting particle method and the field estimator,” *Physical Review E*, vol. 57, no. 6, pp. 7259–7267, 1998.
 [12] M. Sun and C. Ebner, “Molecular-dynamics simulation of compressible fluid flow in two-dimensional channels,” *Physical Review A*, vol. 46, no. 8, pp. 4813–4818, 1992.
 [13] E. B. Arkilic, M. A. Schmidt, and K. S. Breuer, “Gaseous slip flow in long microchannels,” *Journal of Microelectromechanical Systems*, vol. 6, no. 2, pp. 167–178, 1997.
 [14] L. D. Landau and E. M. Lifshitz, *Fluid Mechanics*, Pergamon Press, 1987.
 [15] C. Cai, Q. Sun, and I. D. Boyd, “Gas flows in microchannels and microtubes,” *Journal of Fluid Mechanics*, vol. 589, pp. 305–314, 2007.
 [16] J. H. Irving and J. G. Kirkwood, “The statistical mechanical theory of transport processes. IV. The equations of hydrodynamics,” *The Journal of Chemical Physics*, vol. 18, no. 6, pp. 817–829, 1950.
 [17] B. D. Todd, D. J. Evans, and P. J. Daivis, “Pressure tensor for inhomogeneous fluids,” *Physical Review E*, vol. 52, no. 2, pp. 1627–1638, 1995.
 [18] D. Evans and G. Morriss, *Statistical Mechanics of Nonequilibrium Liquids*, Cambridge University Press, Cambridge, UK, 2008.
 [19] W. G. Hoover, C. G. Hoover, and J. F. Lutsko, “Microscopic and macroscopic stress with gravitational and rotational forces,” *Physical Review E*, vol. 79, no. 3, Article ID 036709, 2009.
 [20] D. H. Tsai, “The virial theorem and stress calculation in molecular dynamics,” *The Journal of Chemical Physics*, vol. 70, no. 3, pp. 1375–1382, 1979.
 [21] M. P. Allen and D. J. Tildesley, *Computer Simulation of Liquids*, Oxford University Press, Oxford, UK, 1989.
 [22] J. P. Hansen and I. R. McDonald, *Theory of Simple Liquids*, Academic Press, New York, NY, USA, 2006.
 [23] D. C. Rapaport, *The Art of Molecular Dynamics Simulation*, Cambridge University Press, Cambridge, UK, 2004.

- [24] D. K. Bhattacharya and G. C. Lie, "Nonequilibrium gas flow in the transition regime: a molecular-dynamics study," *Physical Review A*, vol. 43, no. 2, pp. 761–767, 1991.
- [25] D. Frenkel and B. Smit, *Understanding Molecular Simulation: From Algorithms to Applications*, Academic Press, New York, NY, USA, 2002.
- [26] M. Han and J. S. Lee, "Method for calculating the heat and momentum fluxes of inhomogeneous fluids," *Physical Review E*, vol. 70, no. 6, Article ID 061205, 2004.
- [27] Y. Zheng, A. L. Garcia, and B. J. Alder, "Comparison of kinetic theory and hydrodynamics for Poiseuille flow," *Journal of Statistical Physics*, vol. 109, no. 3-4, pp. 495–505, 2002.
- [28] K. Xu, "Super-Burnett solutions for Poiseuille flow," *Physics of Fluids*, vol. 15, no. 7, pp. 2077–2080, 2003.

Research Article

Measurement and Model Validation of Nanofluid Specific Heat Capacity with Differential Scanning Calorimetry

Harry O'Hanley, Jacopo Buongiorno, Thomas McKrell, and Lin-wen Hu

Massachusetts Institute of Technology, Cambridge, MA 02139, USA

Correspondence should be addressed to Harry O'Hanley, hohanley@mit.edu

Received 16 May 2011; Accepted 14 October 2011

Academic Editor: Kambiz Vafai

Copyright © 2012 Harry O'Hanley et al. This is an open access article distributed under the Creative Commons Attribution License, which permits unrestricted use, distribution, and reproduction in any medium, provided the original work is properly cited.

Nanofluids are being considered for heat transfer applications; therefore it is important to know their thermophysical properties accurately. In this paper we focused on nanofluid specific heat capacity. Currently, there exist two models to predict a nanofluid specific heat capacity as a function of nanoparticle concentration and material. Model I is a straight volume-weighted average; Model II is based on the assumption of thermal equilibrium between the particles and the surrounding fluid. These two models give significantly different predictions for a given system. Using differential scanning calorimetry (DSC), a robust experimental methodology for measuring the heat capacity of fluids, the specific heat capacities of water-based silica, alumina, and copper oxide nanofluids were measured. Nanoparticle concentrations were varied between 5 wt% and 50 wt%. Test results were found to be in excellent agreement with Model II, while the predictions of Model I deviated very significantly from the data. Therefore, Model II is recommended for nanofluids.

1. Introduction

Nanofluids are unique fluids consisting of nanoparticles suspended in a base fluid. They are currently being considered for use by a wide range of industries from energy to manufacturing to medicine.

The ability to customize the characteristics of the nanofluids—through particle material selection—makes them attractive candidates for heat transfer applications. For example, nanofluids can be used as a medium to more effectively transfer energy captured from solar arrays or cool nuclear reactors.

Recent research has indicated that dispersions of nanoparticles in a base fluid, known as nanofluids, can increase the boiling critical heat flux and overall performance of thermal systems. Typical nanoparticle concentrations may range from 0.01 wt% to 50 wt%, and common particle materials include silica, alumina, copper oxide, zirconia, and carbon nanotubes [1–3]. Water often serves as the base fluid though other liquids such as ethylene glycol have been used [1].

As nanofluids are being considered for thermal applications, it is necessary to be able to predict their thermophysical properties accurately. Because nanofluids were initially considered for thermal conductivity enhancement, this property has been extensively studied [2–4]. However, there have been fewer examinations of nanofluid specific heat capacity [5, 6]. It is the objective of this paper to complement existing research by (i) measuring the specific heat capacity of water-based silica, alumina, and copper oxide nanofluids and (ii) comparing the predictions of two popular nanofluid specific heat capacity models to data.

2. Specific Heat Models

There are two specific heat models widely used in the nanofluid literature. Model I is similar to mixing theory for ideal gas mixtures [3]. It is a straight average relating nanofluid specific heat, $c_{p,nf}$, to basefluid specific heat, $c_{p,f}$, nanoparticle specific heat, $c_{p,n}$, and volume fraction, ϕ . Using

these parameters, Model I calculates the nanofluid specific heat as

$$c_{p,nf} = \varphi c_{p,n} + (1 - \varphi) c_{p,f}. \quad (1)$$

While it is simple and thus commonly used, Model I has little theoretical justification in the context of nanofluids.

Model II [3, 7] is based on the assumption of thermal equilibrium between the particles and the surrounding fluid. Starting from an arbitrary mass of nanofluid m_{nf} , of volume V_{nf} and with a nanoparticle volumetric fraction φ , the nanofluid density is obviously $\rho_{nf} = m_{nf}/V_{nf} = \varphi\rho_n + (1 - \varphi)\rho_f$, where the particle and fluid densities are ρ_n and ρ_f , respectively. The energy required to elevate the nanofluid mass is $\varphi V_{nf}(\rho c_p)_n + (1 - \varphi)V_f(\rho c_p)_f$. Therefore, the nanofluid specific heat capacity per unit mass of nanofluid, that is, the nanofluid specific heat, is

$$c_{p,nf} = \frac{\varphi(\rho c_p)_n + (1 - \varphi)(\rho c_p)_f}{\varphi\rho_n + (1 - \varphi)\rho_f}. \quad (2)$$

A rigorous derivation of (2) is presented also in [8].

Predictions of nanofluid specific heat capacity were made using both models and compared to experimental measurements. Water was the base fluid of all nanofluids used in this investigation. Therefore, handbook values of temperature-dependent water specific heat and density were used in calculating theoretical nanofluid specific heat [9]. Additionally, the specific heat and density of the nanoparticles were assumed to be equal to the respective thermophysical properties of particle material in bulk form.

3. Nanofluids

The specific heat capacities of three nanofluids were analyzed: alumina-water (Nyacol AL20DW), silica-water (Ludox TMA 420859), and copper-oxide-water (Alfa Aesar 45407). Selected nanofluid properties are presented in Table 1.

The stock nanofluids were obtained from commercial vendors and diluted with deionized water to vary their concentrations. Prior to mixing, the nanofluids were manually agitated to ensure uniform dispersion. Dilution was performed by weight percent using a Mettler Toledo XS105 balance. Four unique concentrations were prepared for each nanofluid and are listed in Table 2. For each concentration, two identical samples were prepared and tested.

While nanofluids were diluted and prepared according to their weight fraction, calculations were performed using volume fraction. Using the nanoparticle volume, V_n , and the water volume, V_{H_2O} , the volume fraction can be calculated as

$$\varphi = \frac{V_n}{V_n + V_{H_2O}}. \quad (3)$$

Substituting in nanoparticle mass, m_n , and density ρ_n , and water mass, m_{H_2O} , and density, ρ_{H_2O} (3) can be rewritten as

$$\varphi = \frac{m_n/\rho_n}{m_n/\rho_n + m_{H_2O}/\rho_{H_2O}}. \quad (4)$$

TABLE 1: Nanofluid.

Nanofluid	Particle size (nm)	pH	Specific gravity
NYACOL AL20DW	50 nm	4.0	1.19
Ludox TMA 420859	32 nm	4.0–7.0	1.22–1.24
Alfa Aesar 45407	30 nm	4.6	1.50

TABLE 2: Nanofluid sample concentrations.

Nanofluid	Alumina-water	Silica-water	Copper-oxide-water
Conc. 1 (stock)	20 wt%	34 wt%	50 wt%
	(6.4 vol%)	(19.0 vol%)	(13.7 vol%)
Conc. 2	15 wt%	25.5 wt%	37.5 wt%
	(4.6 vol%)	(13.5 vol%)	(8.7 vol%)
Conc. 3	10 wt%	15 wt%	25 wt%
	(2.9 vol%)	(8.5 vol%)	(5.0 vol%)
Conc. 4	5 wt%	8.5 wt%	12.5 wt%
	(1.4 vol%)	(4.1 vol%)	(2.2 vol%)

Equation (4) can be used to determine the nanoparticle volume fraction of nanofluid concentrations created by dilution with deionized water.

4. Measurement Method

A heat-flux-type differential scanning calorimeter (TA Instruments Q2000) was used to measure the nanofluid specific heat capacities. The differential scanning calorimeter (DSC) measures the heat flux into a sample as a function of temperature during a user-prescribed heating regime. It accomplishes this by comparing the heat flux into a pan containing the sample with the heat flux into an empty pan. Hermetically sealed aluminum pans (TA Instruments) were used in the tests presented here.

The classical three-step DSC procedure was followed to measure specific heat capacity [10, 11]. Additionally, testing procedures adhered to protocols set forth in the ASTM Standard Test Method for Determining Specific Heat Capacity by Differential Scanning Calorimetry (E 1269-05).

The three-step DSC procedure begins with designing a heating regime, which should contain the temperature range of interest. Next, a measurement is taken with two empty sample pans loaded into the DSC. During this measurement, the baseline heat flux, Q_0 , is obtained. The results of this measurement indicate the bias in the machine, allowing for it to be accounted for during data reduction.

The second measurement is of a reference sample, with a known specific heat, $c_{p,ref}$. A pan containing the reference sample and an empty pan are loaded into the DSC. The heat flux into the reference sample, Q_{ref} , is recorded throughout the identical heating regime.

The third measurement is made on the actual sample of interest. A pan containing the sample and an empty pan are loaded into the DSC. The heat flux into the sample, Q_{sample} , is recorded during an identical heating regime as the previous two measurements. The heat flux curves from the

three measurements are used to comparatively determine the specific heat of the sample, $c_{p,\text{sample}}$, where

$$c_{p,\text{sample}} = \frac{Q_{\text{sample}} - Q_0}{Q_{\text{ref}} - Q_0} \frac{m_{\text{ref}}}{m_{\text{sample}}} c_{p,\text{ref}} \quad (5)$$

and m_{ref} and m_{sample} represent the masses of the reference and sample, respectively. Sample masses were measured using a Perkin Elmer AD6 autobalance.

In these tests, deionized water was used as the reference sample, with specific heat values obtained from Perry's Chemical Engineers Handbook [9]. The DSC heating procedure consisted of three steps:

- (1) equilibrate and remain isothermal at 25°C for one minute,
- (2) ramp to 75°C at 10°C/min,
- (3) remain isothermal at 75°C for one minute.

Heat flux measurement was continuous from 25°C to 75°C. However, for analysis, specific heat capacities were calculated at 35°C, 45°C, and 55°C. For each sample of nanofluid concentration, three measurements were taken. These values were then averaged to yield the data points and related standard deviations presented in Figures 1, 2, 3, 4, 5, 6, 7, 8, and 9.

Prior to nanofluid measurement, this DSC methodology was validated by analyzing two pure fluids, ethylene glycol and glycerin. The results obtained from these measurements were compared against handbook values of specific heat for these liquids [12]. All experimental data are reported in Section 6.

5. Uncertainty Analysis

The measurement uncertainty for the specific heat was calculated by propagating the precision uncertainties of all individual measurements required to determine the specific heat. Equation (5) suggests there is a precision error associated with the heat flux measurements as well as the mass measurements. If all variables are assumed to be distributed normally, the overall measurement uncertainty, μ_{total} , is

$$\mu_{\text{total}} = \sqrt{\sum_i^n \left(\frac{\partial c_{p,\text{sample}}}{\partial x_i} \mu_i \right)^2}. \quad (6)$$

Here, x_i is the independent variable to be estimated and μ_i is the manufacturer reported precision of the measurement method. Here, (5) is substituted into (6) and the appropriate derivatives are taken to capture all measurement uncertainties. In this instance, each specific heat capacity measurement requires three heat flux measurements and two mass measurements. The associated precision uncertainties are reported in Table 3.

From this analysis, the precision uncertainty in the measurement of specific heat capacity for Model II was found to be about 0.07 (J/g-K).

TABLE 3: Reported measurement uncertainties.

x_i	$\mu_i (\pm)$	Equipment type
Q_s	1.2 mW	TA Instruments Q2000
Q_{ref}	3.3 mW	TA Instruments Q2000
Q_0	10 μ W	TA Instruments Q2000
m_{sample}	0.2 μ g	Perkin Elmer AD6
m_{sample}	0.2 μ g	Perkin Elmer AD6

TABLE 4: Propylene glycol.

Temperature (°C)	Theoretical c_p (J/g-K)	Measured c_p (J/g-K)
35	2.56	2.54 \pm 0.191
45	2.62	2.64 \pm 0.185
55	2.65	2.65 \pm 0.185

TABLE 5: Glycerin.

Temperature (°C)	Theoretical c_p (J/g-K)	Measured c_p (J/g-K)
35	2.39	2.41 \pm 0.008
45	2.41	2.42 \pm 0.002
55	2.42	2.44 \pm 0.001

6. Results and Discussion

DSC measurements of pure ethylene glycol and glycerin were in good agreement with literature values of specific heat capacity. The results of these tests, presented in Tables 4 and 5, validate the DSC methodology and machine calibration.

Figures 1, 2, 3, 4, 5, 6, 7, 8, and 9 show the nanofluids data and the curves predicted by Models I and II. As expected, as nanoparticle concentration increases, the specific heat capacity decreases. However, Model I largely underestimates the decrease, while Model II offers a much more accurate prediction of nanofluid specific heat capacity. These conclusions are consistent with the alumina nanofluid results reported in [3] and expand the validity of Model II to silica and copper oxide nanofluids. In [3], the researchers also found there to be a sharp departure from Model I with increasing nanoparticle volume fraction.

Even for Model II, there appear to be small discrepancies between the data and predictions. These could come from errors in the listed stock nanofluid concentrations, experimental uncertainties in dilution, or inconsistencies in using the bulk material properties in the model, instead of the actual nanoparticle properties. Recent research suggests that these properties may differ if the material is in nanoparticle form versus bulk form [8]. Investigation of these effects is left for future work.

7. Conclusions

Using a heat flux differential scanning calorimeter (DSC), the specific heat capacities of water-based silica, alumina, and copper oxide nanofluids at various nanoparticle concentrations were measured. The DSC procedure was validated by measuring the specific heat capacities of pure ethylene

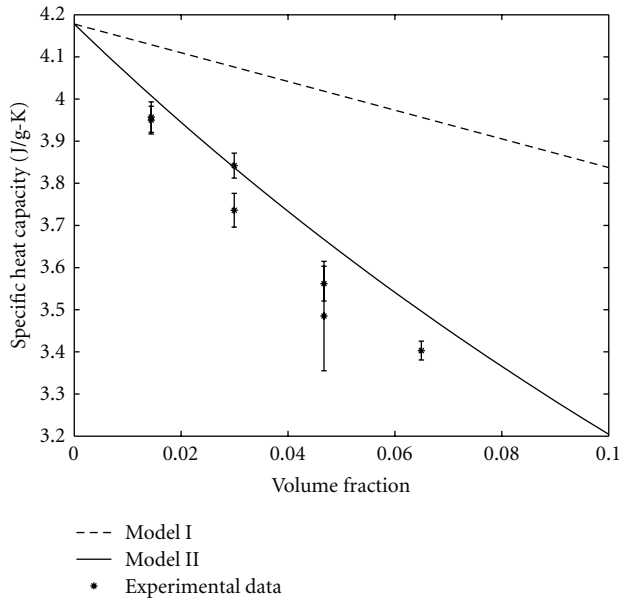


FIGURE 1: Alumina-water at 35°C.

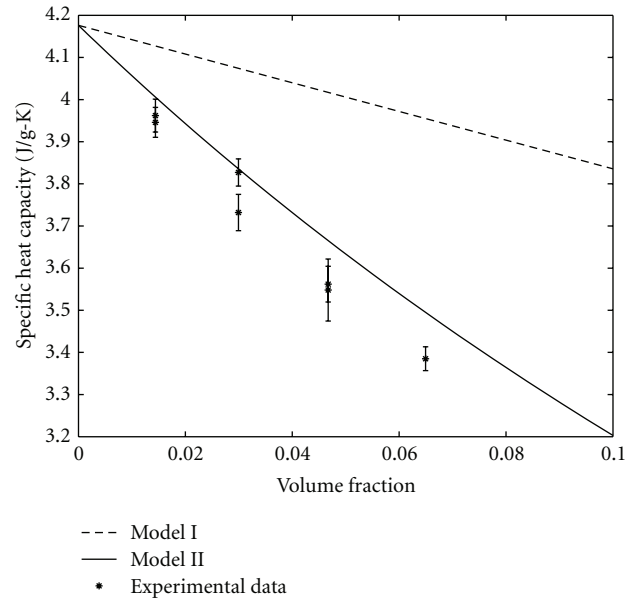


FIGURE 3: Alumina-water at 55°C.

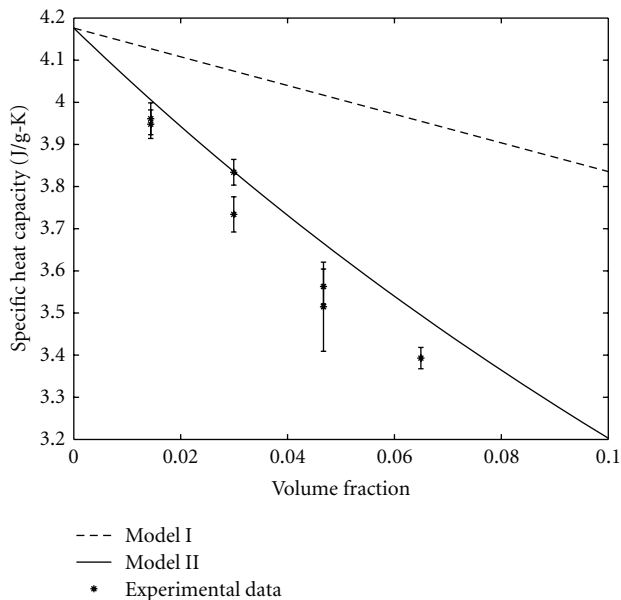


FIGURE 2: Alumina-water at 45°C.

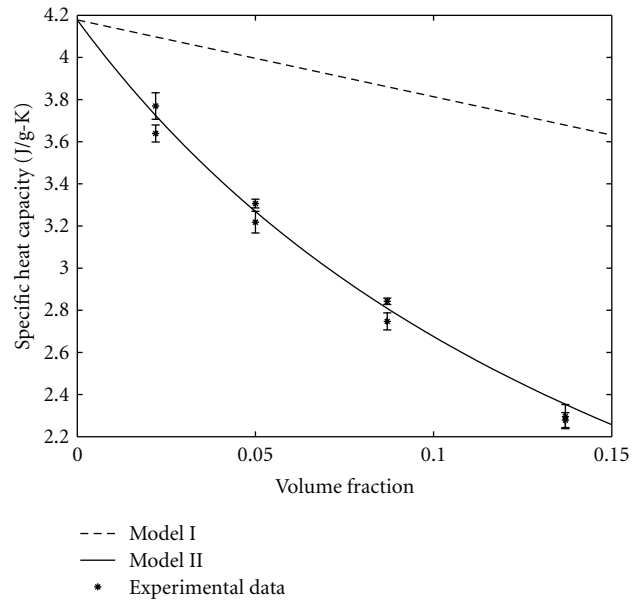


FIGURE 4: Copper-oxide-water at 35°C.

glycol and glycerin, which were confirmed against handbook values. The nanofluid data were used to test the predictions of two popular mixture models for specific heat. The results clearly suggest that the model based on particle/fluid thermal equilibrium (Model II) yields more accurate predictions than the model based on a straight volume-weighted average of the particle and fluid specific heats (Model I). Given its sound theoretical basis, we believe Model II is generally

applicable, while Model I should be abandoned. To further improve the accuracy of Model II, future investigations could focus on measuring the actual density and specific heat of the nanoparticles in dispersion and compare them to those of the bulk materials. Additionally, future research to correlate specific heat capacity with agglomeration and sedimentation would be particularly beneficial, as such phenomena are typically unavoidable in certain applications.

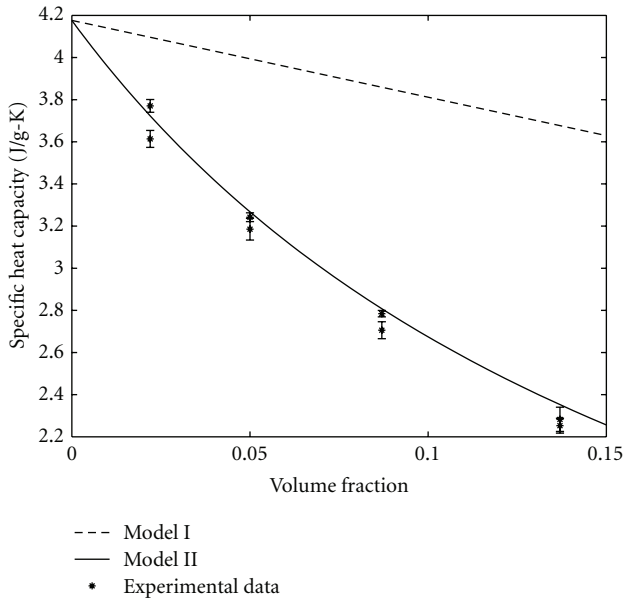


FIGURE 5: Copper-oxide-water at 45°C.

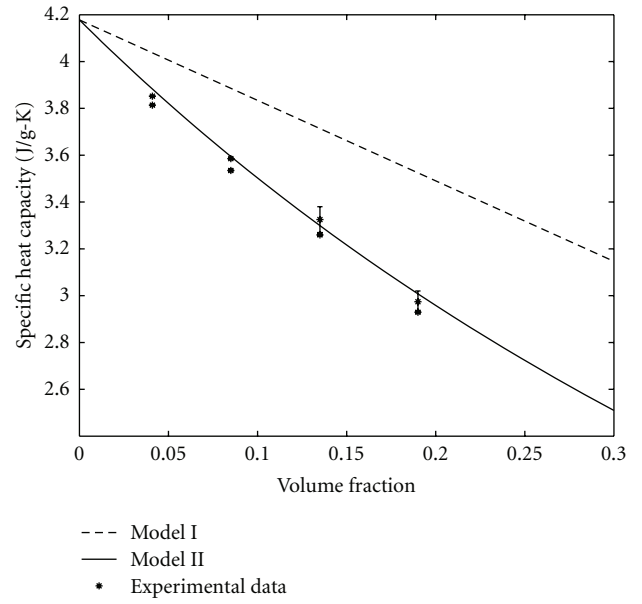


FIGURE 7: Silica-water at 35°C.

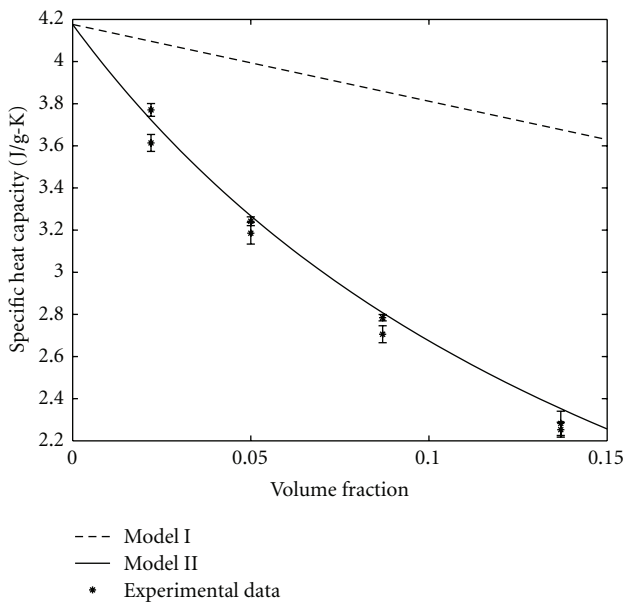


FIGURE 6: Copper-oxide-water at 55°C.

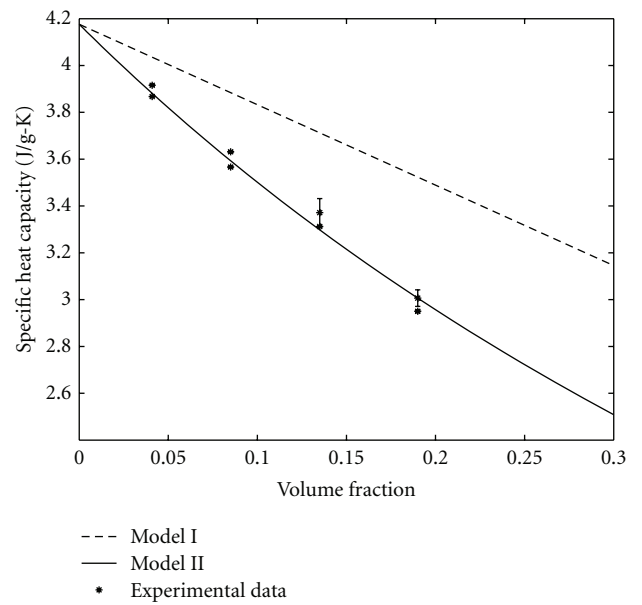


FIGURE 8: Silica-water at 45°C.

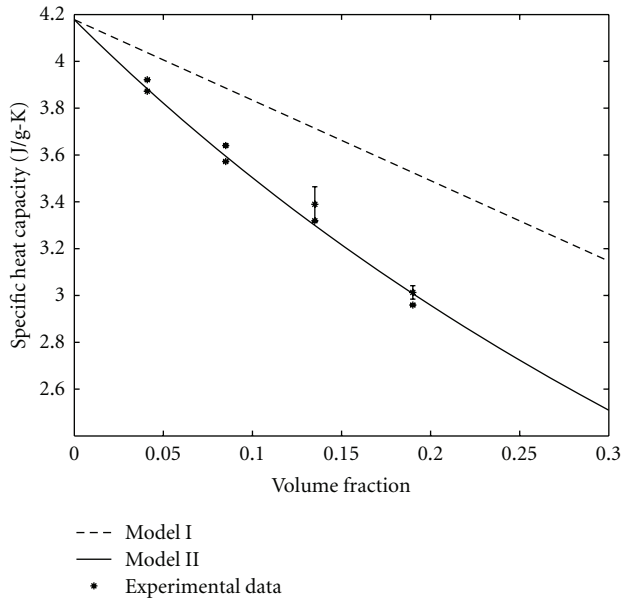


FIGURE 9: Silica-water at 55°C.

Nomenclature

$c_{p,f}$:	Specific heat capacity of base fluid (J/g-K)
$c_{p,nf}$:	Specific heat capacity of nanofluid (J/g-K)
$c_{p,n}$:	Specific heat capacity of nanoparticle (J/g-K)
$c_{p,ref}$:	Specific heat capacity of reference (J/g-K)
$c_{p,sample}$:	Specific heat capacity of sample (J/g-K)
m_{nf} :	Mass of nanofluid (g)
m_n :	Mass of nanoparticles (g)
m_{H_2O} :	Mass of water (g)
m_{ref} :	Mass of reference (g)
m_{sample} :	Mass of sample (g)
Q_{ref} :	Heat flux into reference (Watts)
Q_{sample} :	Heat flux into sample (Watts)
Q_0 :	Heat flux baseline (Watts)
Φ :	Volume fraction (unitless)
ρ_f :	Density of basefluid (g/cm ³)
ρ_n :	Density of nanoparticles (g/cm ³)
ρ_{H_2O} :	Density of water (g/cm ³)
V_{nf} :	Volume of nanofluid (cm ³)
V_n :	Volume of nanoparticles (cm ³)
V_{H_2O} :	Volume of water (cm ³).

Acknowledgments

The Materials Research Science and Engineering Center at Harvard University offered their DSC for use in this paper. Within this facility, Dr. Philseok Kim, Dr. Kosta Ladavac, and Roxanne Kimo offered invaluable instruction and advice on the machine operation.

References

[1] K. Kwak and C. Kim, "Viscosity and thermal conductivity of copper oxide nanofluid dispersed in ethylene glycol," *Korea Australia Rheology Journal*, vol. 17, no. 2, pp. 35–40, 2005.

[2] J. Buongiorno, D. C. Venerus, N. Prabhat et al., "A benchmark study on the thermal conductivity of nanofluids," *Journal of Applied Physics*, vol. 106, no. 9, Article ID 094312, 2009.

[3] S. Q. Zhou and R. Ni, "Measurement of the specific heat capacity of water-based Al₂O₃ nanofluid," *Applied Physics Letters*, vol. 92, no. 9, Article ID 093123, 2008.

[4] S. Sinha, S. Barjami, G. Iannacchione, and S. Sinha, "Thermal properties of carbon nanotube based fluids," in *Proceedings of the Memphis-Area Engineering and Sciences Conference*, 2004.

[5] Q. He, W. Tong, and Y. Liu, "Measurement of specific heat of TiO₂-BaCl₂-H₂O nano-fluids with DSC," *Air Conditioning & Refrigeration*, vol. 7, no. 5, pp. 19–22, 2007 (Chinese).

[6] X. Peng, X. Yu, and F. Yu, "Experiment study on the specific heat of nanofluids," *Journal of Materials Science & Engineering*, vol. 25, no. 5, pp. 719–722, 2007 (Chinese).

[7] J. Buongiorno, "Convective transport in nanofluids," *Journal of Heat Transfer*, vol. 128, no. 3, pp. 240–250, 2006.

[8] L. P. Zhou, B. X. Wang, X. F. Peng, X. Z. Du, and Y. P. Yang, "On the specific heat capacity of CuO nanofluid," *Advances in Mechanical Engineering*, vol. 2010, Article ID 172085, 4 pages, 2010.

[9] D. Green and R. Perry, *Perry's Chemical Engineers' Handbook*, McGraw-Hill, New York, NY, USA, 8th edition, 2008.

[10] G. Hohne, *Differential Scanning Calorimetry*, Springer, New York, NY, USA, 2003.

[11] U.S. Department of Defense, *Military Handbook—MIL-HDBK-17-3F: Composite Materials Handbook, Volume 3—Polymer Matrix Composites Materials Usage, Design, and Analysis*, U.S. Department of Defense.

[12] C. Yaws, *Chemical Properties Handbook*, McGraw-Hill, New York, NY, USA, 1999.

Research Article

Experimental Study of the Freezing Point of γ -Al₂O₃/Water Nanofluid

Thierry Maré,¹ Ousmane Sow,² Salma Halefadi,¹ Sylvain Lebourlout,³
and Cong Tam Nguyen⁴

¹Laboratoire de Génie Civil et de Génie Mécanique (LGCGM), INSA de Rennes, IUT Saint Malo, 35708 Rennes Cedex 7, France

²Laboratoire Matériaux Mécanique et Energétique (LMME), Ecole Polytechnique de Thiès (EPT), Thiès, Senegal

³Centre d'Etude Pole Cristal Dinan, Dinan, France

⁴Mechanical Department, University of Moncton, Moncton, Canada

Correspondence should be addressed to Thierry Maré, thierry.mare@univ-rennes1.fr

Received 27 May 2011; Revised 30 October 2011; Accepted 30 October 2011

Academic Editor: Oronzio Manca

Copyright © 2012 Thierry Maré et al. This is an open access article distributed under the Creative Commons Attribution License, which permits unrestricted use, distribution, and reproduction in any medium, provided the original work is properly cited.

Nanofluids are colloidal suspensions made of nanometer-sized particles dispersed in a conventional fluid. Their unusual thermal properties explain intensive investigations for several thermal and industrial applications. In this work, an experimental investigation was performed to measure the freezing point and to study the supercooling point made of alumina γ -Al₂O₃ nanoparticles with 30 nm diameter size and deionized water. Particles' volume fraction used in this work is ranging from 1% to 4%. The T-historic method based on the measurement of the point of inflexion was performed to measure the thermal properties such as the freezing point and the latent heat of solidification of the nanofluids for different concentrations. The results show that the supercooling degree decreases for the high particles volume concentrations and that the agglomeration does not influence the temperature of the freezing point. However, it makes the freezing process longer.

1. Introduction

Nanofluids are liquids suspensions containing nanoparticles or nanofibers dispersed in a conventional liquid. Recent researches showed an interesting thermal capacity compared to the conventional liquids [1, 2]. Research efforts have mostly been concerned with the characterization of thermal and physical properties of nanofluids. Many experimental studies focused on the measurement of thermal conductivity [3, 4] and the measurement of dynamic viscosity [5, 6] usually for a range of temperature between 20°C and 60°C. Nguyen et al. [7] showed a singular phenomenon of hysteresis for high temperatures and high concentrations. Aladag et al. [8] studied the rheological behavior of alumina/water and aqueous nanotube of carbon nanofluids at low temperature (less than 10°C). Their results show the nanofluids are not Newtonian and that the experimental results of dynamic viscosity are much higher than those from the theoretical models.

Several experimental investigations have revealed an enhancement of the thermal performance in exchangers [9, 10] and an impressive enhancement of the convective heat transfer coefficient in horizontal tubes [11], whereas many factors such as clustering of particles, agglomeration, sedimentation, and the dissociation of the surfactant on the effective thermal properties of nanofluids have an important effect on the results.

The behavior of this type of fluid in a range of temperature below 20°C is not much studied. Some papers show that the behavior of these fluids at low temperature is no longer Newtonian. Khaled and Vafai [12] investigated the effect of the surfactant on the heat transfer, and his experimental results show an influence of the surfactant by more than 20% on the number of Nusselt obtained.

The complexity of the regulation of air conditioning and refrigeration systems especially food industry requires exchangers and buckles with negative temperatures. However, from the point of view of refrigerator performance, the

most commonly used fluids such as water, ethylene glycol, and oil have relatively low thermal conductivity. The high conductivity of nanofluids can be a good solution.

Very few reports studied the thermal properties at low temperature, especially at the freezing and supercooling points. Wu et al. [13] investigated infrared instrument to evaluate the freezing rate of alumina (Al_2O_3)/water nanofluid for very low volume concentrations (less than 0.05%). They found that the addition of the nanoparticles decreases strongly the degree of supercooling and reduces the freezing time. Khodadadi and Hosseinizadeh [14] numerally simulated the thermal energy storage of aqueous CuO nanoparticles at low volume concentration (0.1% and 0.2%). Their results show that freezing time decreases when the particles, volume concentration increases.

The main purpose of this work is to study experimentally the behavior of alumina $\gamma\text{-Al}_2\text{O}_3$ /water nanofluids for the freezing process and to measure the thermal properties using T-history curves for a range of volume fraction of 1–4%.

The T-history method (modified) used in this study is based on the inflection point as the boundary between phase change and solid-state periods [15, 16]. Hong et al. [17] showed 40% discrepancy between the original T-history and the modified T-history method when analyzing the experimental data.

Three different tests are investigated in this present work.

The first test involves putting the nanofluid (initially at 20°C) in a cold room stabilized at temperature -16°C . The acquisition is made at a pace of 45 s.

In the second test, initially the temperature of alumina/water nanofluids and the cold room is the same as 20°C . Then, the temperature is decreased gradually and simultaneously to -15°C .

The third test reproduces the second for nanofluids samples with the same volume concentration and more or less clustering of nanoparticles.

The first part of this paper presents the T-history method and the experimental setup. The second part analyzes the results of the behavior of alumina/water nanofluids at the freezing point.

2. Method of the Historic of the Curves

As shown in Figure 1, the temporal evolution (T-history curve) of cooling process of water consists of three phases. The first one corresponds to the cooling of the liquid phase solution (sensible heat). The second phase is horizontal flat parts where the state changes from liquid to solid (latent heat). Finally, the third phase corresponds to the cooling of the ice (solid) solution (sensitive heat). If the T-history curve maintains at a constant temperature in the latent heat range, the selection of range is very easy. Unfortunately, most of T-history curves show typical phenomena (supercooling).

There are three main temperatures on the T-history curves.

There is the initial temperature of the horizontal flat parts “plateau” T_s which cannot be determined intuitively because of the supercooling process.

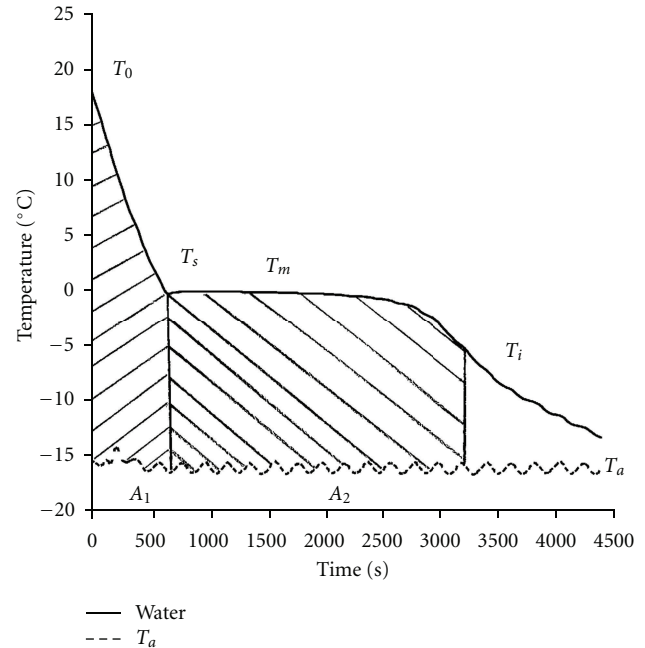


FIGURE 1: T-history curve of water and evolution of temperature with time.

There is the equilibrium freezing temperature T_m where the phase change occurs. Rahman et al. [18] defined it as the temperature in which the slowest cooling rate is observed.

The final temperature of the plateau T_i is defined by the end of latent heat range. This temperature can be calculated using the inflexion point method.

In this present work, the equilibrium temperature of freezing process T_m is evaluated directly from the acquisition data when no difference between two consecutive measurement is observed. The final temperature T_i is obtained using the slope method (Figure 2(a)).

Figure 2(b) shows the slope (derivative in $^\circ\text{C/s}$) of the cooling curve for water as a function of cooling time. When the amount of ice formation decreases, the slope started to increase and reached the highest value of plateau. The end of freezing is defined when the cooling rate is the highest. So T_i is the highest slope value corresponding to the end of the plateau.

The slope decreases to a minimum before ice crystal formation starts. This minimum corresponds to T_s , the supercooling temperature.

The latent heat of solidification is evaluated as the amount of energy required in the second phase (horizontal flat parts) which starts at the beginning of the supercooling process and finishes at the end of the plateau.

3. Determination of the Latent Heat of Solidification

The energy equations including the phase change of water in a tube placed in a room at constant temperature T_a are, respectively as follows.

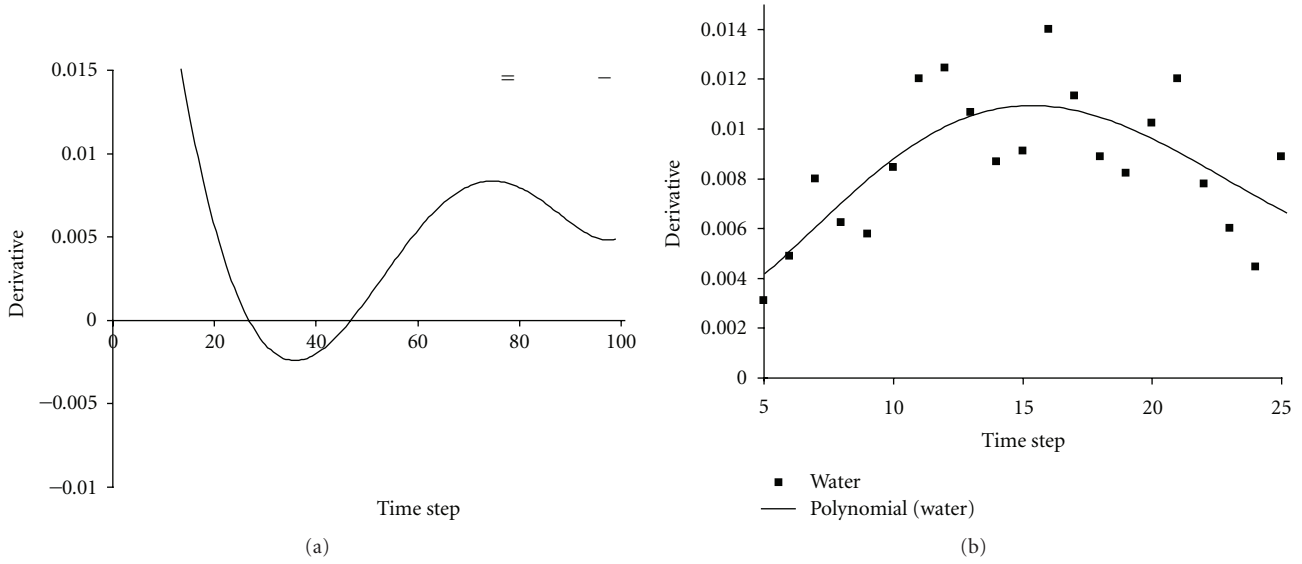


FIGURE 2: (a) Evolution of first derivative ($^{\circ}\text{C/s}$) with time, (b) infection point (end of plateau) for water.

For the liquid sensible heat range between t_0 and t_s ,

$$(m_t(C_p)_t + m_{nf}(C_p)_{nf})(T_0 - T_s) = KS_t A_1, \quad (1)$$

with

$$A_1 = \int_{t_0}^{t_s} (T_{nf} - T_a) dt. \quad (2)$$

During the solidification state between t_s and t_i ,

$$\left(m_t(C_p)_t + \frac{m_{nf}((C_p)_{nf} + (C_p)_{nfice})}{2} \right) (T_m - T_i) + m_{nf}H = KS_t A_2,$$

$$A_2 = \int_{t_s}^{t_i} (T_{nf} - T_a) dt. \quad (3)$$

The latent heat solidification of the fluid is given by

$$H = \frac{[B(T_m - T_i)]}{m_{nf}}, \quad (4)$$

with

$$B = (m_t(C_p)_t + m_{nf}(C_p)_{nf})(T_0 - T_s) \left(\frac{A_1}{A_2} \right) - \left(m_t(C_p)_t + \frac{m_{nf}((C_p)_{nf} + (C_p)_{nfice})}{2} \right). \quad (5)$$

A_1 and A_2 correspond to the area below the curve in the considering period shown in Figure 1.

4. Description of the Experimental Setup

The experimental setup for the cooling process is shown in Figure 3. Identical test tubes for three samples of nanofluids

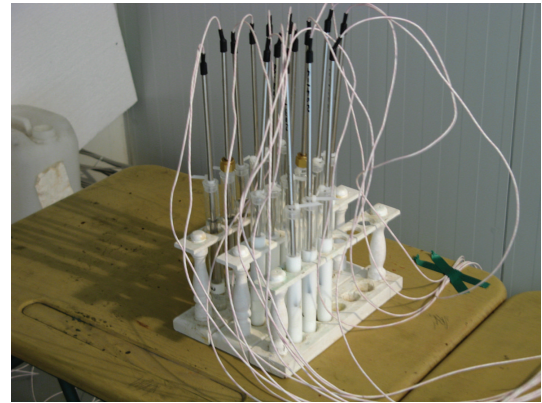


FIGURE 3: Experimental setup.

for each concentration and for reference fluid (pure water) are placed in an insulated cold room which was previously at -16°C . The test tubes racks were disposed on a table in the middle of the cold room (Figure 3). This room has got a ground area of 12 m^2 and a height of 2.5 m . It is cooled by a double-flux distributor situated at the ceiling and connected to a refrigerator.

The Pt100 sensors are placed axially and at midheight for each test tube to measure the temperature variation. To visualize the temporal evolution of temperatures, the sensors Pt100 are joined to a power station acquisition Agilent 34970 A permitting a temperature precision of 0.1°C .

5. Validation of the Installation

The experimental setup is validated using water at PH = 5. Each tube contains 15 mL of sample. The tubes have the following characteristics: $m_t = 0.03 \text{ kg}$, $v_t = 20 \text{ mL}$, and $C_{pt} = 800 \text{ J/kgK}$.

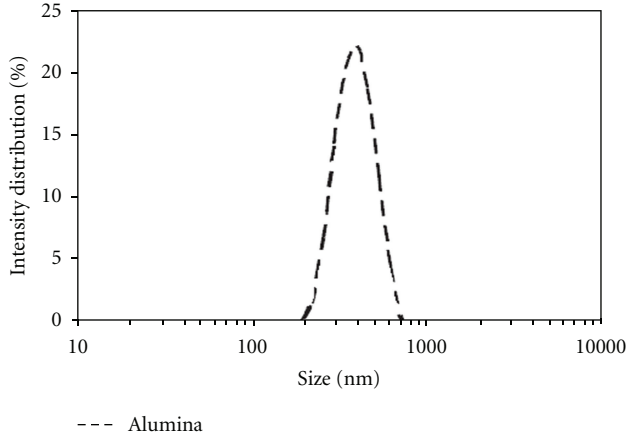


FIGURE 4: Evolution of Al_2O_3 nanoparticles size with the intensity distribution (%).

Initially at ambient temperature (20°C), the samples are placed in the center of the cold room stabilized at -16°C with a precision of 0.2°C . The temporal evolution of temperatures in the center of each sample is raised by the power station of acquisition which is made at a pace of 45 s. The results are calculated from the average temperature of three samples. Figure 1 shows the T-history curve for pure water.

Regarding the relative uncertainty on all the measurements (mass, temperature, time, and C_p), and the (1) to (8), the latent heat of water (Table 1) is obtained with a relative uncertainty of 15%.

6. Results

6.1. Nanofluids Properties. The nanofluids used in this work are composed of demineralized water with $\text{pH} = 5$, alumina nanoparticles ($\gamma\text{-Al}_2\text{O}_3$), and 1% (mass concentration) of surfactant. The mass concentration of the nanofluids was initially 49.9% and has been diluted to get samples with volume concentrations of 1%, 2%, 3%, and 4%. The relation below allows the transition between mass and volume concentrations:

$$\varphi_v = \frac{\varphi_w (\rho_f / \rho_p)}{(1 - \varphi_w (1 - \rho_f / \rho_p))}. \quad (6)$$

The characteristics and the thermal properties of the base fluid (pure water) and the solid nanoparticles ($\gamma\text{-Al}_2\text{O}_3$) used in this study are presented in Table 2.

6.1.1. The Density. We supposed that the density of the particles is constant in the range of temperature used, and we take into account the variation of the water density according to the temperature. We neglected the presence of surfactant, and the relation used is the following:

$$\rho_{\text{nf}} = (1 - \varphi_v) \rho_f + \varphi_v \rho_p. \quad (7)$$

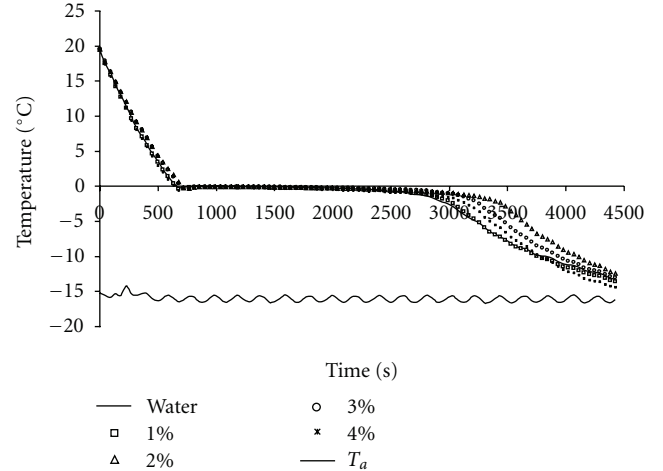


FIGURE 5: T-history curve of 4 nanofluids (1%, 2%, 3%, and 4%), evolution of temperature with time (Test 1).

6.1.2. The Specific Heat. The specific heat of nanofluids was obtained from the equation given by Xuan and Roetzel [19] who supposed that the nanoparticles are immiscible in water,

$$(C_p)_{\text{nf}} = (1 - \varphi_v) (C_p)_f + \varphi_v (C_p)_p. \quad (8)$$

The same relation is used in solid phase considering the specific heat of ice for the base fluid.

6.1.3. Dispersion of Nanoparticles. To control the dispersion of alumina/water nanofluids, we investigated an experimental test based on measuring the size of nanoparticles by dynamic light scattering by using a Zetasizer Nano S (Malvern Instruments). This method can detect the presence of agglomerates [20]. Figure 4 illustrates the particles size distributions of alumina ($\gamma\text{-Al}_2\text{O}_3$)/water nanofluids. The particles' size distribution possesses just one peak which shows that our nanofluids are stables. The average particles size is around 400 nm, and it is greater than the initial particles size. It is because there is particles agglomeration.

6.2. Test 1 (Freezing Process of Nanofluid). In this test, we put the tubes racks of the samples of alumina/water nanofluids initially at the ambient temperature (20°C) at the center of the cold room stabilized at -16°C . Figure 5 shows the T-history curves of alumina/water nanofluids and of pure water. We can notice that the solidification phase for different concentration of alumina/water nanofluids is nearly similar to water solidification phase. The freezing point is close to $T_c = 0^\circ\text{C}$. Therefore, Figure 6 shows that the freezing degree decreases when the particles volume concentration increases.

However, the difference between the samples is still very low; the freezing temperatures of the samples vary on a range of 0°C to -16°C . In addition to this, the sensors Pt100 have a precision of 0.1°C . So it is hard to evaluate objective conclusions with regard to the variation of the freezing temperature for volume fraction range of 1% to 4% of alumina/water nanofluids.

TABLE 1: Characteristic of T-history curve and heat latent results.

	0%	1%	2%	3%	4%
T_0 (°C)	19.5	19.4	19.6	19.6	19.7
T_a (°C)	-16.0	-16.0	-16.0	-16.0	-16.0
T_s (°C)	-0.2	-0.4	-0.3	-0.3	-0.5
T_m (°C)	0	-0.1	-0.0	-0.0	-0.1
T_i (°C)	-5.3	-5.9	-6.0	-6.1	-6.5
H (kJ/kg)	332 ± 32	315 ± 47	276 ± 41	238 ± 36	293 ± 44

TABLE 2: Thermophysical properties of different phases (water/ Al_2O_3 nanoparticles).

Property	Base fluid (water)	Nanoparticles Al_2O_3
C_p (J/kg·K)	4182	773
ρ (kg/m ³)	998.2	3880
k (W/m·K)	0.6	36
Particles diameter (nm)	—	30

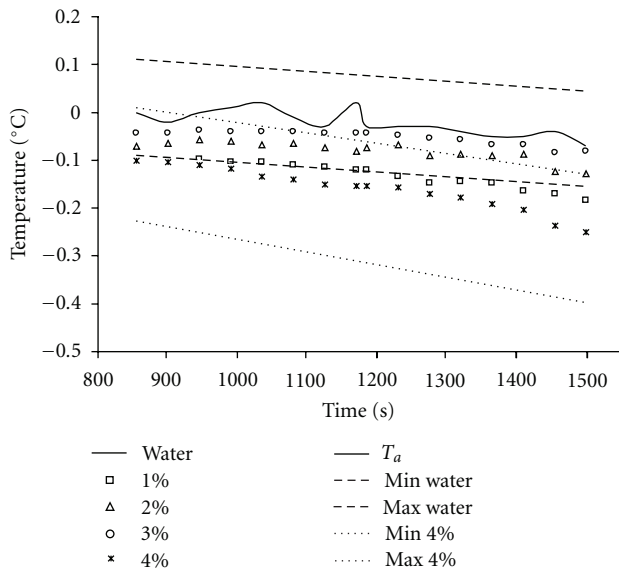


FIGURE 6: Precision of melting fusion of nanofluid (plateau).

If we compare only the T-history curve of alumina/water nanofluid at 4% volume fraction with pure water (Figure 6), we will notice that the points of measurement of alumina/water nanofluids (dotted line in Figure 5) are not in the range of uncertainty of pure water, and vice versa. The results in Table 1 show that the latent heat of solidification decreases with increasing the concentration of particle.

6.3. *Test 2 (Supercooling Point of Nanofluids)*. Initially the temperature of the nanofluids and the cold room was stabilized at 20°C (ambient temperature). The test tubes racks were disposed on a table in the middle of the room. Then, the temperature decreased gradually and simultaneously to

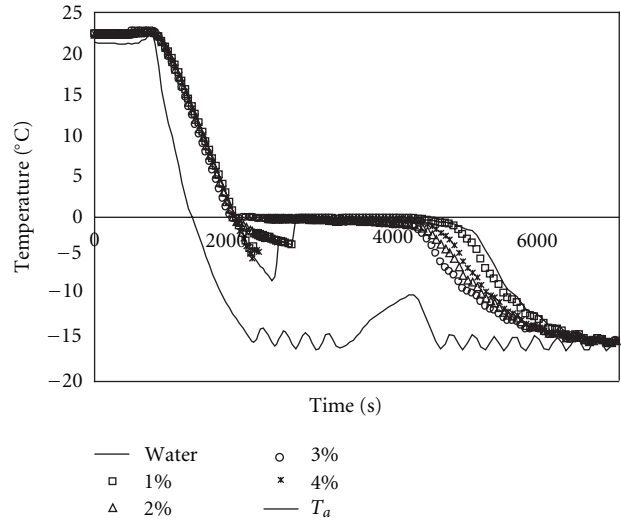


FIGURE 7: T-history curve of 4 nanofluids (1%, 2%, 3%, and 4%), evolution of supercooling (Test 2).

-15°C. Figure 7 shows the T-history curves of alumina/water nanofluids and of pure water. Unlike the first test, in this second test, we can observe the supercooling process for all the samples. We noticed that the supercooling degree decreases when the volume fraction of Al_2O_3 nanoparticles increases. However, it is not possible to establish a correlation between the supercooling degree observed and the percentage of volume concentration of the nanofluids. It is due to the uncertainty of measurements and the phenomena of agglomeration and sedimentation of the nanofluids. In fact, it is difficult to evaluate the homogeneity and the dispersion rate of agglomeration or sedimentation of every solution.

The supercooling temperature obtained for this test is T_s (0%) = -7.8°C; T_s (1%) = -3.4°C; T_s (2%) = -2.4°C; T_s (3%) = -0.6°C; T_s (4%) = -4.2°C.

6.4. *Test 3 (Sedimentation of Nanofluid)*. This third experience consisted in observing the impact of the sedimentation of the Al_2O_3 nanoparticles on the freezing phase and the supercooling point. We have let six samples of the same volume fraction (3%) stand for 16 hours and 30 minutes. Then three samples have been agitated just before starting the cooling process (Test 2). The cold room was stabilized at -5°C.

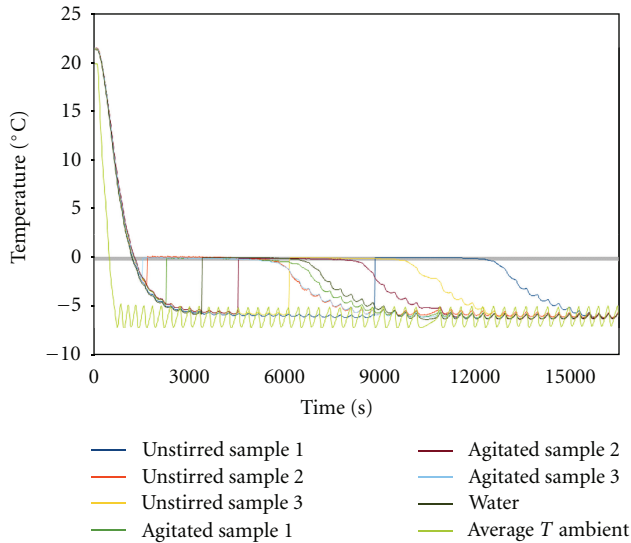


FIGURE 8: T-history curve of 4 nanofluids (1%, 2%, 3%, and 4%), impact of sedimentation (Test 3).

The T-history curves for the six samples of Al_2O_3 nanoparticles (Figure 8) show that the impact of agglomeration on the freezing point is insignificant. However, the supercooling time increases strongly with agglomeration. In fact, the agitation allows a good dispersion for the Al_2O_3 nanoparticles, but their agglomeration encourages germination.

7. Conclusion

Three experimental tests were performed to measure the freezing point and to study the supercooling point made of alumina $\gamma\text{-Al}_2\text{O}_3$ nanoparticles with 30 nm diameter size and deionized water. The results show that the solidification phase for different concentration of alumina/water nanofluids is nearly similar to water solidification phase, and the freezing and supercooling degrees decrease when the particles volume concentration increases and that is not possible to establish a correlation between the supercooling degree observed and the percentage of volume concentration of the nanofluids due to the uncertainty of measurements and to the phenomena of agglomeration and sedimentation in the nanofluids. In addition to this, we found that the impact of agglomeration on the freezing point is insignificant and that the supercooling time increases strongly with agglomeration.

The difference observed in the first test between water and alumina nanofluids with 4% volume fraction shows that for high-volume fraction of Al_2O_3 nanoparticles, the solidification phase could be different from water.

The heat latent of solidification seems less important for nanofluids in comparison to water.

Finally the impact of the surfactant and the dispersion of nanoparticles must be better dominated to analyze in a more precise way the cooling process.

Nomenclature

C_p : Specific heat, J/kg.K
 m : Mass, Kg
 K : Convective heat transfer, $\text{W}/\text{m}^2\text{K}$
 k : Thermal conductivity, W/mK .
 V : Volume, m^3
 φ : Concentration
 T : Temperature, $^\circ\text{C}$, K
 ρ : Density, kg/m^3
 S : Area, m^2

Subscripts

t : Tube
 f : Base fluid (water)
 O : Starting point
 m : Melting equilibrium
 v : Volumic
 p : Particle
 nf : Nanofluid
 $nfce$: Nanofluid solid phase
 s : Supercooling
 i : End of solidification
 a : Ambient
 w : Massic.

Acknowledgments

The head of Pole Cristal of Dinan, Frederic Bazantay, is gratefully acknowledged for his contribution to this study. Malvern Company is gratefully acknowledged for its help in DLS measurement.

References

- [1] S. Z. Heris, M. N. Esfahany, and S. G. Etemad, "Experimental investigation of convective heat transfer of Al_2O_3 /water nanofluid in circular tube," *International Journal of Heat and Mass Transfer*, vol. 28, no. 2, pp. 203–210, 2007.
- [2] R. Luciu, T. Maré, and O. Sow, "Enhancement of Heat transfer in solar using nanofluid: experimental dated," in *Proceedings of the 4th International Conference on Thermal Engineering: theory and Applications (ICTEA '09)*, Abu Dhabi, UAE, January 2009.
- [3] S. Lee, S. U. S. Choi, S. Li, and J. A. Eastman, "Measuring thermal conductivity of fluids containing oxide nanoparticles," *Journal of Heat Transfer*, vol. 121, no. 2, pp. 280–289, 1999.
- [4] H. Q. Xie, J. C. Wang, T. G. Xi, Y. Liu, F. Ai, and Q. R. Wu, "Thermal conductivity enhancement of suspensions containing nanosized alumina particles," *Journal of Applied Physics*, vol. 91, no. 7, pp. 4568–4572, 2002.
- [5] J. H. Lee, K. S. Hwang, S. P. Jang et al., "Effective viscosities and thermal conductivities of aqueous nanofluids containing low volume concentrations of Al_2O_3 nanoparticles," *International Journal of Heat and Mass Transfer*, vol. 51, no. 11–12, pp. 2651–2656, 2008.
- [6] P. Kebabian, S. R. Phillpot, S. U. S. Choi, and J. A. Eastman, "Mechanisms of heat flow in suspensions of nano-sized particles nanofluids," *International Journal of Heat and Mass Transfer*, vol. 45, no. 4, pp. 855–863, 2002.

- [7] C. T. Nguyen, F. Desgranges, G. Roy et al., "Temperature and particle-size depends viscosity dated heart water-based nanofluids—hysteresis phenomenon," *International Journal of Heat of and Fluid Flow*, vol. 28, no. 6, pp. 1492–1506, 2007.
- [8] B. Aladag, S. Halelfaldl, P. Estelle et al., "Experimental investigations of nanofluids at low temperatures," in *Proceedings of the 3rd International Conference on Applied Energy*, pp. 3153–3162, Perugia, Italy, May 2011.
- [9] T. Maré, S. Halelfadl, O. Sow et al., "Comparison of the thermal performances of three nanofluids at low temperature in a plate heat exchanger," *Experimental and Fluid Science*, vol. 35, no. 8, pp. 1535–1543, 2011.
- [10] C. Nelson, D. Banerjee, and P. Rengasamy, "Flow loop experiments using polyalphaolefin nanofluids," *Journal of Thermophysics and Heat Transfer*, vol. 23, no. 4, pp. 752–761, 2009.
- [11] Y. Ding, H. Alias, D. Wen, and R. A. Williams, "Heat transfer of aqueous suspensions of carbon nanotubes (CNT nanofluids)," *International Journal of Heat and Mass Transfer*, vol. 49, no. 1-2, pp. 240–250, 2006.
- [12] A. R. A. Khaled and K. Vafai, "Heat transfer enhancement through control of thermal dispersion effects," *International Journal of Heat and Mass Transfer*, vol. 48, no. 11, pp. 2172–2185, 2005.
- [13] S. Wu, D. Zhu, X. Li, H. Li, and J. Lei, "Thermal energy storage behavior of $\text{Al}_2\text{O}_3\text{-H}_2\text{O}$ nanofluids," *Thermochimica Acta*, vol. 483, no. 1-2, pp. 73–77, 2009.
- [14] J. M. Khodadadi and S. F. Hosseinizadeh, "Nanoparticle-enhanced phase change materials (NEPCM) with great potential for improved thermal energy storage," *International Communications in Heat and Mass Transfer*, vol. 34, no. 5, pp. 534–543, 2007.
- [15] J. H. Peck, J.-J. Kim, C. Kang, and H. Hong, "A study of accurate latent heat measurement for a PCM with a low melting temperature using T-history method," *International Journal of Refrigeration*, vol. 29, no. 7, pp. 1225–1232, 2006.
- [16] H. Hong, C. Kang, and J. H. Peck, "Measurement method of latent heat of PCM with low melting temperature in closed tube," *International Journal of Air-Conditioning and Refrigeration*, vol. 12, no. 4, pp. 206–213, 2004.
- [17] H. Hong, C. H. Park, J. H. Choi, and J. H. Peck, "Improvement of the T-history method to measure heat of fusion for phase change materials," *International Journal of Air-Conditioning and Refrigeration*, vol. 11, no. 1, pp. 32–39, 2003.
- [18] M. S. Rahman, N. Guizani, M. Al-Khaseibi, S. Ali Al-Hinai, S. S. Al-Maskri, and K. Al-Hamhami, "Analysis of cooling curve to determine the end point of freezing," *Food Hydrocolloids*, vol. 16, no. 6, pp. 653–659, 2002.
- [19] Y. Xuan and W. Roetzel, "Conceptions for heat transfer correlation of nanofluids," *International Journal of Heat and Mass Transfer*, vol. 43, no. 19, pp. 3701–3707, 2000.
- [20] B. Pak and Y. I. Cho, "Hydrodynamic and heat transfer study of dispersed fluids with submicron metallic oxide particles," *Experimental Heat Transfer*, vol. 11, no. 2, pp. 151–170, 1998.

Research Article

Numerical Investigation on Mixed Convection in Triangular Cross-Section Ducts with Nanofluids

Oronzio Manca, Sergio Nardini, Daniele Ricci, and Salvatore Tamburrino

Dipartimento di Ingegneria Aerospaziale e Meccanica, Seconda Università degli Studi di Napoli, Real Casa dell'Annunziata, Via Roma 29, 81031 Aversa (CE), Italy

Correspondence should be addressed to Oronzio Manca, oronzio.manca@unina2.it

Received 5 July 2011; Accepted 21 September 2011

Academic Editor: Kambiz Vafai

Copyright © 2012 Oronzio Manca et al. This is an open access article distributed under the Creative Commons Attribution License, which permits unrestricted use, distribution, and reproduction in any medium, provided the original work is properly cited.

Convective heat transfer can be enhanced passively by changing flow geometry and boundary conditions or by improving the thermal conductivity of the working fluid, for example, introducing suspended small solid nanoparticles. In this paper, a numerical investigation on laminar mixed convection in a water- Al_2O_3 -based nanofluid, flowing in a triangular cross-sectioned duct, is presented. The duct walls are assumed at uniform temperature, and the single-phase model has been employed in order to analyze the nanofluid behaviour. The hydraulic diameter is equal to 0.01 m. A fluid flow with different values of Richardson number and nanoparticle volume fractions has been considered. Results show the increase of average convective heat transfer coefficient and Nusselt number for increasing values of Richardson number and particle concentration. However, also wall shear stress and required pumping power profiles grow significantly.

1. Introduction

Heat transfer enhancement is a significant issue in the research and industry fields. Several thermal device applications employ ducts characterized by noncircular cross-sections, thus many investigations have concerned with this topic. Different shapes of cross-section area have been analyzed, like square, rhombic, rectangular, triangular, sinusoidal, elliptical ones, even with truncated corners [1–6]. In particular, triangular sectioned ducts are suitable for the construction of compact heat exchangers because of their compactness and cost effectiveness [7, 8]. In fact, compact heat exchangers with triangular-sectioned passages provide relative low fabrication costs because of the easy construction with thin materials and high mechanical strength [9]. Investigations have been performed in mixed and forced convection, considering mainly the flow regime laminar and also turbulent ones [10–15] and recently also microchannel have been analyzed [16]. Experimental test [3, 14] and analytical [17] and numerical methods [18, 19] are available in the literature. The use of numerical methods is nowadays widely adopted calculator powers and scheme strongly improved.

Several researchers developed and validated unstructured grid meshes both in laminar and turbulent flow regime [18, 19] in order to predict the friction and heat transfer features in triangular ducts. Moreover, different fluids have been considered like gas, liquid, and non-Newtonian ones [11, 20].

Forced convection in a triangular duct is affected by several parameters, including the apex angle, the hydraulic diameter, the axial length, and the flow conditions. A comprehensive review of theoretical and experimental studies on laminar forced convection and heat transfer in ducts having noncircular sections has been performed by Shah and London [21]. In particular, they provided the flow and thermal performances of equilateral, isosceles, and right triangular ducts in developed and thermal developing flow. For the fully developed flow, a Nusselt number value equal to 2.47, 3.111, and 1.892 were reported for T , H_1 and H_2 boundary conditions, respectively. A few works are reported on natural [22] or mixed convection [10] in triangular sectioned ducts. Ali and Al-Ansary [22] analyzed the natural convection in vertical triangular ducts in laminar and transition regime,

giving the critical values of the modified Rayleigh number for the transition to turbulent flow. They underlined the local axial (perimeter averaged) heat transfer coefficient decrease in the laminar region and increase in the transition one. Talukdar and Shah [10] studied the effect of Rayleigh number on bulk mean temperature and Nusselt number in triangular ducts with different apex angles. They pointed out the increase of these parameters for increasing Rayleigh numbers and the higher heat transfer rate from the bottom boundary.

According to Bergles [23] there are several enhancement techniques available. Among them, passive techniques, employing special surface geometries, rough surfaces, extended surfaces or swirl flow devices, and fluid additives for the enhancement can be adopted [24]. An innovative way to improve the fluid thermal conductivity consists of the introduction of nanosize particles suspended in the working fluids. The so-called nanofluids are composed by a base fluid and solid particles with a diameter smaller than 100 nm. They are becoming more and more popular, and there is a fast growth in the number of scientific research activities in these topics in order to evaluate solutions to develop efficient heat exchangers or cooling devices [25–27]. In fact, several investigations pointed out that nanofluid heat transfer average coefficients could increase by more than 20% in comparison with the base fluid coefficients also in the case of low nanoparticle concentrations [28]. However, a critical discussion about the lack of agreement among results from different research groups must be pointed out. There are still some difficulties in formulating efficient theoretical models for the predictions [29, 30], but this topic is still incomplete, as recently underlined by Gherasim et al. [31]. It is well known that the evaluation of properties, like thermal conductivity and viscosity, differs from different research groups because of the numerical and experimental approaches and processes adopted [32, 33].

The number of theoretical and experimental investigations on convective heat transfer in confined flows with nanofluids is growing. For example, experimental tests were performed on forced convective heat transfer in laminar and turbulent flow regime of nanofluids inside tubes in [34, 35]. Correlations for the Nusselt number, using nanofluids composed of water and Cu, TiO₂, and Al₂O₃ nanoparticles were proposed. Experimental results for the convective heat transfer of Al₂O₃ (27–56 nm)/water-based nanofluids flowing through a copper tube in laminar regime was reported in [36]. An experimental investigation was carried out to study the mixed laminar convection of Al₂O₃-water nanofluid inside an inclined copper tube submitted to a uniform wall heat flux at its outer surface by Ben Mansour et al. [37]. Results showed that the experimental heat transfer coefficient decreases slightly with an increase of particle volume concentration from 0% to 4%. They developed correlations to calculate the Nusselt number in the fully developed region for horizontal and vertical tubes, for Rayleigh number from 5×10^5 to 9.6×10^5 , Reynolds number from 350 to 900 and particle volume concentrations up to 4%. Moreover, also the number of numerical studies on nanofluids is growing,

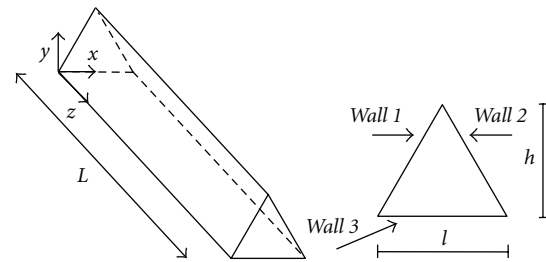


FIGURE 1: Sketch of the geometrical model.

and the analysis can be carried out by using two approaches. It is possible to consider that the continuum assumption is still valid for fluids with suspended nanosize particles at low volume fractions or to adopt two-phase models in order to describe both the fluid and the solid phase. The single-phase model with physical and thermal properties, all assumed to be constant with temperature, was employed in [38–41]. The advantages of adopting nanofluids with respect to the heat transfer mechanism were discussed in [38, 39], but it was also found that the presence of nanoparticles led to significant effects on growing wall shear stress and pumping power for heated tubes in laminar and turbulent regime. For a given Reynolds number, buoyancy force has a negative effect on the Nusselt number, while the nanoparticles concentration had a positive effect on the heat transfer enhancement and also on the skin friction reduction, as pointed out in [40], where the mixed convection in horizontal curved tubes was performed. Mirmasoumi and Behzadmehr [41] adopted a two-phase model in order to describe the strong influence of particle concentration on the thermal parameters, above all on the tube bottom part and also at the near wall region.

In the present paper, a numerical investigation on laminar mixed convection in ducts with an equilateral triangular cross-section is presented. A constant and uniform temperature is applied on the walls. Results are given to evaluate the fluid dynamic and thermal features of the considered geometry with different Richardson number values, adopting Al₂O₃/water nanofluid as the working fluid. Different nanoparticle volume fractions are considered and the single-phase model has been assumed.

2. Governing Equations

A computational analysis of a three-dimensional model concerning with the mixed convection in a triangular cross sectioned duct is considered, and its scheme is reported in Figure 1. The aim is to evaluate its thermal and fluid-dynamic behaviours and study the temperature and velocity fields in the cases with Al₂O₃/water nanofluid as working fluid. A constant uniform temperature is applied on the walls, such as the T_1 boundary condition indicated in [21], and its value is evaluated on the basis of the chosen Richardson numbers. The inlet average velocity is set in the ranges

of laminar regime. Single-phase model is employed and the fluid properties are considered constant with temperature.

Governing equations of continuity, momentum and energy, for a three-dimensional steady state laminar, incompressible flow, with temperature independent thermophysical properties and assuming the Boussinesq approximation, in rectangular coordinates are given in the following:

continuity:

$$\frac{\partial u}{\partial x} + \frac{\partial v}{\partial y} + \frac{\partial w}{\partial z} = 0, \quad (1)$$

momentum:

$$\left[u \frac{\partial u}{\partial x} + v \frac{\partial u}{\partial y} + w \frac{\partial u}{\partial z} \right] = -\frac{1}{\rho} \frac{\partial P}{\partial x} + \nu \left[\frac{\partial^2 u}{\partial x^2} + \frac{\partial^2 u}{\partial y^2} + \frac{\partial^2 u}{\partial z^2} \right], \quad (2)$$

$$\left[u \frac{\partial v}{\partial x} + v \frac{\partial v}{\partial y} + w \frac{\partial v}{\partial z} \right] = -\frac{1}{\rho} \frac{\partial P}{\partial y} + \nu \left[\frac{\partial^2 v}{\partial x^2} + \frac{\partial^2 v}{\partial y^2} + \frac{\partial^2 v}{\partial z^2} \right] + \beta g(T - T_{in}), \quad (3)$$

$$\left[u \frac{\partial w}{\partial x} + v \frac{\partial w}{\partial y} + w \frac{\partial w}{\partial z} \right] = -\frac{1}{\rho} \frac{\partial P}{\partial z} + \nu \left[\frac{\partial^2 w}{\partial x^2} + \frac{\partial^2 w}{\partial y^2} + \frac{\partial^2 w}{\partial z^2} \right], \quad (4)$$

energy:

$$\left[u \frac{\partial T}{\partial x} + v \frac{\partial T}{\partial y} + w \frac{\partial T}{\partial z} \right] = \lambda \left[\frac{\partial^2 T}{\partial x^2} + \frac{\partial^2 T}{\partial y^2} + \frac{\partial^2 T}{\partial z^2} \right]. \quad (5)$$

The assigned boundary conditions are the following:

- (i) inlet section: uniform velocity and temperature profiles,
- (ii) outlet section: outflow condition with velocity components and temperature derivatives equal to zero,
- (iii) duct surfaces: velocity components equal to zero and assigned temperature value.

The use of the single-phase model does not exclude the possibility to take into account for phenomena like the Brownian motion. In fact, the relations adopted to evaluate the thermal conductivity and viscosity consider the component linked to the Brownian motion as well as the particle diameter effects, and they were adopted by several authors, also in the case of nanofluid mixed convection [42, 43].

3. Physical Properties of Nanofluids

The working fluid is pure water or a water/Al₂O₃-based nanofluid. The nanoparticle diameter of 30 nm and different volume fractions equal to 1%, 3%, and 5% have been considered. In Table 1, the values of density, specific heat, dynamic viscosity, thermal conductivity, and thermal expansion coefficient, given by Rohsenow et al. [44], are reported

TABLE 1: Properties of pure water and Al₂O₃ particles at $T = 293$ K.

Material	ρ (kg/m ³)	c_p (J/kgK)	μ (Pas)	λ (W/mK)	β (1/K)
Al ₂ O ₃	3880	773	//	36	//
Water	998.2	4182	993×10^{-6}	0.597	2.1×10^{-4}

TABLE 2: Thermophysical properties of the working fluids.

ϕ	ρ (kg/m ³)	c_p (J/kgK)	μ (Pas)	λ (W/Mk)	β (1/K)
0%	998.2	4182	993×10^{-6}	0.597	2.100×10^{-4}
1%	1027	4053	1110×10^{-6}	0.617	2.098×10^{-4}
3%	1085	3816	1233×10^{-6}	0.643	2.093×10^{-4}
5%	1142	3603	1724×10^{-6}	0.664	2.086×10^{-4}

for pure water and Al₂O₃ particles at the reference temperature of 293 K. The concentration of nanoparticles influences the working fluid properties. The single-phase model was adopted. Thus, fluid properties must be evaluated by employing relations, available in the literature, in order to compute the thermal and physical properties of the considered nanofluids [29, 36, 40, 45, 46]. Their values are given in Table 2. Density was evaluated by using the classical formula valid for conventional solid-liquid mixtures, while the specific heat values and thermal expansion coefficient ones were calculated by assuming the thermal equilibrium between particles and surrounding fluid [36, 40, 46]

density:

$$\rho_{nf} = (1 - \phi)\rho_{bf} + \phi\rho_p, \quad (6)$$

specific heat:

$$(\rho c_p)_{nf} = (1 - \phi)(\rho c_p)_{bf} + \phi(\rho c_p)_p, \quad (7)$$

thermal expansion coefficient:

$$\frac{\beta_{nf}}{\beta_{bf}} = \frac{1}{((1 - \phi/\phi)(\rho_{bf}/\rho_p))\beta_{bf}} + \frac{1}{((\phi/1 - \phi)(\rho_{bf}/\rho_p) + 1)}. \quad (8)$$

For the viscosity as well as for thermal conductivity, formula given by [29, 40, 45] were adopted, because these relations are expressed as a function of particle volume concentration and diameter

dynamic viscosity:

$$\mu_{nf} = \mu_{bf} + \frac{\rho_p V_B d_p^2}{72C\delta}, \quad (9)$$

thermal conductivity:

$$\frac{\lambda_{nf}}{\lambda_{bf}} = 1 + 64.7\phi^{0.746} \left(\frac{d_{bf}}{d_p} \right)^{0.3690} \left(\frac{\lambda_p}{\lambda_{bf}} \right) Pr^{0.9955} Re^{1.2321}, \quad (10)$$

where $V_B = \sqrt{18K_b T / \pi \rho_p d_p}$ and K_b is the Boltzmann constant, given by $K_b = 1.36 \times 10^{-26}$; the other terms are given by:

$$C = \mu_{bf}^{-1} \left[(c_1 d_p + c_2) \phi + (c_3 d_p + c_4) \right], \quad (11)$$

with $c_1 = -0.000001133$, $c_2 = -0.000002771$, $c_3 = 0.00000009$ and $c_4 = -0.000000393$, and the distance between nanoparticles, δ , obtained by

$$\delta = \sqrt[3]{\frac{\pi}{6\phi}} d_p, \quad (12)$$

while $Pr = \mu / \rho_{bf} \alpha_{bf}$ and $Re = \rho_{bf} K_b T / 3\pi \mu^2 L_{bf}$ with L_{bf} is the mean free path of water (0.17 nm).

4. Geometrical Configuration and Data Reduction

A numerical thermal and fluid-dynamic study on a three-dimensional duct model with an equilateral triangular section was carried out. The total length L is 2.0 m, while the internal edge one l is 0.017 m, as shown in Figure 1; the consequent hydraulic diameter, $d_h = 4A/P_h$ is equal to 0.01 m. The duct includes a developing section at the entrance region with a length of 1.5 m and a 0.4 m long test section, followed by the outlet one. The working fluid is water or a mixture of water and Al_2O_3 nanoparticles with a diameter of 30 nm, at different volume fractions equal to 1%, 3% and 5%.

The dimensionless parameters of Reynolds number, Grashof number, Richardson number, Nusselt number, and friction factor are considered for the data reduction and they are expressed by:

$$Re = \frac{V d_h}{\nu}, \quad (13)$$

$$Gr = \frac{g \beta (T_w - T_{in}) d_h^3}{\nu^2}, \quad (14)$$

$$Ri = \frac{Gr}{Re^2}, \quad (15)$$

$$Nu_{av} = \frac{\dot{q} d_h}{(T_w - T_m) \lambda_f}, \quad (16)$$

$$f = 2\Delta P \frac{d_h}{L} \frac{1}{\rho V^2}, \quad (17)$$

where V is the average inlet velocity, \dot{q} is the heat flux, T_w and T_m represent the temperature of the surface and the fluid bulk one, respectively.

5. Numerical Model

The governing equations, reported in the previous section, are solved by means of the finite volume method by means of Fluent code [47]. A steady-state solution and a segregated method are chosen to solve the governing equations, which are linearized implicitly with respect to dependent variables

of the equation. A second-order upwind scheme is chosen for energy and momentum equations. The SIMPLE coupling scheme is chosen to couple pressure and velocity. The convergence criteria of 10^{-4} , 10^{-6} and 10^{-8} are assumed for the residuals of density, velocity components, and energy ones, respectively, for all the considered simulations. It is assumed that the incoming flow is laminar at ambient temperature and pressure. Reynolds number is set equal to 100 and different values of Grashof number, ranging from 0 to 50000, were considered. On the solid walls, the no-slip condition was applied and velocity inlet and outflow ones were given for inlet and outlet sections.

Four different unstructured mesh distributions were tested on a triangular sectioned duct at $Re = 100$ and 250 in order to perform the grid-independence analysis. They had 152190, 302778, 563104, and 1146232 nodes, respectively. The third grid case was adopted, because it ensured a good compromise between the computational time and the accuracy requirements. In fact, comparing the third and fourth configurations, differences of 0.58% and 0.19% at most were evaluated in terms of average Nusselt number and pressure coefficient, in the case of pure water.

The validation has been performed by comparing the numerical results for $Re = 100$ and $Ri = 0$ with literature data for T_1 boundary condition. For the local and average Nusselt number, the comparison has been accomplished with Wilbulswas results [21], presented as a function of the axial coordinate for the thermal entrance region, z^* , defined as $z^* = z / (d_h Re)$. For the friction factor, data from Fleming-Sparrow, Miller-Han, and Gangal [21] have been considered. Data reduction has been carried out by means of z^+ parameter, the axial coordinate for the hydrodynamic entrance region, given by $z^* = z / (d_h Pe)$, with the Peclet number, Pe , defined as $Pe = V d_h / \alpha$. The present numerical results in terms of average and local Nusselt number and friction factors are in good agreement with the given correlations, as shown in Figure 2. In particular, a difference of 3% is observed for local and average Nusselt number at most, while a maximum error of 1% is evaluated in terms of friction factor.

6. Results and Discussion

A computational analysis of a three-dimensional model, regarding the nanofluid mixed convection in a triangular cross-sectioned duct is considered. A uniform temperature has been applied on the duct walls, according to the considered Richardson number. The inlet velocities ensure the steady laminar regime, and they correspond to $Re = 100$. The working fluids are pure water or a water/ Al_2O_3 -based nanofluid at different volume fractions. The single-phase model approach is adopted. The range of the considered Richardson numbers and volume fractions are given below:

- (i) Reynolds number, $Re: 100$,
- (ii) Richardson number: 0.0, 0.1, 0.5, 1, 2, 3, and 5,
- (iii) particle concentrations, ϕ 0%, 1%, 3% and 5%.

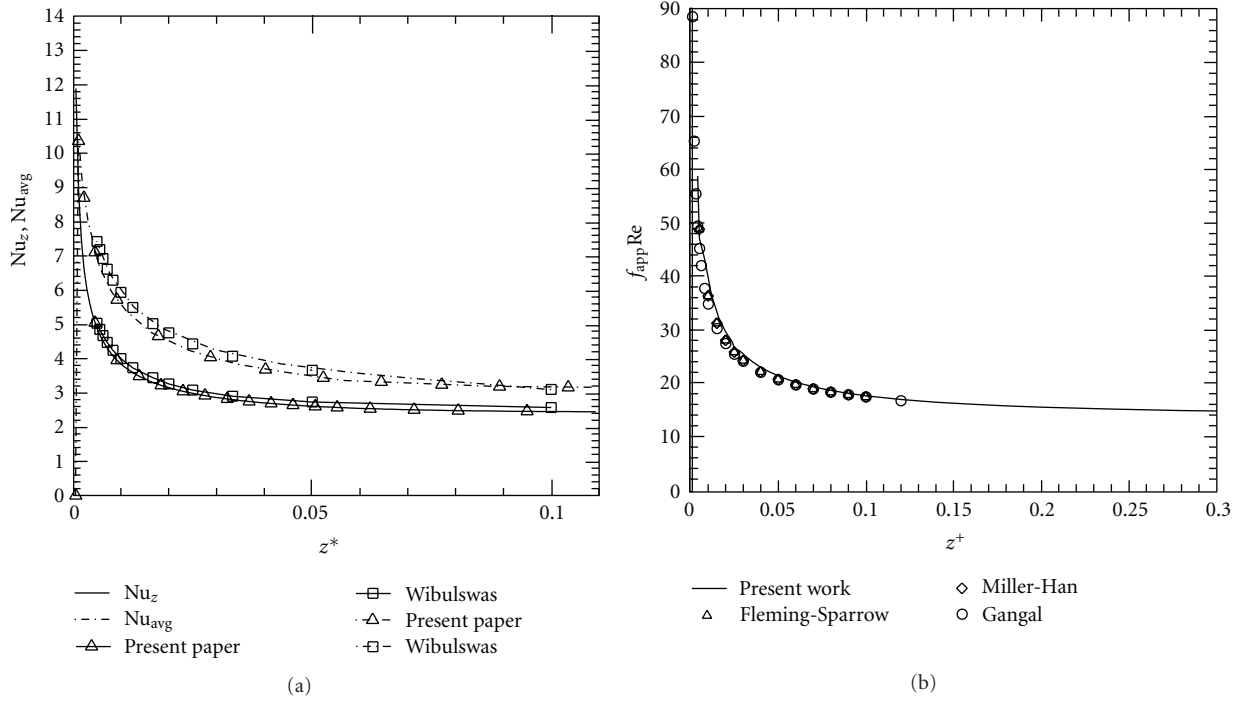


FIGURE 2: Validation of numerical results: (a) local and average Nusselt number; (b) friction factor.

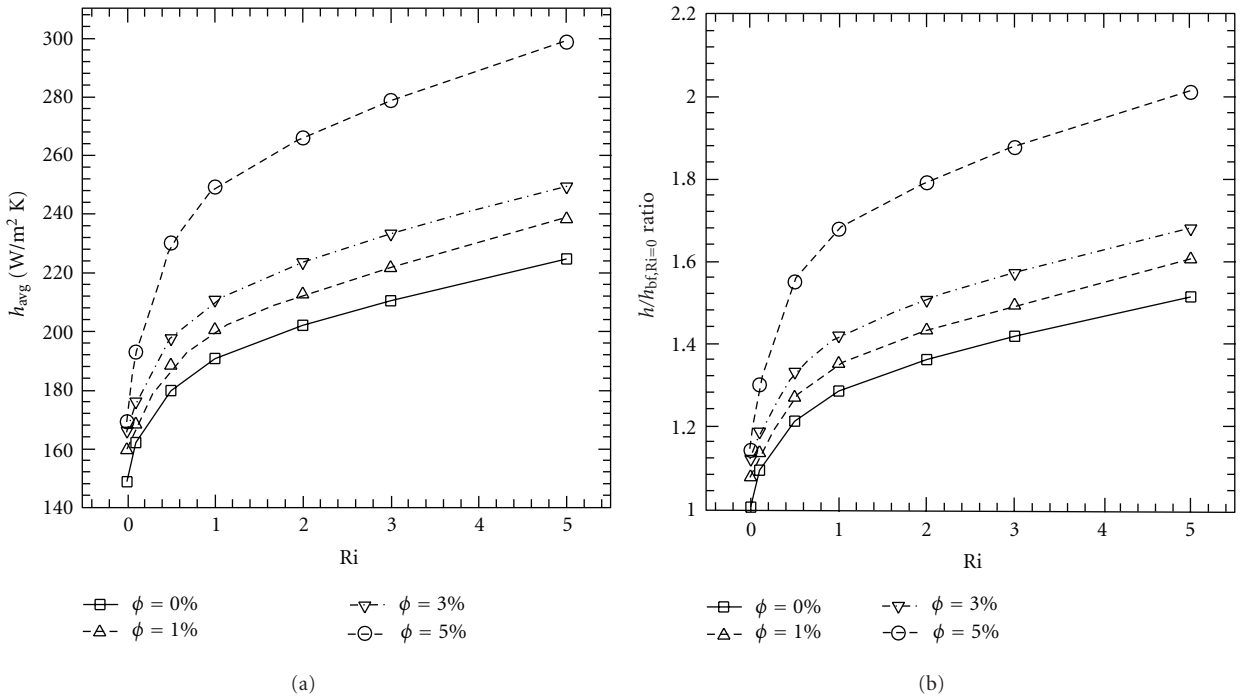


FIGURE 3: Convective heat transfer coefficient profiles as a function of Ri , $\phi = 0\%$, 1% , 3% and 5% : (a) average convective heat transfer coefficient; (b) average convective heat transfer coefficient enhancement, referred to pure water case at $Ri = 0$.

Results are presented in terms of average convective heat transfer coefficient, average Nusselt number, wall shear stress and required pumping power profiles in the test section.

Figure 3(a) depicts the average convective heat transfer coefficient profiles as a function of Ri for different values of

nanoparticle volume concentration. The effect of buoyancy leads to an increase in terms of heat transfer coefficients, and a sharp growth is detected at low Richardson numbers. In fact, in the case of pure water h_{avg} is equal to about 148, 162, 178, 190, and 225 W/m²K for $Ri = 0, 0.1, 0.5, 1, 5,$

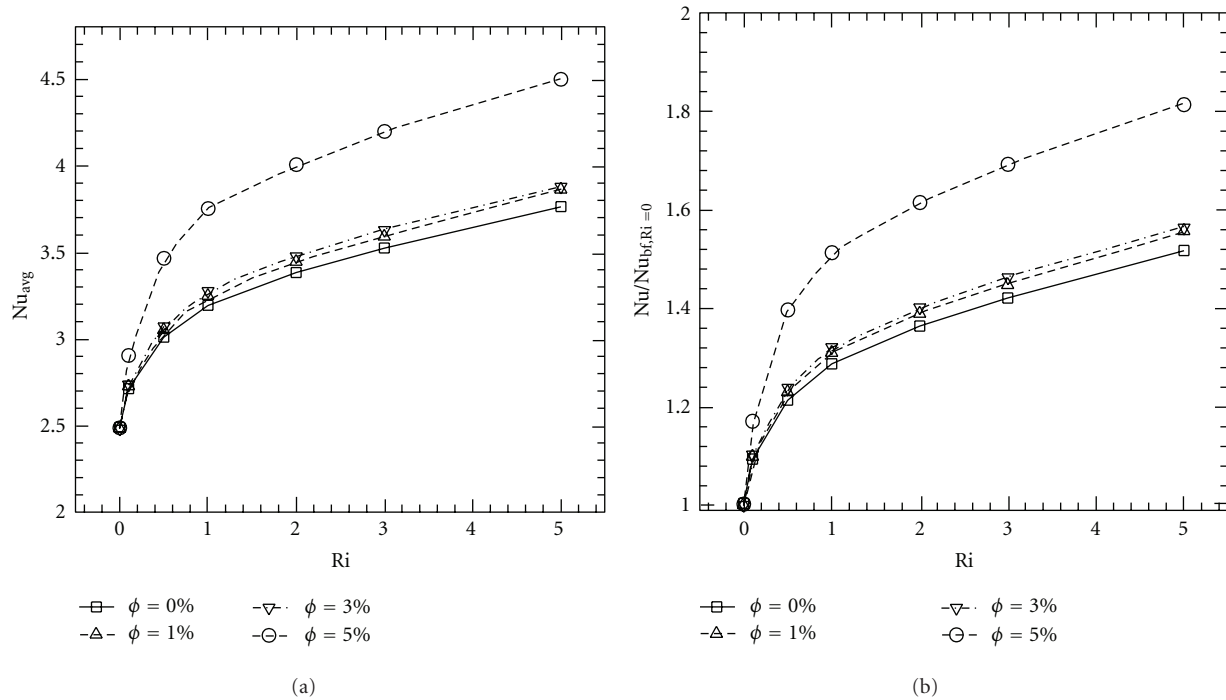


FIGURE 4: Nusselt number profiles as a function of Ri , $\phi = 0\%$, 1% , 3% and 5% : (a) average Nusselt number; (b) average Nusselt number enhancement, referred to pure water case at $Ri = 0$.

respectively. A similar behaviour is observed for the configurations with nanofluids. However, increasing values of convective heat transfer are evaluated as particle concentration increases. In fact, h_{avg} is equal to about 160, 170, 188, 199, 208, and 238 W/m^2K at $\phi = 1\%$ while at $\phi = 5\%$ h_{avg} is equal to about 168, 193, 230, 250, 266, and 298 W/m^2K for $Ri = 0, 0.1, 0.5, 1, 2$ and 5 , respectively. Figure 3(b) describes the average convective heat transfer enhancement in comparison with the pure water case at $Ri = 0$. The maximum improvement is detected for the cases, characterized by $\phi = 5\%$, which show heat transfer coefficient values equal to 1.14, 1.55, 1.68, and 2.01 times greater than the reference case for $Ri = 0, 0.5, 1$, and 5 . Smaller increases are observed for decreasing values of nanoparticle volume concentration. For example, the enhancement ratio is equal to 1.06, 1.26, 1.33, and 1.60 for $\phi = 1\%$ at $Ri = 0, 0.5, 1$ and 5 while for $\phi = 3\%$ it is equal to 1.10, 1.32, 1.41, and 1.68.

The average Nusselt profiles as a function of Ri for different values of nanoparticle volume concentration are presented in Figure 4(a). For fully developed laminar flow at $Ri = 0$, the average Nusselt number is equal to 2.47 for triangular ducts with walls at a uniform temperature. In mixed convection, the fully developed condition is reached much farther upstream than for pure forced convection, depending on the importance of buoyancy effects. However, average Nusselt number in the test section tends to increase as Ri and nanoparticle fraction increase. In fact, at $Ri = 5$, $Nu_{avg} = 3.76, 3.87, 3.90$, and 4.5 for at $\phi = 0\%, 1\%, 3\%$ and 5% . The consequent enhancement in terms of Nusselt number is depicted in Figure 4(b); it is less significant if compared with Figure 3 because of the nanofluid thermal

conductivity increase. In fact, for ϕ equal to 1% and 3% the average Nusselt number is 4% and 6% higher than the cases with pure water on average. A more significant enhancement is provided by the cases with $\phi = 5\%$.

The heat transfer enhancement is partly due to the increase of fluid velocity, because the simulations have been carried out at a constant Reynolds number. In fact, the increase of nanofluid viscosity is not balanced by the increase of density. Another possible reason is linked to the Brownian motion which could become very important in the case of laminar flow regime. However, a further analysis about the comparison criteria among the results in terms of heat transfer coefficients for base fluid and nanofluid is necessary as observed by Prabhat et al. [48].

The working fluid flows into a triangular cross-sectioned duct with walls at a uniform temperature; thus, the heat transfer mechanism is different if the bottom wall behaviour is compared with the inclined ones when the buoyancy effects are considered. In fact, the orientation of hot surfaces and their inclination must be taken into account even in internal flows. For $Ri = 0$ no differences are detected among the heated walls. Figure 5 allows to describe the different behaviour of bottom surface and upper ones. In general, convective heat transfer coefficient profiles result to be higher for *wall 1* for all the considered Ri values, as shown by Figure 5(a). Profiles tend to increase as Ri increases; in fact, for pure water h_{avg} is equal to about 210 and 370 W/m^2K for $Ri = 0.1$ and 5 , respectively. The introduction of nanoparticles leads to a significant enhancement of heat transfer coefficients even at low Ri numbers and particle concentration. For $\phi = 5\%$, the highest heat transfer coefficient value is detected for

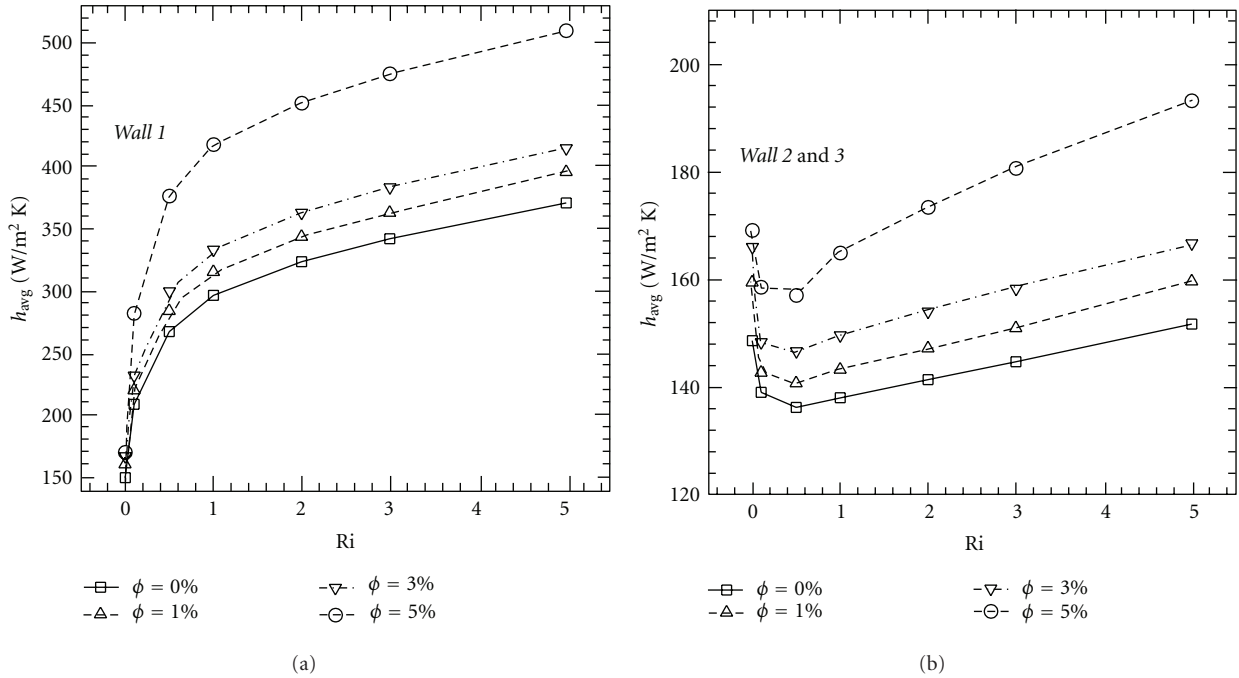


FIGURE 5: Average convective heat transfer coefficient profiles as a function of Ri , $\phi = 0\%$, 1% , 3% and 5% : (a) wall 1; (b) wall 2 and 3.

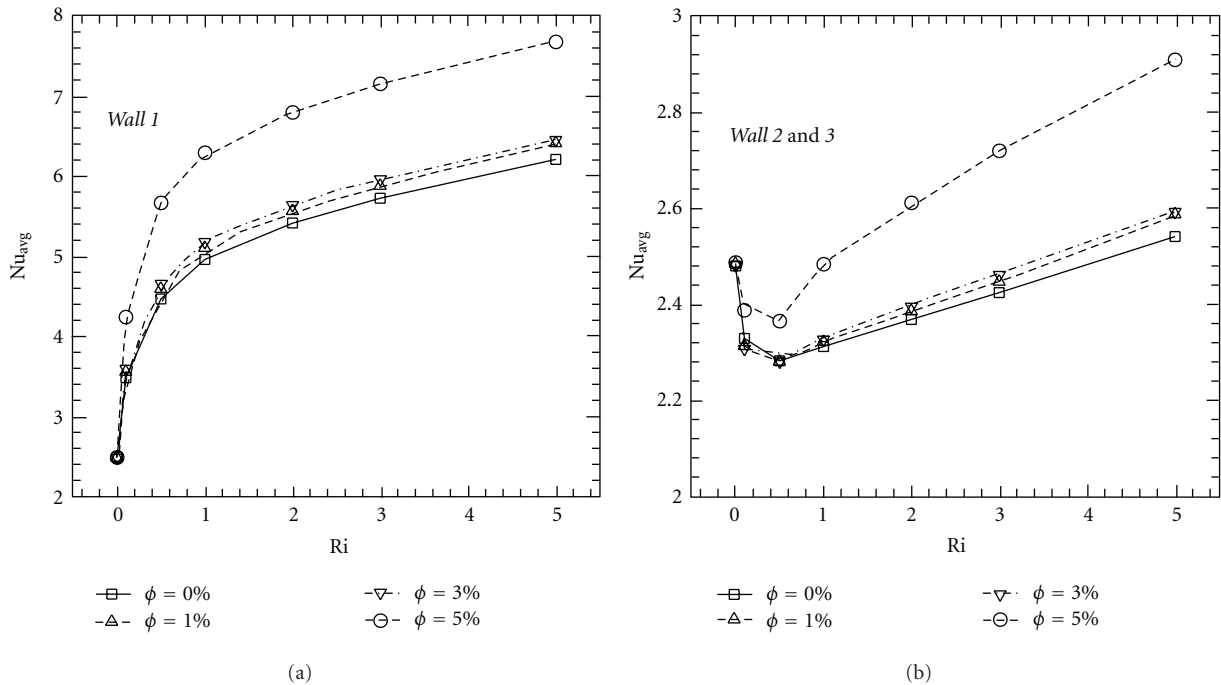


FIGURE 6: Average Nusselt number profiles as a function of Ri , $\phi = 0\%$, 1% , 3% and 5% : (a) wall 1; (b) wall 2 and 3.

$Ri = 5$, and it is equal to $510 \text{ W/m}^2\text{K}$. Wall 2 and 3 present smaller heat transfer coefficient values, as reported in Figure 5(b). In fact, at $Ri = 5h_{avg}$ is equal to 152, 160, 170, and $194 \text{ W/m}^2\text{K}$ for $\phi = 0\%$, 1% , 3% , and 5% , respectively. Moreover, for $Ri < 2$, buoyancy determines negative effects on the heat transfer mechanism if results are compared with ones obtained in the case of forced convection. The results in terms of average Nusselt number are shown in Figure 6.

The highest Nusselt numbers for wall 1 are equal to 6.2, 6.4, 6.5, and 7.7 for $\phi = 0\%$, 1% , 3% , and 5% , respectively; the profiles for wall 2 and wall 3 tends to decrease as Ri increases until Ri is equal to 1 for $\phi = 0\%$, 1% and 3% , and 1 for $\phi = 5\%$, then they increase.

The use of nanofluids as working fluids instead of pure water provides a heat transfer enhancement, according to the particle volume fraction, but it leads to increasing values of

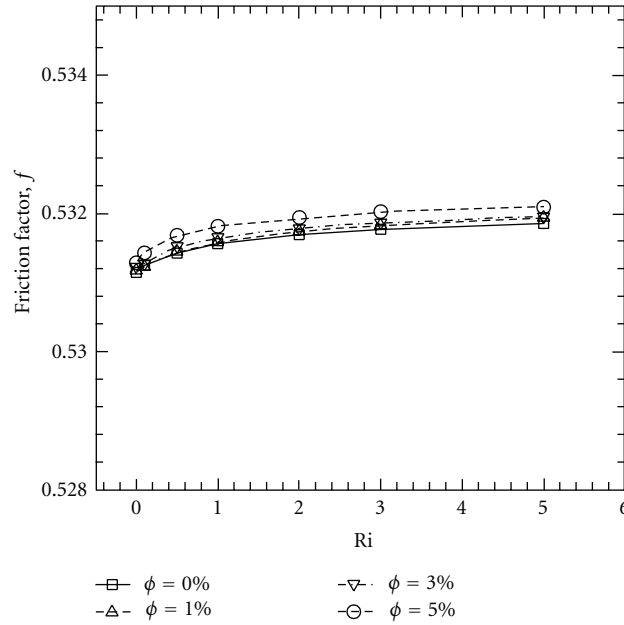


FIGURE 7: Friction factor profiles as a function of Ri, $\phi = 0\%$, 1%, 3% and 5%.

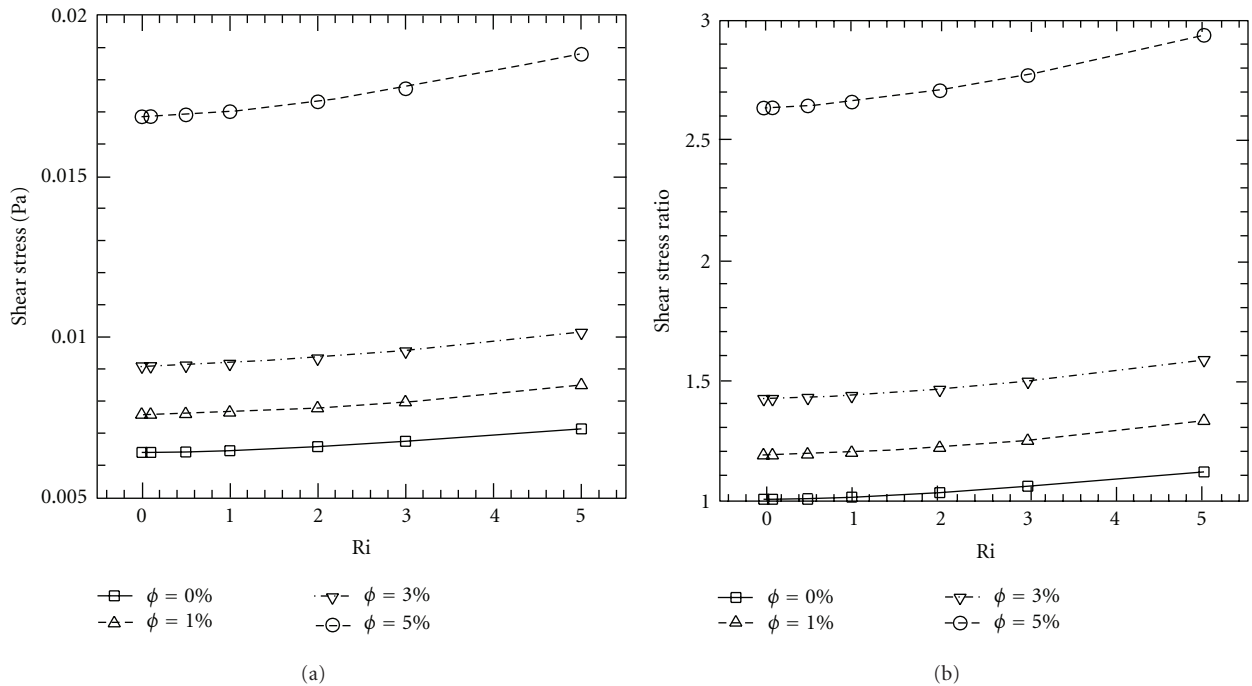


FIGURE 8: Wall shear stress profiles as a function of Ri, $\phi = 0\%$, 1%, 3% and 5%: (a) average wall shear stress; (b) average wall shear stress, referred to the pure water case at Ri = 0.

wall shear stress, while the friction factor keeps substantially constant as reported in Figure 7, because the flow is fully developed. The average wall shear stress profiles as a function of Ri are depicted in Figure 8(a). Values grow as the buoyancy effects become more significant. In fact, the highest values are observed at Ri = 5; moreover, wall shear stress increases as particle concentration increases and the maximum values are evaluated for $\phi = 5\%$. In fact, for $\phi = 5\%$ wall shear

stress is 2.63, 2.65, 2.68, 2.75, and 2.94 times higher than the value calculated at Ri = 0 with pure water, as depicted in Figure 8(b). For lower particle concentrations, wall shear stress ratio is smaller than the ones calculated at $\phi = 5\%$ and, for example, it is equal to 1.18, 1.20, and 1.32 for $\phi = 1\%$ and Ri = 0.1, 1, and 5, respectively, while it is equal to 1.40, 1.42, and 1.58 for $\phi = 3\%$. *Wall 1* is featured by higher wall shear stress values than the ones calculated for *wall 2* and

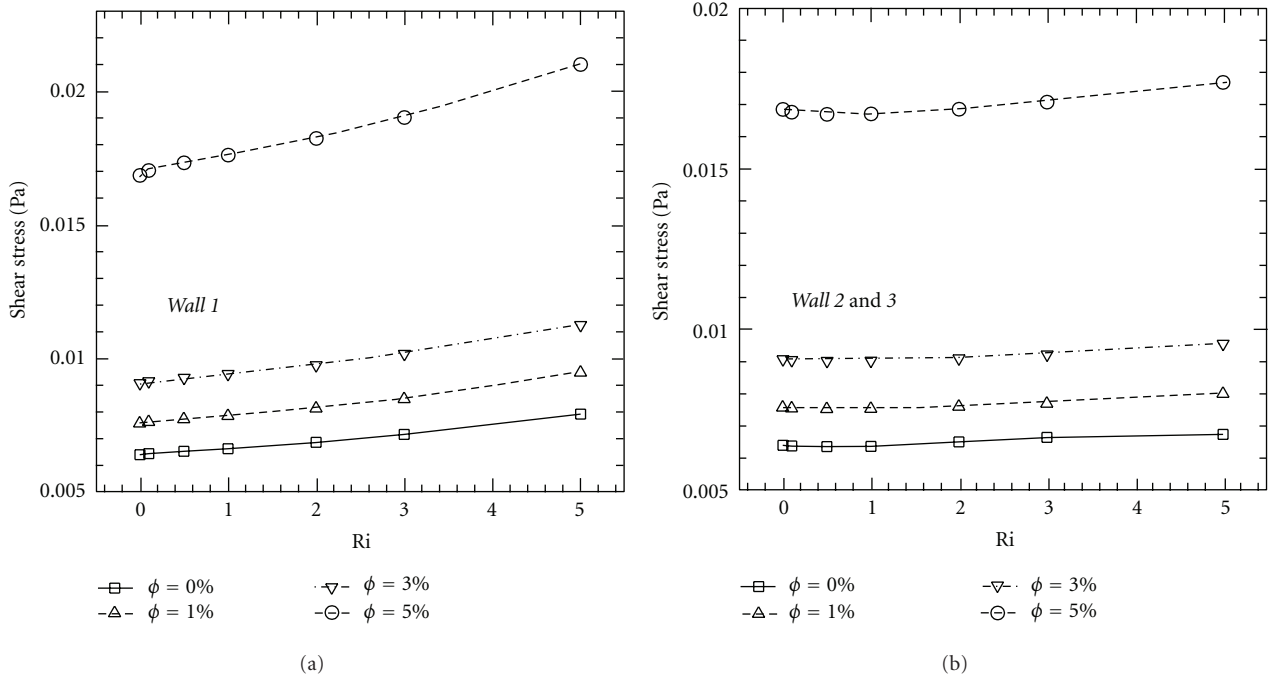


FIGURE 9: Average wall shear stress profiles as a function of Ri, $\phi = 0\%$, 1%, 3% and 5%: (a) wall 1; (b) wall 2 and 3.

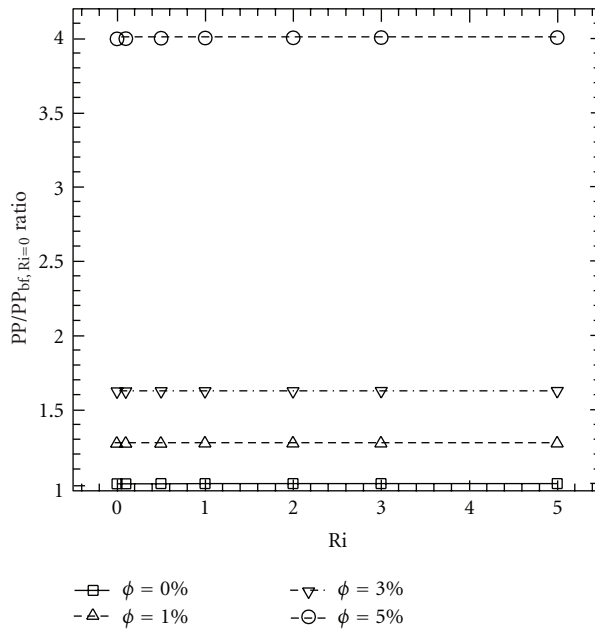


FIGURE 10: Required pumping power profiles, referred to the pure water case at $Ri = 0$, as a function of Ri, $\phi = 0\%$, 1%, 3% and 5%.

wall 3, as observed in Figure 9. Profiles increase as Ri, and nanoparticle concentration increases if wall 1 is considered, while they keep substantially constant in the case of wall 2 and wall 3. The friction factor keeps substantially constant as reported in Figure 7, because the flow is fully developed.

The required pumping power ratio profiles, referred to the water cases at $Ri = 0$, are carried out in Figure 10. Pumping power is defined as $PP = \dot{V}\Delta P$, and its profiles tend to increase as ϕ grows, while a very little dependence on Ri is

observed. The pumping power ratio is equal to 1.26, 1.61, and 4.0 for $\phi = 1\%$, 3%, and 5%, respectively.

Figures 11 and 12 describe the fully developed flow regime in terms of velocity and dimensionless temperature profiles for the vertical symmetry axis of the channel at $z/d_h = 125$ and 150. Figure 11 shows that u/u_{max} profiles substantially overlap each other for different values of particle concentration and Richardson number. The highest values are detected at y/h equal to about 0.30, while

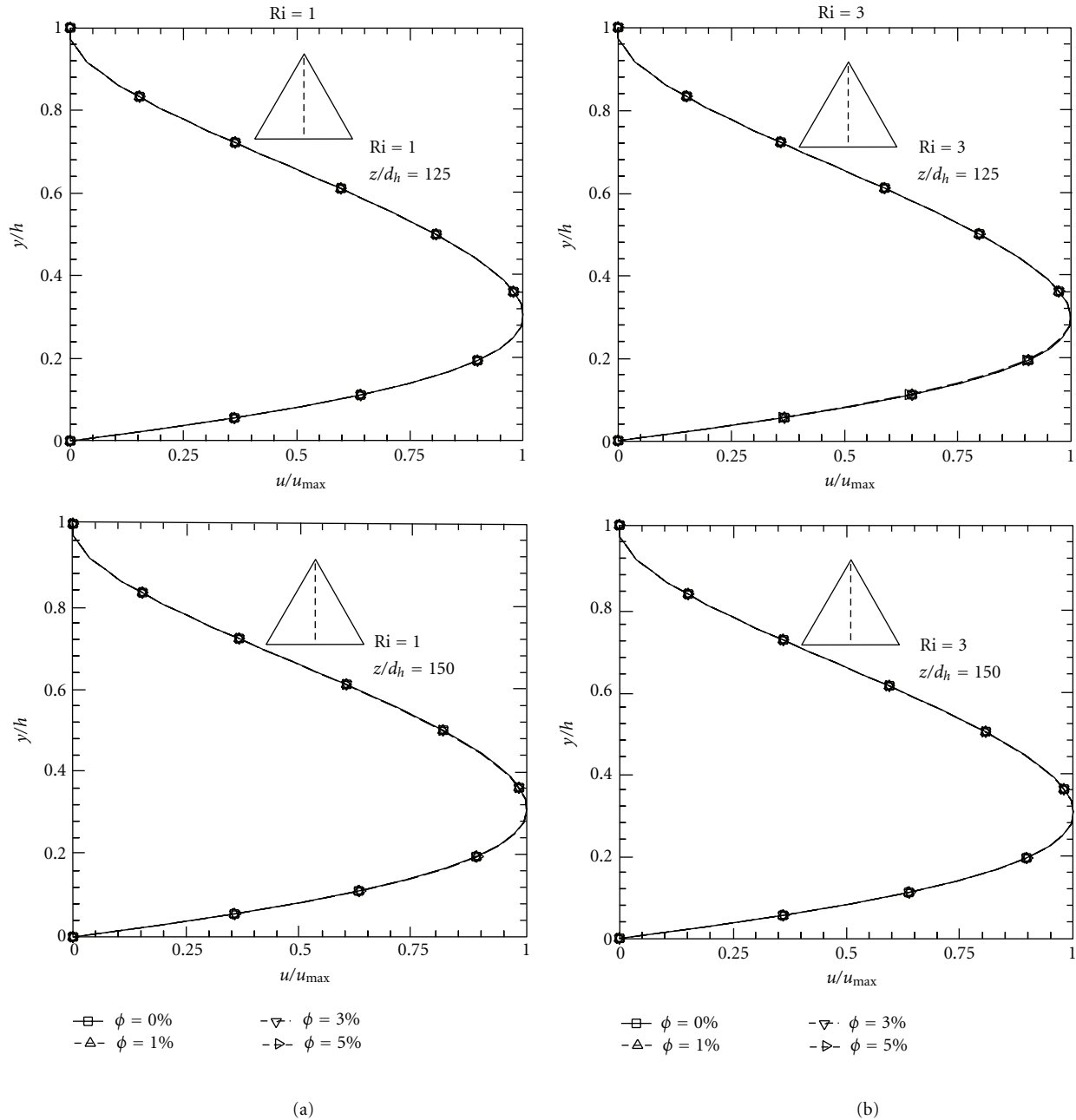


FIGURE 11: Velocity profiles for different values of particle concentration and $Ri = 1$ and 3 : (a) $z/d_h = 125$; (b) $z/d_h = 150$.

the maximum values of dimensionless temperature, defined as $T^* = (T - T_w)/(T_m - T_w)$, is evaluated at y/h equal to about 0.20. The temperature profiles keep similar if they are compared at the same values of Ri and volume particle concentration, as shown in Figure 12.

7. Conclusions

In this paper, a numerical investigation about the laminar mixed convection in water/ Al_2O_3 -based nanofluids flowing into a triangular sectioned duct is carried out. The laminar flow regime was considered at $Re = 100$, and Ri numbers ranging from 0 to 5 were assumed. A constant and uniform

temperature is applied on the duct walls, depending on the Ri number. The single-phase model was adopted in order to analyze the behaviour in the case of nanofluids as working fluid. Thus, the considered nanoparticle volume concentrations were equal to 0%, 1%, 3%, and 5%.

The introduction of nanoparticles significantly raises the convective heat transfer coefficients as particle concentration grows as well as Ri number. This effect is very significant at low Ri numbers. In fact, the maximum improvement is detected for the cases, characterized by $\phi = 5\%$, which show heat transfer coefficient values equal to 1.14, 1.55, 1.68, and 2.01 times greater than the pure water case at $Ri = 0$. However, the wall shear stress and the required pumping

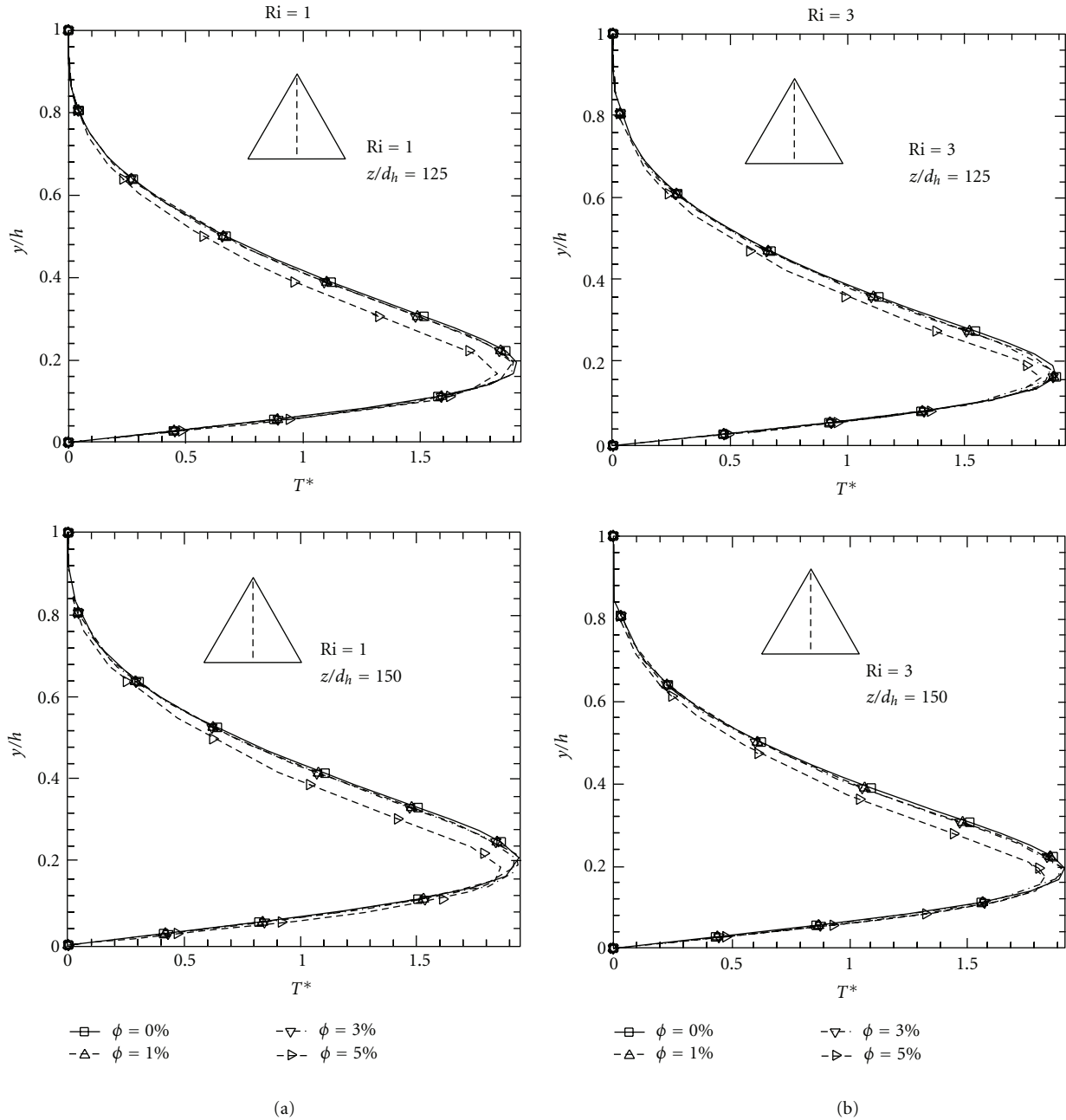


FIGURE 12: Dimensionless temperature profiles for different values of particle concentration and $Ri = 1$ and 3 : (a) $z/d_h = 125$; (b) $z/d_h = 150$.

power increase, and their values become very high at high concentrations. This effect is amplified at low Ri numbers, and an increase of about 30% in terms of wall shear stress is evaluated at $Ri = 0$ and 0.1 in comparison with the pure water results. Moreover, the pumping power ratio, referred to the pure water cases at $Ri = 0$, is equal to 1.26, 1.61, and 4.0 for $\phi = 1\%$, 3% , and 5% , respectively.

It should be remarked that further investigations need to be accomplished in order to understand the main physical reasons of the heat enhancement using the nanofluids in laminar regime, particularly, in mixed convection, as underlined in [48].

Nomenclature

- A : Cross-section area (m^2)
- c_p : Specific heat (J/kgK)
- d : Diameter (m)
- f : Friction factor (17)
- g : Gravitational acceleration (m/s^2)
- Gr : Grashof number (14)
- H : Duct height (m)
- h : Heat transfer coefficient (W/m^2K)
- l : Duct internal edge length (m)
- L : Duct length (m)

Nu:	Nusselt number(16)
P :	Pressure (Pa)
Pe:	Peclet number
PP:	Required pumping power (W)
q :	Target surface heat flux (W/m ²)
Re:	Reynolds number(13)
Ri:	Richardson number(15)
T :	Temperature (K)
u, v, w :	Velocity components (m/s)
V :	Average velocity (m/s)
\dot{V} :	Volume flow rate (m ³ /s)
x, y, z :	Spatial coordinates (m)
α :	Thermal diffusivity (m ² /s)
β :	Volumetric expansion coefficient (1/K)
δ :	Distance between nanoparticles (m)
λ :	Thermal conductivity (W/mK)
μ :	Dynamic viscosity (Pas)
ν :	Kinematic viscosity (m ² /s)
ρ :	Density (kg/m ³)
ϕ :	Nanoparticle volumetric concentration
avg:	Average
bf:	Base fluid
f :	Fluid
h :	Hydraulic
m :	Mass
nf:	Nanofluid
p :	Particle
w :	Wall.

Acknowledgment

This work was supported by SUN with a 2010 grant and by MIUR with Articolo D.M. 593/2000 Grandi Laboratori "EliosLab."

References

- [1] I. Uzun and M. Unsal, "A numerical study of laminar heat convection in ducts of irregular cross-sections," *International Communications in Heat and Mass Transfer*, vol. 24, no. 6, pp. 835–848, 1997.
- [2] Y. Asako and M. Faghri, "Three-dimensional laminar heat transfer and fluid flow characteristics in the entrance region of a rhombic duct," *Journal of Heat Transfer*, vol. 110, no. 4, pp. 855–861, 1988.
- [3] R. K. Shah, "Laminar flow friction and forced convection heat transfer in ducts of arbitrary geometry," *International Journal of Heat and Mass Transfer*, vol. 18, no. 7-8, pp. 849–862, 1975.
- [4] S. R. Montgomery and P. Wibulswas, "Laminar flow heat transfer ducts of rectangular cross-section," in *Proceedings of the 3rd International Heat Transfer Conference*, pp. 85–96, New York, NY, USA, 1966.
- [5] K. Velusamy, V. K. Garg, and G. Vaidyanathan, "Fully developed flow and heat transfer in semi-elliptical ducts," *International Journal of Heat and Fluid Flow*, vol. 16, no. 2, pp. 145–152, 1995.
- [6] R. Gupta, P. E. Geyer, D. F. Fletcher, and B. S. Haynes, "Thermohydraulic performance of a periodic trapezoidal channel with a triangular cross-section," *International Journal of Heat and Mass Transfer*, vol. 51, no. 11-12, pp. 2925–2929, 2008.
- [7] C. W. Leung and S. D. Probert, "Forced-convective internal cooling of a horizontal equilateral-triangle cross-sectioned duct," *Applied Energy*, vol. 50, no. 4, pp. 313–321, 1995.
- [8] W. M. Kays and A. L. London, *Compact Heat Exchangers*, McGraw-Hill, New York, NY, USA, 3rd edition, 1984.
- [9] L. Zhang, "Laminar flow and heat transfer in plate-fin triangular ducts in thermally developing entry region," *International Journal of Heat and Mass Transfer*, vol. 50, no. 7-8, pp. 1637–1640, 2007.
- [10] P. Talukdar and M. Shah, "Analysis of laminar mixed convective heat transfer in horizontal triangular ducts," *Numerical Heat Transfer, Part A*, vol. 54, no. 12, pp. 1148–1168, 2008.
- [11] A. Lawal, "Mixed convection heat transfer to power law fluids in arbitrary cross-sectional ducts," *Journal of Heat Transfer*, vol. 111, no. 2, pp. 399–405, 1989.
- [12] G. E. Schneider and B. L. LeDain, "Fully developed Laminar heat transfer in triangular passages," *Journal of Energy*, vol. 5, no. 1, pp. 15–21, 1981.
- [13] R. W. Hanks and R. C. Cope, "Laminar-turbulent transitional flow phenomena in isosceles triangular cross-section ducts," *American Institute of Chemical Engineers Journal*, vol. 16, no. 4, pp. 528–535, 1970.
- [14] C. A. C. Altemani and E. M. Sparrow, "Turbulent heat transfer and fluid flow in an unsymmetrically heated triangular duct," *Journal of Heat Transfer*, vol. 102, no. 4, pp. 590–597, 1980.
- [15] C. W. Leung, T. T. Wong, and H. J. Kang, "Forced convection of turbulent flow in triangular ducts with different angles and surface roughnesses," *Heat and Mass Transfer/Waerme- und Stoffuebertragung*, vol. 34, no. 1, pp. 63–68, 1998.
- [16] M. Bahrami, M. Michael Yovanovich, and J. Richard Culham, "A novel solution for pressure drop in singly connected microchannels of arbitrary cross-section," *International Journal of Heat and Mass Transfer*, vol. 50, no. 13-14, pp. 2492–2502, 2007.
- [17] K. Rehme, "Simple method of predicting friction factors of turbulent flow in non-circular channels," *International Journal of Heat and Mass Transfer*, vol. 16, no. 5, pp. 933–950, 1973.
- [18] Y. G. Lai, "An unstructured grid method for a pressure-based flow and heat transfer solver," *Numerical Heat Transfer, Part B*, vol. 32, no. 3, pp. 267–281, 1997.
- [19] S. Chen, T. L. Chan, C. W. Leung, and B. Yu, "Numerical prediction of laminar forced convection in triangular ducts with unstructured triangular grid method," *Numerical Heat Transfer, Part A*, vol. 38, no. 2, pp. 209–224, 2000.
- [20] S. Syrjala, "Accurate prediction of friction factor and nusselt number for some duct flows of power-law non-newtonian fluids," *Numerical Heat Transfer, Part A*, vol. 41, no. 1, pp. 89–100, 2002.
- [21] R. K. Shah and A. L. London, *Laminar Flow Forced Convection in Ducts*, Academic Press, New York, NY, USA, 1978.
- [22] M. E. Ali and H. Al-Ansary, "Natural convection heat transfer from vertical triangular ducts," in *Proceedings of the 2009 ASME Summer Heat Transfer Conference, (HT '09)*, vol. 2, pp. 421–428, San Francisco, Calif, USA, July 2009.
- [23] A. E. Bergles, "Some perspective on enhanced heat transfer, second-generation heat transfer technology," *Journal of Heat Transfer*, vol. 110, no. 4, pp. 1082–1096, 1988.
- [24] R. L. Webb and N. H. Kim, *Principles of Enhanced Heat Transfer*, Taylor & Francis Group, New York, NY, USA, 2nd edition, 2005.
- [25] J. Buongiorno, "Convective transport in nanofluids," *Journal of Heat Transfer*, vol. 128, no. 3, pp. 240–250, 2006.
- [26] S. U. S. Choi, "Nanofluids: from vision to reality through research," *Journal of Heat Transfer*, vol. 131, no. 3, pp. 1–9, 2009.

- [27] O. Manca, P. Mesolella, S. Nardini, and D. Ricci, "Numerical study of a confined slot impinging jet with nanofluids," *Nanoscale Research Letters*, vol. 6, pp. 1–16, 2011.
- [28] Y. Xuan and Q. Li, "Heat transfer enhancement of nanofluids," *International Journal of Heat and Fluid Flow*, vol. 21, no. 1, pp. 58–64, 2000.
- [29] C. H. Chon, K. D. Kihm, S. P. Lee, and S. U. S. Choi, "Empirical correlation finding the role of temperature and particle size for nanofluid (Al₂O₃) thermal conductivity enhancement," *Applied Physics Letters*, vol. 87, no. 15, Article ID 153107, pp. 1–3, 2005.
- [30] B. C. Pak and Y. I. Cho, "Hydrodynamic and heat transfer study of dispersed fluids with submicron metallic oxide particles," *Experimental Heat Transfer*, vol. 11, no. 2, pp. 151–170, 1998.
- [31] I. Gherasim, G. Roy, C. T. Nguyen, and D. Vo-Ngoc, "Heat transfer enhancement and pumping power in confined radial flows using nanoparticle suspensions (Nanofluids)," *International Journal of Thermal Sciences*, vol. 50, pp. 369–377, 2010.
- [32] P. Keblinski, R. Prasher, and J. Eapen, "Thermal conductance of nanofluids: is the controversy over?" *Journal of Nanoparticle Research*, vol. 10, no. 7, pp. 1089–1097, 2008.
- [33] J. Buongiorno, D. C. Venerus, N. Prabhat et al., "A benchmark study on the thermal conductivity of nanofluids," *Journal of Applied Physics*, vol. 106, no. 9, Article ID 094312, 2009.
- [34] Y. Xuan and Q. Li, "Investigation on convective heat transfer and flow features of nanofluids," *Journal of Heat Transfer*, vol. 125, no. 1, pp. 151–155, 2003.
- [35] D. Wen and Y. Ding, "Experimental investigation into convective heat transfer of nanofluids at the entrance region under laminar flow conditions," *International Journal of Heat and Mass Transfer*, vol. 47, no. 24, pp. 5181–5188, 2004.
- [36] S. E. B. Maiga, C. T. Nguyen, N. Galanis, and G. Roy, "Heat transfer behaviours of nanofluids in a uniformly heated tube," *Superlattices and Microstructures*, vol. 35, no. 3–6, pp. 543–557, 2004.
- [37] R. Ben Mansour, N. Galanis, and C. T. Nguyen, "Experimental study of mixed convection with water-Al₂O₃ nanofluid in inclined tube with uniform wall heat flux," *International Journal of Thermal Sciences*, vol. 50, pp. 403–410, 2010.
- [38] S. Maiga, S. J. Palm, C. T. Nguyen, G. Roy, and N. Galanis, "Heat transfer enhancement by using nanofluids in forced convection flows," *International Journal of Heat and Fluid Flow*, vol. 26, no. 4, pp. 530–546, 2005.
- [39] S. E. B. Maiga, C. T. Nguyen, N. Galanis, G. Roy, T. Maré, and M. Coqueux, "Heat transfer enhancement in turbulent tube flow using Al₂O₃ nanoparticle suspension," *International Journal of Numerical Methods for Heat and Fluid Flow*, vol. 16, no. 3, pp. 275–292, 2006.
- [40] M. Akbari and A. Behzadmehr, "Developing mixed convection of a nanofluid in a horizontal tube with uniform heat flux," *International Journal of Numerical Methods for Heat and Fluid Flow*, vol. 17, no. 6, pp. 566–576, 2007.
- [41] S. Mirmasoumi and A. Behzadmehr, "Numerical study of laminar mixed convection of a nanofluid in a horizontal tube using two-phase mixture model," *Applied Thermal Engineering*, vol. 28, no. 7, pp. 717–727, 2008.
- [42] S. Allahyari, A. Behzadmehr, and S. M. H. Sarvari, "Conjugate heat transfer of laminar mixed convection of a nanofluid through an inclined tube with circumferentially non-uniform heating," *Nanoscale Research Letters*, vol. 6, no. 1, pp. 1–13, 2011.
- [43] S. Allahyari, A. Behzadmehr, and S. M. H. Sarvari, "Conjugate heat transfer of laminar mixed convection of a nanofluid through a horizontal tube with circumferentially non-uniform heating," *International Journal of Thermal Sciences*, vol. 50, pp. 1963–1972, 2011.
- [44] W. M. Rohsenow, J. P. Hartnett, and Y. I. Cho, *Handbook of Heat Transfer*, McGraw-Hill, New York, NY, USA, 3rd edition, 1998.
- [45] N. Masoumi, N. Sohrabi, A. Behzadmehr, and S. M. H. Sarvari, "A new model for calculating the effective viscosity of nanofluids," *Journal of Physics D*, vol. 42, no. 5, Article ID 055501, 2009.
- [46] K. Khanafer, K. Vafai, and M. Lightstone, "Buoyancy driven heat transfer enhancement in a two-dimensional enclosure utilizing nanofluids," *International Journal of Heat and Mass Transfer*, vol. 46, no. 19, pp. 3639–3653, 2003.
- [47] Fluent Inc., "FLUENT computational fluid dynamic code version 6.3 user guide," 2006, <http://www.fluent.com/>.
- [48] N. Prabhat, J. Buongiorno, and L. Hu, "Convective heat transfer enhancement in nanofluids: real anomaly or analysis artifact?" in *Proceedings of the ASME/JSME 8th Thermal Engineering Joint Conference, (AJTEC '11)*, Honolulu, Hawaii, USA, March 2011.

Research Article

Water-Based Fe₂O₃ Nanofluid Characterization: Thermal Conductivity and Viscosity Measurements and Correlation

L. Colla, L. Fedele, M. Scattolini, and S. Bobbo

Consiglio Nazionale delle Ricerche, Istituto per le Tecnologie della Costruzione, Corso Stati Uniti, 4, 35127 Padova, Italy

Correspondence should be addressed to S. Bobbo, sergio.bobbo@itc.cnr.it

Received 12 July 2011; Revised 19 September 2011; Accepted 19 September 2011

Academic Editor: Oronzio Manca

Copyright © 2012 L. Colla et al. This is an open access article distributed under the Creative Commons Attribution License, which permits unrestricted use, distribution, and reproduction in any medium, provided the original work is properly cited.

An experimental investigation on water-based nanofluids containing iron oxide (Fe₂O₃) in concentrations ranging between 5 and 20% in mass is presented. The purpose of this study is to measure thermal conductivity and dynamic viscosity of these fluids, as a starting point to study the heat transfer capability. The stability of the nanofluids was verified by pH and Zeta potential measurements. A dynamic light scattering (DLS) technique was used to obtain the mean nanoparticle diameters. It was found that thermal conductivity of these nanofluids improved with temperature and particles concentration. The temperature and nanoparticle concentration effects on viscosity were analyzed, obtaining a significant increase with respect to water. All the fluids exhibited a Newtonian behaviour. The experimental values were compared with some theoretical models for both thermal conductivity and dynamic viscosity.

1. Introduction

Several solutions have been proposed to enhance the thermal performance of the heat transfer devices. The most common technique has been maximizing heat transfer area in heat exchangers, but, at the moment, it seems no further improvement could be achieved. Another possibility is given by increasing heat transfer coefficient h that, for an imposed flux, depends on the thermal properties of the fluid. Aiming to improve the characteristics of the traditional working fluids (as water, glycol, oil, and refrigerants), a new generation of thermal vectors, called *nanofluids*, has emerged. Nanofluids are suspensions of nanosized solid particles (1–100 nm) in liquids. These new suspensions may be utilised in several applications, for example, engine cooling, engine transmission oil, cooling electronics, refrigeration, drilling, lubrications, thermal storage, solar water heating, and so forth [1].

In the last decade, several papers have been published on the preparation and characterization of these fluids, but they are often not coherent and the results are inconsistent.

This could be due to the difference in their preparation methods and, consequently, on their stability. There are two

main procedures to obtain nanofluids, one is the one-step method and consists on synthesizing the particles directly into the fluid, the second is the two-step method and it implies the dispersion of nanopowders in the based fluid [2]. These methods influence the stability of the fluids and then their properties [3]. Nanosized particles have high-energy surface. For example, in 4 nm diameter particle ca, 50% of the atoms are at the surface, and, therefore, surface properties and chemistry control the nanoparticle behaviour [4]. In aqueous environments, there is a tendency for nanoparticles to aggregate, to reduce the particle surface energy. It depends on a number of factors including surface functionalization, pH, and ionic strength. For this reason, a pH optimization is fundamental [5], and often different dispersants and surfactants are added to the nanofluids [6].

Moreover, different methods of nanoparticles dispersion into the base fluid (ball milling, ultrasonication, homogenization) can lead to a different stability [7, 8].

For this reason, before studying thermophysical properties, a stability investigation must be done.

In literature, many studies on the thermal conductivity of nanofluids have been published highlighting significant

enhancement in this property [9–11], but some results are controversial and the mechanisms behind exceptional conductivity enhancement is still not well understood.

On the contrary, viscosity data in literature are still scarce even if this property is fundamental as well as thermal conductivity. Too high viscosity increase can nullify the positive effects of thermal conductivity enhancement.

Oxide nanoparticles are easier to get and less expensive than other nanoparticles, as metals and carbon nanotubes. Amongst them, Fe_2O_3 is already used to produce stable and commercially available water nanofluids, but, at our knowledge, no thermal conductivity data and only few experimental viscosity data are available in the literature.

For this reason, in this investigation, we study the effect of temperature and nanoparticles concentration on thermal conductivity and dynamic viscosity of Fe_2O_3 water-based nanofluids.

We compare our results with some literature models, and we propose an experimental correlation for nanofluids viscosity.

2. Nanofluid Preparation and Experimental Apparatus

2.1. Nanofluid Preparation. The studied nanofluid is formed by hematite (Fe_2O_3) nanoparticles, monodispersed in deionized water. It was supplied by Sigma Aldrich at a nanoparticles nominal concentration of 20% by mass.

Bidistilled water (Carlo Erba, CAS Nr 7732-18-5) was added to the commercial nanofluid to obtain the other two nanofluid compositions: 5 wt% and 10 wt%.

These two compositions were prepared taking the original nanofluid after one hour of sonication, by means of an ultrasonic bath (Bransonic, Ultrasonic cleaner Branson 2210, output power 90 W) and adding bidistilled water in a weighed amount, measured by an analytical balance (Gibertini E42S 240 g FS), with an uncertainty of 0.002 g. Each fluid obtained in this way was further sonicated for one hour, in order to improve the dispersion of nanoparticles in the water.

No dispersant has been added to the fluid.

2.2. Nanofluids Stability Characterization. A Zetasizer Nano ZS (Malvern), based on dynamic light scattering (DLS), was used to check the actual average dimension of the nanoparticles in solution. The mean particle diameter was around 67 nm, and it did not change with the particle concentration. In Figure 1, the particle size distribution detected by the Zetasizer is represented. A further particle size measurement was performed after almost three months, and the same average diameter was found. This indicates that no aggregation occurs in few months.

The Zetasizer Nano ZS also measures the Zeta potential of nanoparticles that quantify the magnitude of the electrical charge at the double layer. A value of Zeta potential out of the range between 30 mV and -30 mV indicates high charged surface and hence a strong electrical repulsion among the particles. Fe_2O_3 -water nanofluid Zeta potential was around

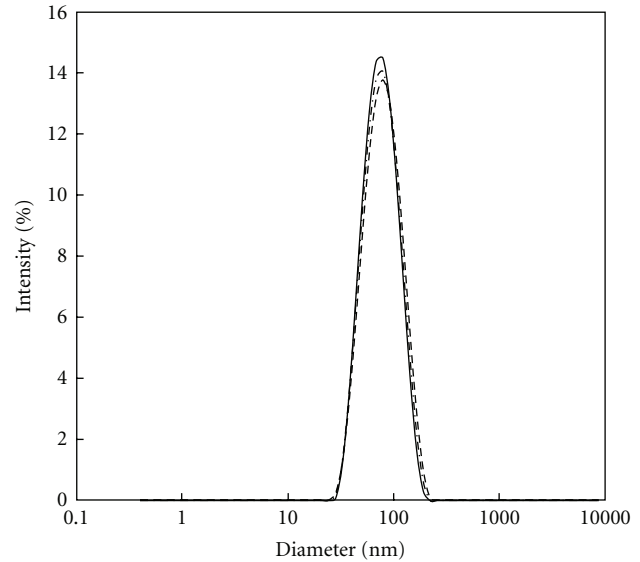


FIGURE 1: Nanoparticles size distribution for water containing 5 wt% (\cdots), 10 wt% (—), 20 wt% (---) Fe_2O_3 .

+56 mV for the 5 wt% solution, +57 mV for the 10 wt% solution, and +49 mV for the 20 wt% solution, therefore all the nanofluids seem to be very stable.

The pH of each nanofluid has been measured with a pH Meter (CRISON GPL 21) with a pH electrode (code 50 11 T). The measured values were 3.45 for the 5 wt% solution, 3.33 for 10 wt%, and 3.34 for 20 wt% at 26°C . As described in [12], the isoelectric point for water-hematite nanofluid is observed at pH 6.1. Then, the measured pH values of these solutions are far from this point, as further confirmation, together to the Zeta potential (always positive and higher than 30 mV), of the nanofluids stability.

2.3. Thermal Conductivity Measurement Apparatus. A TPS 2500 S was used for thermal conductivity measurements. The instrument is based on the hot-disk technique and can measure thermal conductivity and thermal diffusivity of several materials. The hot disk sensor is made of a double spiral of thin nickel wire and works as a continuous plane heat source. During the experiment, a small constant current is supplied to the sensor, which also serves as a temperature sensor, so that the temperature increase in the sensor is accurately determined through resistance measurement. The temperature increase is registered over a short period of time after the start of the experiment. A theoretical description of this method is provided by [13].

A proper box containing the sensor and the fluid was put in a water thermostatic bath to reach the test temperature.

The power supplied for each measurement was 30 mW, and the time of the power input was 4 s. The declared instrument uncertainty is 5%.

2.4. Dynamic Viscosity Measurement Apparatus. The dynamic viscosity data were measured at ambient pressure and in a temperature range between 283.15 K and 343.15 K, with

steps of 20 K, by means of an AR-G2 rheometer (TA Instruments). It is a rotational rheometer with magnetic bearing for ultra-low nanotorque control. The suitable employed geometry is a plate-cone type, with a 1° cone and diameter of 40 mm. In order to stabilize the measurement temperature, a proper device (Upper Heated Plate) was used. A critical point in this measurement is the sample loading. After some trials with water, a constant quantity of about 0.34 mL was considered optimal for the analysis. The sample was deposited using a pipette, taking care no air bubbles were inside. Before the measurements, the rheometer was carefully calibrated at each temperature, as fully described in [14].

All the measurements were performed at constant temperature and variable shear rate, starting from 80 1/s to 1200 1/s, at constant step of about 124 1/s (except for temperature 343.15 K, at which faster measurements had to be performed due to the water evaporation). A conditioning step of 2 seconds at a preshear rate of 80 1/s was performed before the measurements.

The estimated uncertainty in the viscosity measurements is about 5%.

3. Results and Discussion

3.1. Thermal Conductivity. The measurements accuracy was assessed measuring water thermal conductivity at each temperature and comparing it with Refprop 8.0, which was assumed as [15]. The absolute average deviation between experimental data and expected value was around 0.7% with a maximum of 1.3% [16].

Thermal conductivity measurements were performed in the temperature range between 10°C and 70°C , with steps of 20°C , at ambient pressure. Figure 2 presents nanofluids thermal conductivity as a function of mass fraction and temperature, showing an almost linear enhancement with temperature at all the concentrations examined up to 50°C . Some instability is observed at temperature of 70°C , probably due to the introduction of convective motions or aggregation of the nanoparticles, but these phenomena cannot be evaluated during the conductivity tests. Table 1 presents the experimental data and the ratio between the thermal conductivity of the nanofluids and water at the same temperature.

3.2. Dynamic Viscosity. To evaluate the rheometer performance, preliminary tests were performed on a well-known fluid as water. The viscosity data were compared with Refprop 8.0 at each temperature, as shown in Figure 3. All the deviations between the measured and literature data are well within the experimental uncertainty for the shear rates between 200 and 1200 s^{-1} , with a maximum percentage absolute average deviation (AAD%) about 2.4%. The deviations at the lowest shear rate could be due to difficulties in the torque control by the rheometer.

Dynamic viscosity measurements were performed at 5 wt%, 10 wt%, and 20 wt% in the temperature range between 10°C and 70°C , with steps of 20°C .

Figure 4 shows the flow curves at 10°C for water and all nanofluids. The same trend was found at all the measured

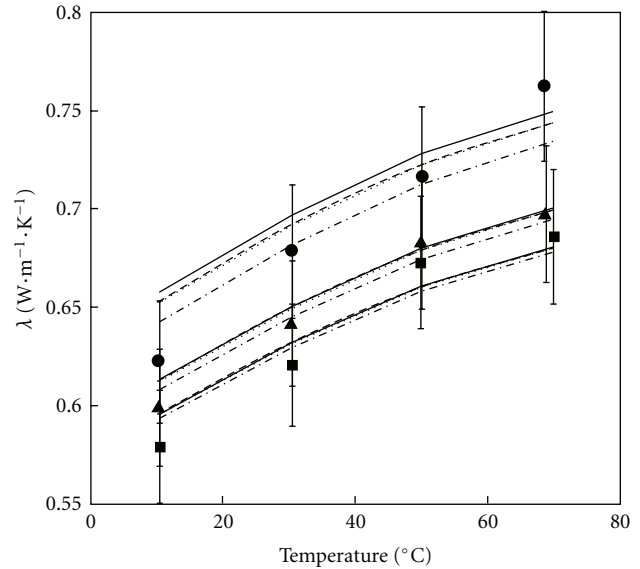


FIGURE 2: Experimental thermal conductivity of water- Fe_2O_3 nanofluid, (■) 5 wt%, (▲) 10 wt%, (●) 20 wt%, as a function of temperature. Comparison with Maxwell model (---), Bruggeman model (—), Lu and Lin model (- · -), Xuan model (—). Error bars correspond to 5% uncertainty.

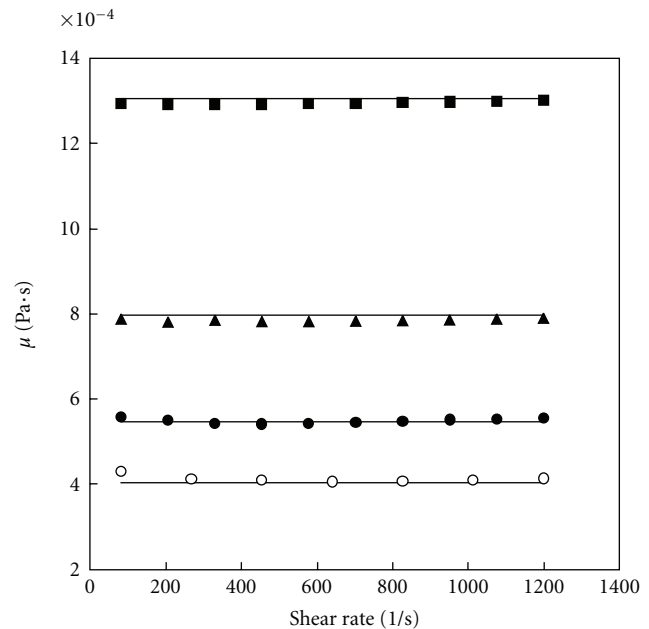
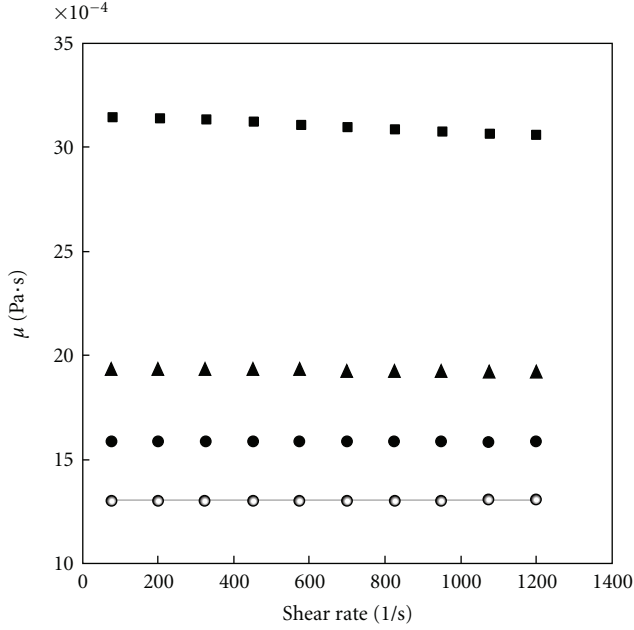


FIGURE 3: Dynamic viscosity of water at (■) 10°C , (▲) 30°C , (●) 50°C , (○) 70°C , compared to (—) Refprop 8.0.

temperatures. In Table 2, the experimental data are reported at shear rate around 800 s^{-1} . Under the imposed conditions and taking into account that the used rheometer could not operate at lower shear rates for some of these samples, the nanofluids appeared to have a Newtonian behaviour, as it can be deduced by Figure 5, where shear stress is represented as a function of shear rate for the measurements at 30°C .

TABLE 1: Experimental thermal conductivity data and thermal conductivity ratio for Fe₂O₃ water-based nanofluids.

Mass fraction	5 wt%		10 wt%		20 wt%	
Vol. fraction	0.99 vol%		2.08 vol%		4.55 vol%	
T (°C)	λ_{exp} (W·m ⁻¹ ·K ⁻¹)	$\lambda_{\text{exp}}/\lambda_{\text{water}}$	λ_{exp} (W·m ⁻¹ ·K ⁻¹)	$\lambda_{\text{exp}}/\lambda_{\text{water}}$	λ_{exp} (W·m ⁻¹ ·K ⁻¹)	$\lambda_{\text{exp}}/\lambda_{\text{water}}$
10.4	0.5791	1.00	0.5989	1.03	0.6223	1.07
30.4	0.6208	1.01	0.6418	1.04	0.6784	1.10
50.0	0.6728	1.05	0.6835	1.06	0.7161	1.11
70.0	0.6862	1.03	0.6974	1.05	0.7625	1.15

FIGURE 4: Dynamic viscosity of Fe₂O₃ at 10°C. (○) water, (●) 5 wt%, (▲) 10 wt%, (■) 20 wt% compared to (—) Refprop 8.0.

All isotherms are linear and converge to the origin of the diagram.

Figure 6 shows the trend of viscosity as a function of nanoparticles concentration at all temperatures. Viscosity improves in an exponential way at each temperature, reaching a maximum value of 0.00309 Pa·s at 20 wt% and 10°C. Viscosity decreases if temperature increases, with the same trend for all the concentrations.

3.3. Comparison with Published Literature. The only study presented in literature on dynamic viscosity of hematite dispersed in water is [17], in which Phuoc and Massoudi observed the rheological properties of Fe₂O₃ water-based nanofluids in concentrations between 1 and 4% in mass. They found a non-Newtonian behaviour, but their results cannot be compared with ours because their concentrations are lower and they always used polymer dispersants which strongly affect rheological behaviour. No other study on thermal conductivity of Fe₂O₃ water-based nanofluids has been found.

3.4. Theoretical Models

3.4.1. Thermal Conductivity. In Figure 2, our results are compared with classical effective thermal conductivity model, known as Maxwell (1873) model [18]:

$$k_{nf} = k_w \frac{k_p + 2k_w + 2\phi(k_w - k_p)}{k_p + 2k_w + \phi(k_w - k_p)}, \quad (1)$$

where k_w and k_p represent the thermal conductivity of water (the bulk liquid) and the added solid particles (15.42 W·m⁻¹·K⁻¹ [19]), respectively, and ϕ is the particle volume fraction of the suspension (vol%).

At the lower temperature, the model overestimates the experimental results, but, starting from temperatures around 50°C, theoretical and experimental results are in quite good agreement.

In literature, several models have been proposed. Amongst these, few models have been chosen for comparison.

Bruggeman model [20] is based on the differential effective medium theory in order to estimate the effective thermal conductivity of composites at high particle concentrations:

$$k_{nf} = k_w \frac{(3\phi - 1)k_p/k_w + [3(1 - \phi) - 1] + \sqrt{\Delta}}{4}, \quad (2)$$

$$\Delta = \left\{ (3\phi - 1) \frac{k_p}{k_w} + [3(1 - \phi) - 1] \right\}^2 + 8 \frac{k_p}{k_w}. \quad (3)$$

Lu and Lin model [21] is used for spherical and non-spherical particles. The effective conductivity of composites containing aligned spheroids of finite conductivity was modelled with the pair interaction:

$$k_{nf} = k_w(1 + a\phi + b\phi^2). \quad (4)$$

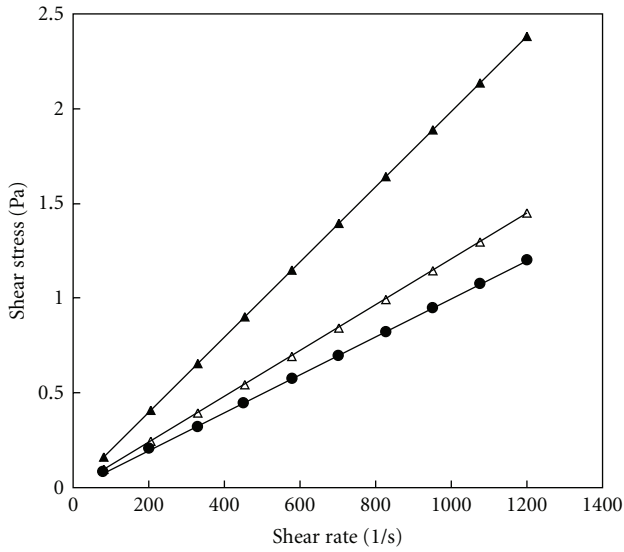
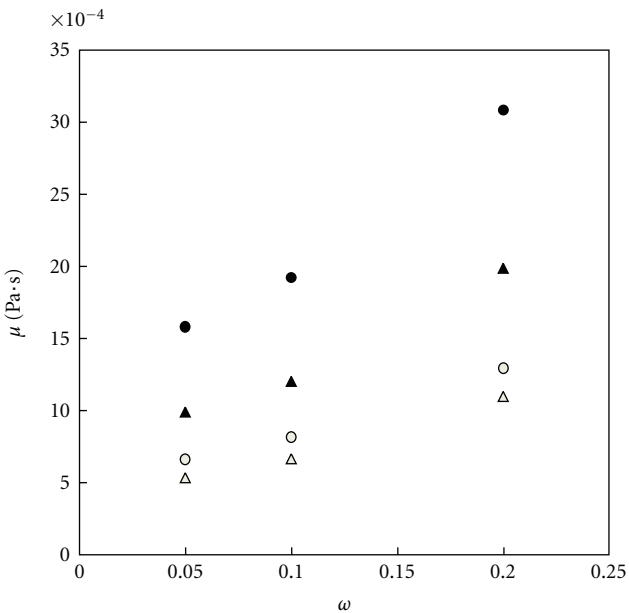
In the case of spherical particles, the values of the coefficients a and b are 2.25 and 2.27, respectively.

Xuan et al. model [22] is based on the Maxwell model and includes the effects of random motion, particle size, concentration, and temperature:

$$k_{nf} = k_w \left[\frac{k_p + 2k_w + 2\phi(k_w - k_p)}{k_p + 2k_w + \phi(k_w - k_p)} + \frac{\rho_p \cdot \phi \cdot c_{p,p}}{2k_w} \sqrt{\frac{k_B \cdot T}{3 \cdot \pi \cdot \mu \cdot r_c}} \right], \quad (5)$$

TABLE 2: Experimental viscosity data at constant shear rate (about 800 s^{-1}) and viscosity ratio for Fe_2O_3 water-based nanofluids.

Mass fraction	5 wt%		10 wt%		20 wt%	
Vol. fraction	0.99 vol%		2.08 vol%		4.55 vol%	
T ($^{\circ}\text{C}$)	μ_{exp} ($\text{Pa}\cdot\text{s}$)	$\mu_{\text{exp}}/\mu_{\text{water}}$	μ_{exp} ($\text{Pa}\cdot\text{s}$)	$\mu_{\text{exp}}/\mu_{\text{water}}$	μ_{exp} ($\text{Pa}\cdot\text{s}$)	$\mu_{\text{exp}}/\mu_{\text{water}}$
10.0	0.00158	1.21	0.00192	1.47	0.00309	2.36
30.0	0.00099	1.24	0.00120	1.51	0.00199	2.49
50.0	0.00066	1.21	0.00081	1.49	0.00129	2.36
70.0	0.00053	1.32	0.00067	1.65	0.00110	2.72

FIGURE 5: Shear stress as a function of shear rate for water- Fe_2O_3 nanofluid at 30°C . (\bullet) 5 wt%, (Δ) 10 wt%, (\blacktriangle) 20 wt%.FIGURE 6: Dynamic viscosity on mass fraction of water- Fe_2O_3 nanofluid at (\bullet) 10°C , (\blacktriangle) 30°C , (\circ) 50°C , (Δ) 70°C .

where T is the temperature, ρ_p is the density of particles, $c_{p,p}$ represents the specific heat capacity of particles, k_B is the Boltzmann constant, r_c is the radius of the clusters, and μ is the viscosity.

All these models were added to Figure 2, together with the experimental uncertainties. Their behaviour is very similar. They overestimate thermal conductivity values at temperature lower than 50°C , while they underestimate at higher temperature for all the nanofluids, although the data are always within the experimental uncertainties.

3.4.2. Dynamic Viscosity. In literature, several theoretical models have been proposed to predict the viscosity of a particle suspension. The most often used models derive from the Einstein model [23].

Brinkman extended the Einstein model to include particle volume concentration up to roughly 4% [24], in the form of

$$\mu_{nf} = \mu_f \frac{1}{(1 - \phi)^{2.5}}. \quad (6)$$

Here, ϕ is the particle volume fraction and μ_{nf} and μ_f are the dynamic viscosity of the nanofluid and the based fluid, respectively.

In [25], Batchelor proposed a similar correlation considering the nanoparticle Brownian motion and their interaction:

$$\mu_{nf} = \mu_f (1 + 2.5\phi + 6.5\phi^2). \quad (7)$$

In all these models a nanofluid is considered as a two-phase fluid and treated as a solid-liquid mixture. These equations base on the assumptions that the viscosity of the nanofluid is only a function of the base fluid viscosity and the particle concentration and that the nanoparticles can be modelled as rigid spherical particles. This assumption seems not correct for the systems nanofluids, which present specific properties and interactions not yet completely understood.

The effects of volume fraction ϕ and maximum volume fraction ϕ_m on viscosity are described using the Krieger-Dougherty equation [26]:

$$\mu_{nf} = \mu_f \left(1 - \frac{\phi_a}{\phi_m}\right)^{-[\eta]\phi_m}, \quad (8)$$

where ϕ_a is the effective aggregates volume fraction (and here it is considered as ϕ) and $[\eta]$ is the intrinsic viscosity (for noninteracting, rigid spherical particles, 2.5).

A simplified equation was proposed [26] as

$$\mu_{nf} = \mu_f \left(1 - \frac{\phi}{\phi_m}\right)^{-2}. \quad (9)$$

In order to apply (8) and (9), ϕ_m should be calculated. Basing on [27], the maximum solid concentration can be estimated by

$$\phi_m = \frac{1 - \beta}{\alpha}, \quad (10)$$

where α and β are calculated by the following equation [28]:

$$\mu_{nf} = \mu_f (1 - \alpha\phi - \beta)^{-2}. \quad (11)$$

Basing on the experimental data $\alpha = 0.07298$ and $\beta = 0.03402$, then ϕ_m becomes 13.24.

A comparison between experimental data and equations is shown in Figure 8. Equations (6) and (7) overlap equation (8).

All these equations underestimated nanofluids viscosity, confirming their incapability to model this property for nanofluids.

Here, a simple equation, with similar form to (4), is proposed to correlate the experimental data:

$$\mu_{nf} = \mu_f (1 + a\phi + b\phi^2). \quad (12)$$

This equation was regressed basing on all experimental data for nanofluids and water viscosity calculated by [15] at the same temperatures. The regressed parameters are $a = 18.64$ and $b = 248.30$. As shown in Figure 7, this equation well represents the experimental data.

3.5. Mouromtseff Number Analysis. Thermal conductivity and dynamic viscosity experimental data were also used to evaluate the nanofluid thermal effectiveness, by means of the *Mouromtseff number* (Mo). It is a figure of merit to evaluate and compare the heat transfer capability of alternative thermal fluids [29]. Higher Mo numbers indicate higher heat transfer capability of the fluid, for a given geometry at a specified velocity.

In case of full developed internal laminar flow, it can be shown that the ratio of Mo numbers for each nanofluid on that of water is equal to the ratio of the respective thermal conductivities:

$$\frac{Mo_{nf}}{Mo_{water}} = \frac{\lambda_{nf}}{\lambda_{water}}. \quad (13)$$

For internal turbulent flow, Mo number is given by

$$Mo = \frac{\rho^{0.8} \lambda^{0.67} c_p^{0.33}}{\mu^{0.47}}, \quad (14)$$

where ρ and c_p are density and specific heat of the fluid, respectively, and they were calculated as volume weighted averages ($\rho_{nf} = 5240 \text{ kg} \cdot \text{m}^{-3}$, $c_{pnf} = 628.0 \text{ J} \cdot \text{kg}^{-1} \cdot \text{K}^{-1}$) [30].

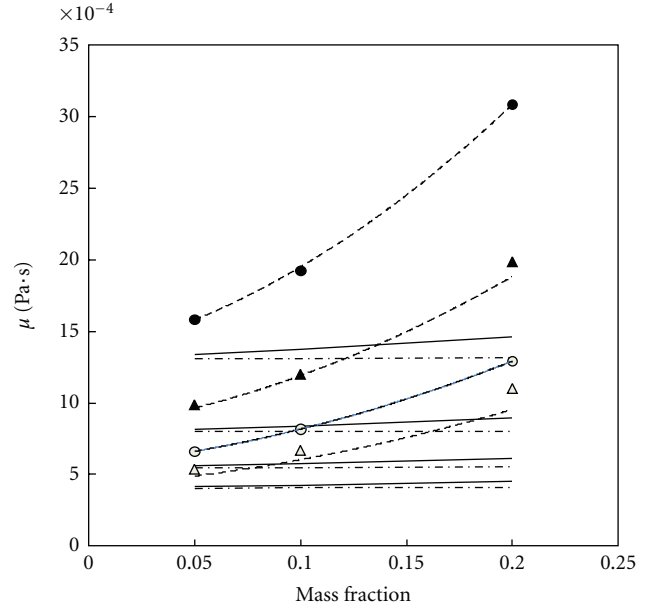


FIGURE 7: Experimental dynamic viscosity of water- Fe_2O_3 nanofluid at (●) 10°C, (▲) 30°C, (○) 50°C, (△) 70°C on mass fraction. Comparison with theoretical models: (—) equations (8); (---) equations (9); (-·-) equation (12). Equations (6) and (7) overlap equation (8).

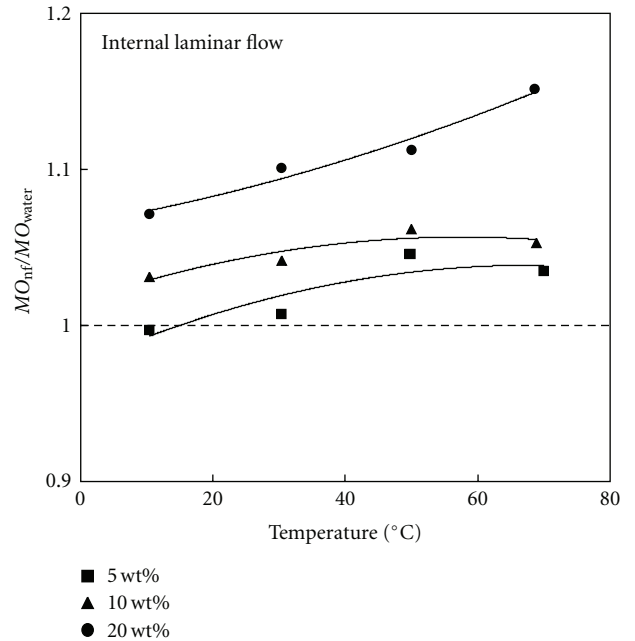


FIGURE 8: Mouromtseff number (Mo) for water- Fe_2O_3 in laminar flow.

Figures 8 and 9 show Mo number ratio as a function of temperature and concentration. For laminar flow, it is higher than 1, except for 5 wt% nanofluid at 10°C, and increases with nanoparticles concentration and temperature. Then, the heat transfer capability of water- Fe_2O_3 nanofluids is potentially higher than that of water if the flow is developed laminar.

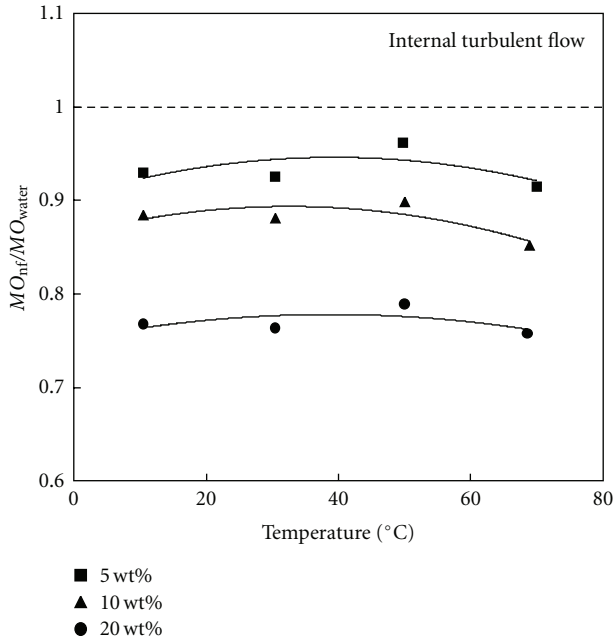


FIGURE 9: Mouromtseff number (Mo) for water- Fe_2O_3 in turbulent flow.

On the contrary, in turbulent flow (the most significant for technological applications) Mo ratio is always lower than 1, with a minimum of 0.76 for 20 wt% and 70°C. It means that heat transfer capability of water- Fe_2O_3 nanofluids is potentially lower than that of water, due to the increase of viscosity produced by the addition of nanoparticles.

4. Conclusions

Fe_2O_3 water-based nanofluids have long time stability also at high concentration as 20 wt%. Thermal conductivity increases with mass fraction and with temperature. Thermal conductivity ratio is greater at the highest concentrations. The rheological behaviour of the nanofluids is Newtonian, and the dynamic viscosity increases considerably in respect of water, mainly at mass fraction of 20 wt%. Hence, the increment in thermal conductivity is combined with a rising in dynamic viscosity. Mouromtseff number indicates that, if the water- Fe_2O_3 nanofluids work in laminar flow, their heat transfer capability is potentially higher than that of water, but if the flow is developed turbulent, there is a loss in the heat transfer capability, due to the increase in viscosity. In order to experimentally measure the heat transfer capability, a new apparatus, able to measure the heat transfer coefficient, is going to be installed in our Institute.

References

[1] R. Saidur, K. Y. Leong, and H. A. Mohammad, "A review on applications and challenges of nanofluids," *Renewable and Sustainable Energy Reviews*, vol. 15, no. 3, pp. 1646–1668, 2011.

[2] S. U. S. Choi, "Nanofluid technology: current status and future research," in *Proceedings of the Korea-U.S. Technical Conference on Strategic Technologies*, pp. 22–24, Vienna, Va, USA, 1998.

[3] M. J. Pastoriza-Gallego, C. Casanova, R. Páramo, B. Barbés, J. L. Legido, and M. M. Pieiro, "A study on stability and thermophysical properties (density and viscosity) of Al_2O_3 in water nanofluid," *Journal of Applied Physics*, vol. 106, no. 6, Article ID 064301, 2009.

[4] V. H. Grassian, "When size really matters: size-dependent properties and surface chemistry of metal and metal oxide nanoparticles in gas and liquid phase environments," *Journal of Physical Chemistry C*, vol. 112, no. 47, pp. 18303–18313, 2008.

[5] X. J. Wang, D. S. Zhu, and S. yang, "Investigation of pH and SDBS on enhancement of thermal conductivity in nanofluids," *Chemical Physics Letters*, vol. 470, no. 1–3, pp. 107–111, 2009.

[6] A. Ghadimi, R. Saidur, and H. S.C. Metselaar, "A review of nanofluid stability properties and characterization in stationary conditions," *International Journal of Heat and Mass Transfer*, vol. 54, no. 17-18, pp. 4051–4068, 2011.

[7] L. Fedele, L. Colla, S. Bobbo, S. Barison, and F. Agresti, "Experimental stability analysis of different water-based nanofluids," *Nanoscale Research Letters*, vol. 6, no. 1, pp. 1–8, 2011.

[8] Y. Hwang, J. K. Lee, J. K. Lee et al., "Production and dispersion stability of nanoparticles in nanofluids," *Powder Technology*, vol. 186, no. 2, pp. 145–153, 2008.

[9] P. Kebabian, R. Prasher, and J. Eapen, "Thermal conductance of nanofluids: is the controversy over?" *Journal of Nanoparticle Research*, vol. 10, no. 7, pp. 1089–1097, 2008.

[10] W. Yu, D. M. France, J. L. Routbort, and S. U. S. Choi, "Review and comparison of nanofluid thermal conductivity and heat transfer enhancements," *Heat Transfer Engineering*, vol. 29, no. 5, pp. 432–460, 2008.

[11] J. A. Eastman, S. U. S. Choi, S. Li, W. Yu, and L. J. Thompson, "Anomalously increased effective thermal conductivities of ethylene glycol-based nanofluids containing copper nanoparticles," *Applied Physics Letters*, vol. 78, no. 6, pp. 718–720, 2001.

[12] S. U. S. Choi, *Nanofluid Technology: Current Status and Future Research*, Energy Technology Division, Argonne National Laboratory, Argonne, France, 1999.

[13] Y. He, "Rapid thermal conductivity measurement with a hot disk sensor—part 1. Theoretical considerations," *Thermochimica Acta*, vol. 436, no. 1-2, pp. 122–129, 2005.

[14] S. Bobbo, L. Fedele, A. Benetti et al., "Viscosity of water based SWCNH and TiO_2 nanofluids," *Experimental Thermal and Fluid Science*, vol. 36, pp. 65–71, 2012.

[15] E. W. Lemmon, M. L. Huber, and M. O. McLinden, "NIST Reference Fluid Thermodynamic and Transport Properties-REFPROP," Version 8.0, Physical and Chemical Properties Division, National Institute of Standards and Technology, Boulder, Colo, USA, 2007.

[16] S. Bobbo, L. Colla, M. Scattolini et al., "Thermal conductivity and viscosity measurements of water-based silica nanofluids," in *Proceedings of the Nanotech Conference and Expo*, Boston, Mass, USA, June 2011.

[17] T. X. Phuoc and M. Massoudi, "Experimental observations of the effects of shear rates and particle concentration on the viscosity of Fe_2O_3 -deionized water nanofluids," *International Journal of Thermal Sciences*, vol. 48, no. 7, pp. 1294–1301, 2009.

[18] J. C. Maxwell, *A Treatise on Electricity and Magnetism*, vol. 2, Clarendon Press, Oxford, UK, 1873.

- [19] C. Clauser and E. Huenges, *Rock Physics and Phase Relations. A Handbook of Physical Constants*, American Geophysical Union, Washington, DC, USA, 1995, Edited by T. J. Ahrens.
- [20] D. A. G. Bruggeman, "Berechnung berechnung verschiedener physikalischer konstanten von heterogenen substanzen. I. Dielektrizitätskonstanten und leitfähigkeiten der mischkörper aus isotropen substanzen," *Annalen der Physik*, vol. 416, no. 7, pp. 636–664, 1935.
- [21] S. Y. Lu and H. C. Lin, "Effective conductivity of composites containing aligned spheroidal inclusions of finite conductivity," *Journal of Applied Physics*, vol. 79, no. 9, pp. 6761–6769, 1996.
- [22] Y. Xuan, Q. Li, and W. Hu, "Aggregation structure and thermal conductivity of nanofluids," *AIChE Journal*, vol. 49, no. 4, pp. 1038–1043, 2003.
- [23] A. Einstein, "Eine neue Bestimmung der Molekiildimensionen," *Annalen der Physik*, vol. 19, pp. 289–306, 1906.
- [24] H. C. Brinkman, "The viscosity of concentrated suspensions and solutions," *The Journal of Chemical Physics*, vol. 20, no. 4, pp. 571–581, 1952.
- [25] G. K. Batchelor, "The effect of Brownian motion on the bulk stress in a suspension of spherical particles," *Journal of Fluid Mechanics*, vol. 83, no. 1, pp. 97–117, 1977.
- [26] I. M. Krieger and T.-J. Dougherty, "A mechanism for non-Newtonian flow in suspensions of rigid spheres," *Transactions of the Society of Rheology*, vol. 3, pp. 137–152, 1959.
- [27] T. Kitano, T. Kataoka, and T. Shirota, "An empirical equation of the relative viscosity of polymer melts filled with various inorganic fillers," *Rheologica Acta*, vol. 20, no. 2, pp. 207–209, 1981.
- [28] D. M. Liu, "Particle packing and rheological property of highly-concentrated ceramic suspensions: ϕ_m determination and viscosity prediction," *Journal of Materials Science*, vol. 35, no. 21, pp. 5503–5507, 2000.
- [29] R. E. Simons, "Comparing heat transfer rates of liquid coolants using the Mouromtseff number," *Electronics Cooling*, vol. 12, 2006.
- [30] E. V. Timofeeva, W. Yu, D. M. France, D. Singh, and J. L. Routbort, "Nanofluids for heat transfer: an engineering approach," *Nanoscale Research Letters*, vol. 6, p. 182, 2011.

Research Article

Numerical Study of Laminar Confined Impinging Slot Jets with Nanofluids

Giuseppe Di Lorenzo, Oronzio Manca, Sergio Nardini, and Daniele Ricci

Dipartimento di Ingegneria Aerospaziale e Meccanica, Seconda Università degli Studi di Napoli, Real Casa dell'Annunziata, Via Roma, 29-81031 Aversa, Italy

Correspondence should be addressed to Oronzio Manca, oronzio.manca@unina2.it

Received 4 July 2011; Accepted 2 September 2011

Academic Editor: Liqiu Wang

Copyright © 2012 Giuseppe Di Lorenzo et al. This is an open access article distributed under the Creative Commons Attribution License, which permits unrestricted use, distribution, and reproduction in any medium, provided the original work is properly cited.

A solution to obtain efficient cooling systems is represented by the use of confined or unconfined impinging jets. Moreover, the possibility of improving the thermal performances of the working fluids can be taken into account and the introduction of nanoparticles in a base fluid can be considered. In this paper, a numerical investigation on confined impinging slot jet working with a mixture of water and Al_2O_3 nanoparticles is described. The flow is laminar and a uniform temperature is applied on the target surface. The single-phase model approach has been adopted. Different geometric ratios, particle volume concentrations, and Reynolds numbers have been considered in order to study the behaviour of the system in terms of average and local Nusselt number, convective heat transfer coefficient and required pumping power profiles, temperature fields, and stream function contours.

1. Introduction

Heat transfer enhancement is a significant issue in the research and industry fields. Both active and passive techniques can be employed. The impinging jets are classified into the category of the active methods, and they have been widely used in several industrial applications as a means of providing high localized heat transfer coefficients. In fact, impinging jets are applied to drying of textiles, film, and paper, cooling of gas turbine components and the outer wall of combustors, freezing of tissue in cryosurgery and manufacturing, material processing, and electronic cooling. There are numerous papers concerning this problem, and the analyses have been performed both numerically and experimentally [1–6].

Several studies have been developed on impinging air jets [1, 2] but liquid jets have been recently studied because they have possible application to the cooling of heat engines [5, 7], thermal control in electronic devices [8, 9], and the thermal treatment of metals and material processing [10–12].

The main configurations include circular or slot jets, and their flow and heat transfer mechanics are significantly different. It seems that more research activity on heat and

mass transfer with circular impinging jets has been predominantly published [1–3, 13, 14]. However, investigations on heat and mass transfer with slot jet impingement have attracted more attention recently. In fact, slot jet impingements offer some benefits in cooling effectiveness, uniformity, and controllability, as underlined in [15]. These features are suitable with ones required by the modern electronic packages, characterized by increasing heat flux and decreasing dimensions [15–21]. Impinging jets can be confined or unconfined. Small space designs mark the confined configurations while unconfined impinging jets provide advantages in terms of simple design and easy fabrication. These types of impinging jets are both commonly used, and literature reviews on the subject have been provided in [2, 3, 6]. The effects of confinement on impinging jet heat transfer have been considered in [22–25]. The importance of the subject is underlined by the several investigations performed on impingement on moving plates [25], obliquely flat surfaces [26], porous mediums [27], semicircular concave surfaces [28], jet arrays [29], and adopting foams or fins [30]. Moreover, laminar [20, 31] and turbulent [23, 32, 33] flow regimes can be considered.

Another way can be adopted in order to enhance heat transfer rates without modifications in the cooling system, such as the employment of nanosize particles dispersed in the working fluids [34]. The investigation on nanofluid behaviour is becoming more and more popular, as testified by recent reviews and papers on this issue [35–44] but inconsistencies in published data and disagreements on the heat transfer mechanisms have been underlined by Koblinski et al. [45] and recently by Gherasim et al. [46]. However, a few examples of studies on nanofluids in impinging jets have been investigated experimentally and numerically and, according to the best knowledge of the present authors, their investigations have been reported in [46–59]. Roy et al. [50] provided the first numerical results on the hydrodynamic and thermal fields of $\text{Al}_2\text{O}_3/\text{water}$ nanofluid in a radial laminar flow cooling system, underlining a heat transfer enhancement up to 200% in the case of a nanofluid with 10% in nanoparticle volume concentration at a Reynolds number equal to 1200. However, a significant increase in wall shear stress was noticed. Also Palm et al. [51] numerically investigated laminar impinging jets but they considered temperature-dependent properties of fluids. Results indicated an increase of 25% in terms of average wall heat transfer coefficient, referred to the water at a concentration equal to 4%. Moreover, the use of temperature-dependent properties determined for greater heat transfer predictions with corresponding decreases in wall shear stresses when compared to evaluations employing constant properties. The significant heat removal capabilities of nanofluids were confirmed by the numerical study on steady, laminar radial flow of a nanofluid in a simplified axisymmetric configuration with axial coolant injection, performed by Roy et al. [52]. Roy et al. [50] numerically simulated the behaviour of various particle volume fractions in a circular confined and submerged jet impinging on a horizontal hot plate. Both laminar and turbulent impinging jets in various nozzle-to-plate distances and Reynolds numbers were considered. They underlined the higher heat removal performances of laminar jets in comparison with the base fluid. The investigation on steady laminar incompressible alumina/water flow between parallel disks was performed by Vaziei and Abouali [53] who evaluated increasing Nusselt number values with higher nanoparticle volume fraction, smaller nanoparticle diameter, reduced disk spacing, and larger jet Reynolds number. Gherasim et al. [46] highlighted the limitations in the use of $\text{Al}_2\text{O}_3/\text{water}$ nanofluid in a radial flow configuration due to the significant increase in the associated pumping power. Also, Yang and Lai presented numerical results on confined jets with constant [55] and temperature-dependent [56] properties. Results confirmed the Nusselt number increases with the increase of Reynolds number and nanoparticle volume fraction and the increase in pressure drop. Furthermore, temperature-dependent thermophysical properties of nanofluids were found to have a marked bearing on the simulation results. Manca et al. [57] numerically investigated the confining effects on impinging slot jets in the turbulent regime, such as for Reynolds numbers, ranging from 5000 to 20000. They adopted the single-phase approach in order to describe the $\text{Al}_2\text{O}_3/\text{water}$ nanofluid behaviour for particle

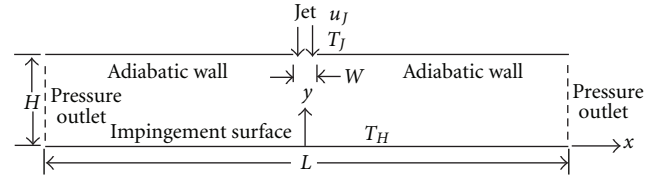


FIGURE 1: Sketch of the geometrical model with boundary conditions.

concentrations up to 5%. A significant enhancement in terms of convective heat transfer coefficients was evaluated for high particle volume concentrations as well as an increase of required pumping power.

On the experimental side, an interesting investigation was carried out by Nguyen et al. [58]. They paid attention to a confined and submerged impinging jet on a flat, horizontal, and circular heated surface with $\text{Al}_2\text{O}_3/\text{water}$ nanofluid. Results were obtained for both laminar and turbulent flow regimes, and the authors showed that, depending upon the combination of nozzle-to-heated surface distance and particle volume fraction, the use of a nanofluid can determine a heat transfer enhancement. Gherasim et al. [59] studied heat transfer enhancement capabilities of coolants with suspended nanoparticles inside a laminar radial flow cooling device. Mean Nusselt number was found to increase with particle volume fraction, Reynolds number, and a decrease in disk spacing.

It seems that a slot confined and submerged impinging jet on a flat surface with nanofluids has not been investigated in laminar flow regime in spite of its importance in engineering applications such as electronic cooling and material processing. In particular, localized and micro-sized cooling devices are significantly suitable for the thermal control requirements in electronic applications [46–59]. The present paper describes a numerical investigation on laminar flow on a confined and submerged impinging slot jet on an isothermal flat surface that is carried out by means of Fluent code [60]. The results are given to evaluate the fluid dynamic and thermal features of the considered geometry with water/ Al_2O_3 -based nanofluids as the working fluids. The single-phase model was adopted.

2. Governing Equations

A computational analysis of a two-dimensional confined impinging slot jet, depicted in Figure 1, is considered in order to evaluate its thermal and fluid-dynamic behaviours and study the temperature and velocity fields in the cases with $\text{Al}_2\text{O}_3/\text{water}$ nanofluid as working fluid. The jet width is W while the distance between the slot jet and the heated plate is H . A constant uniform temperature is applied on the target surface. The use of a two-dimensional slot jet is fair when the lateral length, in the orthogonal direction in respect to the jet, is significant. In particular, Zhou and Lee [61] suggested dimensionless lateral distances, referred to the nozzle width, greater than 6–7 in order to neglect the effect of lateral distance. Different jet velocities are considered

TABLE 1: Properties of pure water and Al₂O₃ particles at $T = 293$ K.

Material	ρ [kg/m ³]	c_p [J/kg K]	μ [Pa s]	λ [W/m K]
Al ₂ O ₃	3880	773	//	36
Water	998.2	4182	993×10^{-6}	0.597

in the ranges of laminar regime, and the fluid properties were considered constant with temperature. Governing equations of continuity, momentum, and energy are solved for a steady-state laminar flow in rectangular coordinates, under the hypotheses of two-dimensional, incompressible, temperature-constant properties flow conditions:

continuity:

$$\frac{\partial u}{\partial x} + \frac{\partial v}{\partial y} = 0, \quad (1)$$

momentum:

$$\begin{aligned} \left[u \frac{\partial u}{\partial x} + v \frac{\partial u}{\partial y} \right] &= -\frac{1}{\rho} \frac{\partial P}{\partial x} + \nu \left[\frac{\partial^2 u}{\partial x^2} + \frac{\partial^2 u}{\partial y^2} \right], \\ \left[u \frac{\partial v}{\partial x} + v \frac{\partial v}{\partial y} \right] &= -\frac{1}{\rho} \frac{\partial P}{\partial y} + \nu \left[\frac{\partial^2 v}{\partial x^2} + \frac{\partial^2 v}{\partial y^2} \right], \end{aligned} \quad (2)$$

energy:

$$\left[u \frac{\partial T}{\partial x} + v \frac{\partial T}{\partial y} \right] = \lambda \left[\frac{\partial^2 T}{\partial x^2} + \frac{\partial^2 T}{\partial y^2} \right]. \quad (3)$$

The assigned boundary conditions are the following:

- (i) jet section: uniform velocity and temperature profile;
- (ii) outlet sections: pressure outlet in order to define the static pressure at flow outlets;
- (iii) target surface: velocity components equal to zero and assigned temperature value;
- (iv) upper wall: velocity components and heat flux equal to zero.

3. Physical Properties of Nanofluids

The working fluid is water or a mixture of water and Al₂O₃ nanoparticles characterized by a diameter of 30 nm and volume fractions equal to 1%, 4%, and 5%. In Table 1 the values of density, specific heat, dynamic viscosity, and thermal conductivity, given by Rohsenow et al. [62], are reported for water and Al₂O₃. The presence of nanoparticles and their concentrations influence the working fluid properties. A single-phase model was adopted because nanofluids may be considered as Newtonian fluids for low volume fractions, such as up to 10%, and for small temperature increases. Thus, it is necessary to employ relations, available in literature, in order to compute the thermal and physical properties of the considered nanofluids [51, 63–66], given in Table 2. Density was evaluated by using the classical formula developed for conventional solid-liquid mixtures

while the specific heat values were obtained by assuming the thermal equilibrium between particles and surrounding fluid [46, 51, 63, 64]:

Density:

$$\rho_{nf} = (1 - \phi)\rho_{bf} + \phi\rho_p, \quad (4)$$

Specific heat:

$$(\rho c_p)_{nf} = (1 - \phi)(\rho c_p)_{bf} + \phi(\rho c_p)_p. \quad (5)$$

For the viscosity as well as for thermal conductivity, equations given by [65, 66] were adopted because these relations are expressed as a function of particle volume concentration and diameter:

Dynamic viscosity:

$$\mu_{nf} = \mu_{bf} + \frac{\rho_p V_B d_p^2}{72C\delta}, \quad (6)$$

Thermal conductivity:

$$\frac{\lambda_{nf}}{\lambda_{bf}} = 1 + 64.7\phi^{0.746} \left(\frac{d_{bf}}{d_p} \right)^{0.3690} \left(\frac{\lambda_p}{\lambda_{bf}} \right), \quad (7)$$

where $V_B = \sqrt{18K_b T / \pi \rho_p d_p}$ and K_b is the Boltzmann constant, given by $K_b = 1.36 \times 10^{-26}$; the other terms are given by the following relations:

$$C = \mu_{bf}^{-1} \left[(c_1 d_p + c_2)\phi + (c_3 d_p + c_4) \right] \quad (8)$$

with $c_1 = -0.000001133$, $c_2 = -0.000002771$, $c_3 = 0.00000009$, and $c_4 = -0.000000393$, and the distance between nanoparticles, δ , is obtained by

$$\delta = \sqrt[3]{\frac{\pi}{6\phi}} d_p. \quad (9)$$

4. Geometrical Configuration

A computational thermofluidynamic analysis of a two-dimensional model, reported in Figure 1, which concerns with a confined impinging jet on a heated wall with nanofluids, is considered in order to evaluate the thermal and fluid-dynamic performances and study the velocity and temperature fields. The two-dimensional model has the jet orifice width, W , equal to 6.2 mm and a length L/W equal to 50 while the height H/W ranges from 4 to 8. A constant temperature value of 313 K is applied on the impingement bottom surface. Two values of H/W ratio, equal to 4 and 8, are considered. The working fluid is pure water or a water/Al₂O₃-based nanofluid at different volume fractions.

TABLE 2: Thermophysical properties of the working fluids.

ϕ	ρ [kg/m ³]	c_p [J/kgK]	μ [Pa s]	λ [W/mK]
0%	998.2	4182	993×10^{-6}	0.597
1%	1027	4148	1110×10^{-6}	0.617
4%	1113	4046	1370×10^{-6}	0.654
5%	1142	4012	1724×10^{-6}	0.664

The dimensionless parameters of Reynolds number, Nusselt number, dimensionless temperature, and dimensionless pressure or pressure coefficient, here considered, are expressed by the following relations:

$$\text{Re} = \frac{u_j W}{\nu}, \quad (10)$$

$$\text{Nu} = \frac{\dot{q} W}{(T_H - T_j) \lambda_f}, \quad (11)$$

$$\theta = \frac{T - T_j}{(T_H - T_j)}, \quad (12)$$

$$C_P = \frac{P - P_j}{(1/2) \rho u_j^2}, \quad (13)$$

where u_j is the average jet velocity, W is the jet width, \dot{q} is the target surface heat flux, and T_H and T_j represent the temperature of the target surface and the jet temperature, respectively.

5. Numerical Procedure

The governing equations are solved by means of the finite volume method, adopting Fluent v6.3.26 code. A steady-state solution and a segregated method are chosen to solve the governing equations, which are linearized implicitly with respect to dependent variables of the equation. A second-order upwind scheme is chosen for energy and momentum equations. The SIMPLE coupling scheme is chosen to couple pressure and velocity. The convergence criteria of 10^{-5} and 10^{-8} are assumed for the residuals of the velocity components and energy, respectively. It is assumed that the incoming flow is laminar at ambient temperature equal to 293 K and pressure. Different inlet uniform velocities, u_j , corresponding to Reynolds number values ranging from 100 to 400, were considered. Along the solid walls no slip condition is employed whereas a velocity inlet and pressure outlet conditions are given for the inlet and outlet surfaces.

Four different grid distributions are tested, to ensure that the numerical results were grid independent for the case characterized by $H/W = 6$ with pure water as working fluid at $\text{Re} = 150$. They have 4950 (90×55), 19800 (180×110), 79200 (360×220), and 316800 (720×440) nodes, respectively. For the adiabatic wall and the bottom surface nodes are distributed by means of an exponential relation ($n = 0.9$), in order to have a fine mesh near the impingement region. On the vertical ones a biexponential distribution ($n = 0.8$) is considered. The third grid case has been

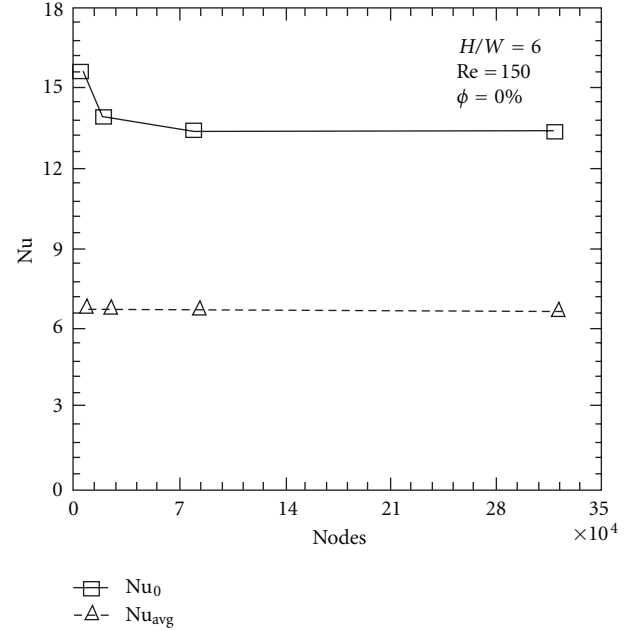


FIGURE 2: Grid independence test results in terms of average and stagnation point Nusselt number.

adopted because it ensured a good compromise between the machine computational time and the accuracy requirements. In fact, comparing the third and fourth mesh configurations in terms of average and stagnation point Nusselt number, results are very close and the relative errors are very small, as reported in Figure 2. Moreover, the computational time is quantified in about eight hours on average.

Results are validated by comparing the obtained numerical data with the ones given in [20, 66]. In particular, comparisons in terms of local and stagnation point Nusselt number values and pressure coefficients are reported in Figure 3 for the cases with $H/W = 4$ and Re , ranging from 50 to 400. It is observed that the present results fit very well with the ones given in [20] in terms of local Nusselt number and pressure coefficients for all the considered Reynolds numbers. Also, the stagnation point Nusselt number values are in good agreement with the correlation given by [67].

6. Results and Discussion

A computational analysis of a two-dimensional model, regarding a confined impinging jet on a heated wall with

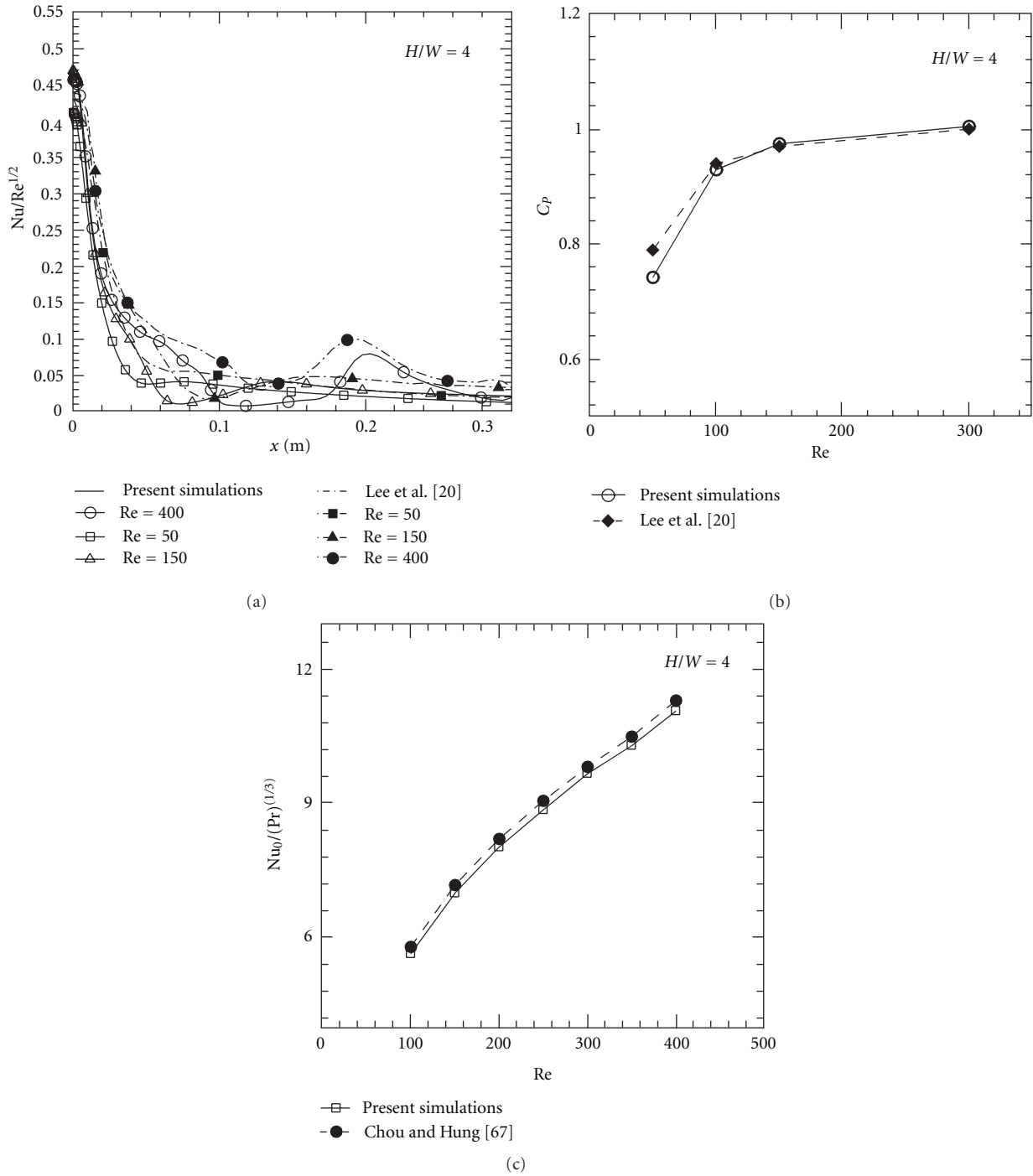


FIGURE 3: Validation of results, cases with $H/W = 4$: (a) local Nusselt number; (b) pressure coefficient; (c) stagnation point Nusselt number.

nanofluids, is considered in order to evaluate the thermal and fluid-dynamic performances and study the velocity and temperature fields. Different inlet velocities are considered in order to ensure a steady laminar regime, and the working fluids are water and mixtures of water and Al_2O_3 at different volume fractions. The single-phase model approach is adopted. The ranges of the considered Reynolds

numbers, geometric ratio, and volume fractions are given follows:

- (i) Reynolds number (Re): 100, 200, 300, and 400;
- (ii) H/W ratio: 4 and 8;
- (iii) particle concentrations (ϕ): 0%, 1%, 4%, and 5%.

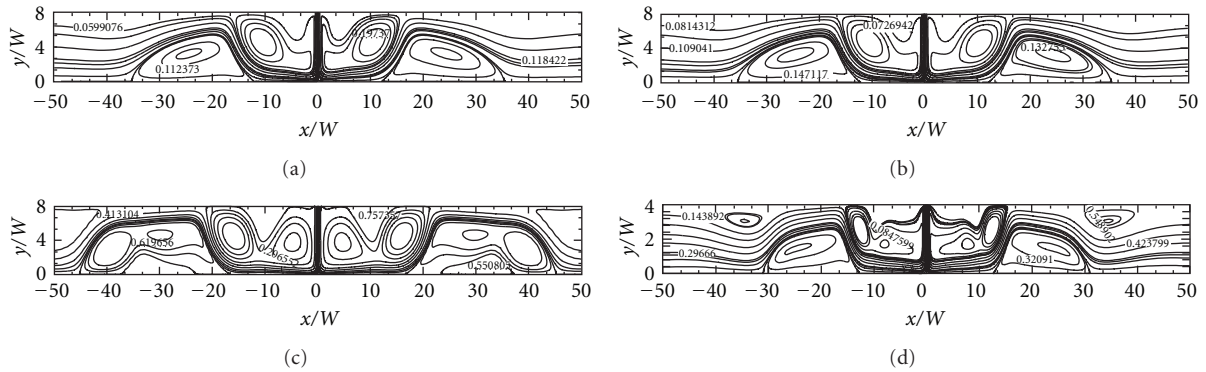


FIGURE 4: Stream function contours: (a) $H/W = 8$, $Re = 100$, and $\phi = 0\%$; (b) $H/W = 8$, $Re = 100$, and $\phi = 4\%$; (c) $H/W = 8$, $Re = 300$, and $\phi = 4\%$; (d) $H/W = 4$, $Re = 300$, and $\phi = 4\%$.

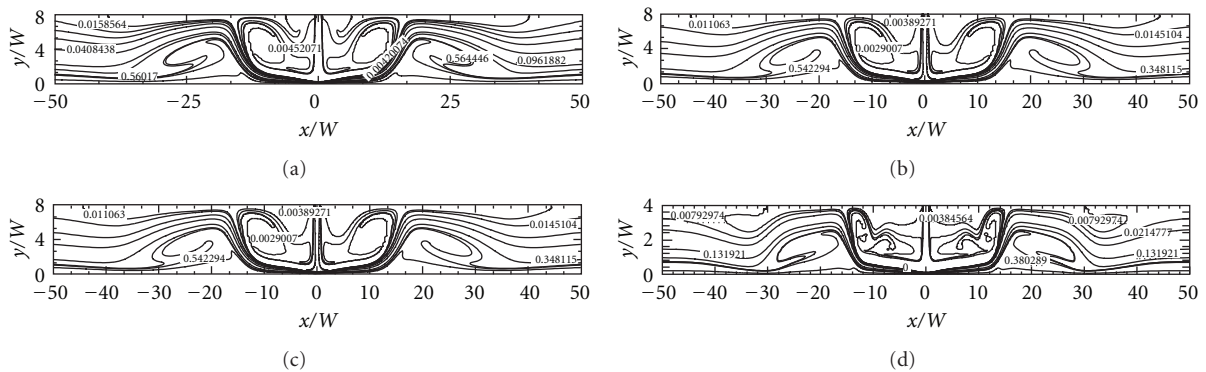


FIGURE 5: Dimensionless temperature fields: (a) $H/W = 8$, $Re = 100$, and $\phi = 0\%$; (b) $H/W = 8$, $Re = 100$, and $\phi = 4\%$; (c) $H/W = 8$, $Re = 300$, and $\phi = 4\%$; (d) $H/W = 4$, $Re = 300$, and $\phi = 4\%$.

Results are presented in terms of average and local convective heat transfer coefficients, Nusselt number, required pumping power profiles as a function of Reynolds number, H/W ratio, and particle concentrations; moreover, dimensionless temperature fields and stream function contours are reported.

Figures 4 and 5 depict the stream function contours and the dimensionless temperature fields, respectively, for the cases with two values of H/W ratio and Re , equal to 100 and 300, $\phi = 0\%$ and 4% . Figure 4 depicts two counterrotating vortex structures, generated when the fluid jet impinges on the target surface. The jet entrainment and confining effects of the upper adiabatic surfaces determine only one stagnation point. In this point the velocity gradients and temperature ones result in being very high. The confining effects, given by H/W ratio values, affect also the vortex intensity and size, together with the Reynolds number and particle concentrations. The comparison of Figure 4(a) with Figure 4(b) allows to analyze the behaviour of nanofluids in terms of motion field. These figures depict the cases with $H/W = 8$, $\phi = 0\%$ and 4% at $Re = 100$, respectively. Smoother eddies with a low intensity increase are observed because the nanofluid viscosity and density are higher than pure water. As Re increases, the separation area near the inlet section becomes larger and the fluid stream results in being

more compressed towards the target surface, as observed in Figure 4(c). Vortex intensity increases and the main eddies extinguish at x/W values larger than the ones evaluated for $Re = 100$, such as at $x/W = -45$ and 45 . However, as H/W decreases from 8 to 4, vortices result in being stronger near the symmetry axis of jet but they extinguish at x/W values equal to about -31 and 31 , as described in Figure 4(d).

The dimensionless temperature fields are presented in Figure 5 for the same configurations analyzed in Figure 4. They follow the stream line contours. In fact, the fluid temperature is very high near the stagnation point, where the highest values of heat transfer efficiency are detected then it decreases for increasing values of x/W . Nanofluids produce an increase of fluid bulk temperature because of the improved thermal conductivity of working fluids. For larger Reynolds numbers the efficiency of heat transfer increases while the confinement leads to higher temperatures in the separation zone and lower for increasing values of x/W values.

Figures 6 and 7 describe the convective heat transfer coefficient distributions along the target surface at $Re = 100$, 200, 300 and 400, for $\phi = 0\%$, 1%, 4%, and 5%, for $H/W = 4$ and 8, respectively. The local convective heat transfer coefficient is defined by $h_x = \dot{q}_x / (T_H - T_j)$. It is shown that the highest values, detected in correspondence with the

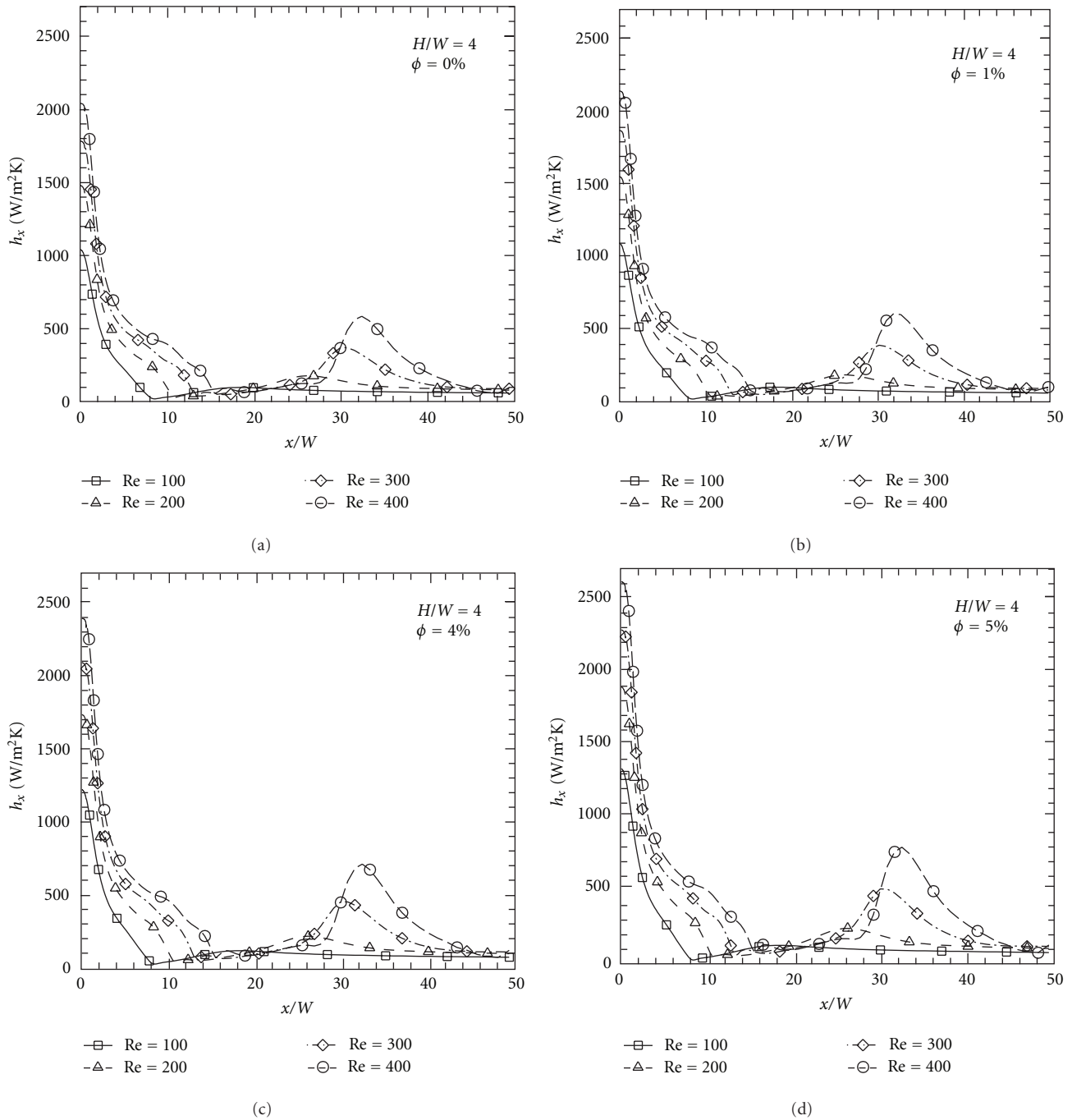


FIGURE 6: Local convective heat transfer coefficient profiles along x/W , $H/W = 4$, and $Re = 100, 200, 300$, and 400 : (a) $\phi = 0\%$; (b) $\phi = 1\%$; (c) $\phi = 4\%$; (d) $\phi = 5\%$.

stagnation point, increase as Reynolds number values and volume concentrations increase. An average increase of about 27% is evaluated. The heat transfer coefficient profiles have a minimum value, depending on Re , at $x/W = 9, 10, 14$ and 19 for $Re = 100, 200, 300$, and 400 , respectively, and very small differences are detected in terms of position for increasing particle volume fractions. Another relative maximum is reported at about $x/W = 32$, and its value increases as Re and ϕ grow. In fact, it is equal to 180 and $580 \text{ W/m}^2\text{K}$ for $\phi = 0\%$

and 210 and $800 \text{ W/m}^2\text{K}$ for $\phi = 5\%$ at $Re = 200$ and 400 . The increase in terms of H/W ratio leads to a small decrease of the highest heat transfer coefficients for $Re < 300$, as pointed out in Figure 7. Moreover, the minimum values are evaluated at larger x/W values and also the second relative maxima are detected towards the outlet section.

The variation of local Nusselt number along the target plate for different values of Re , $H/W = 4$ and 8 , $\phi = 0\%$, and 5% is shown in Figure 8. It is observed that highest values

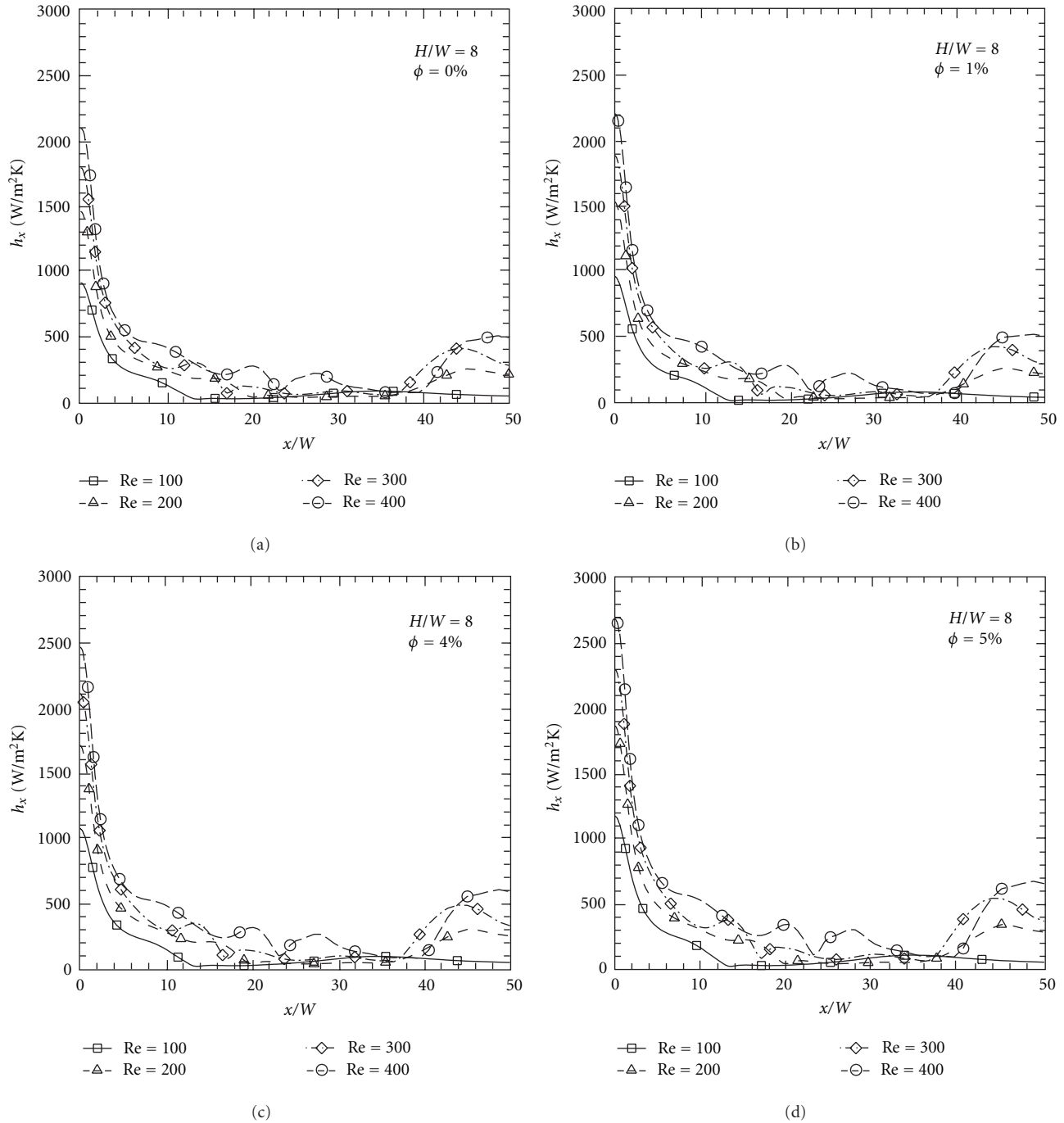


FIGURE 7: Local convective heat transfer coefficient profiles along x/W , $H/W = 8$, and $Re = 100, 200, 300$ and 400 : (a) $\phi = 0\%$; (b) $\phi = 1\%$; (c) $\phi = 4\%$; (d) $\phi = 5\%$.

of Nu_x are observed at the stagnation point for all considered cases. At $\phi = 0\%$ its value is 10.8, 15.2, 18.5, and 21.1 for $H/W = 4$ and 9.4, 14.9, 18.5 and 21.6 at $H/W = 8$, respectively, for $Re = 100, 200, 300$, and 400 , as depicted in Figures 8(a) and 8(c). At the end of the impingement plate, only for $H/W = 4$, Nu_x reaches for similar values equal to about 1. In Figures 8(b) and 8(c), the influence of nanoparticle concentration on the heat transfer is clear, enhanced by the

thermal conductivity improvement. In fact, if Figure 8(c) is analyzed, the highest Nusselt number at $\phi = 5\%$ is about 15% higher than the pure water jet values. For example, the highest values are equal to about 12.5 and 24.2 for $Re = 100$ and 400 in the case of $H/W = 4$ and 11.1 and 25.0 in the case of $H/W = 8$.

The stagnation point values in terms of convective heat transfer coefficients and Nusselt number are depicted in

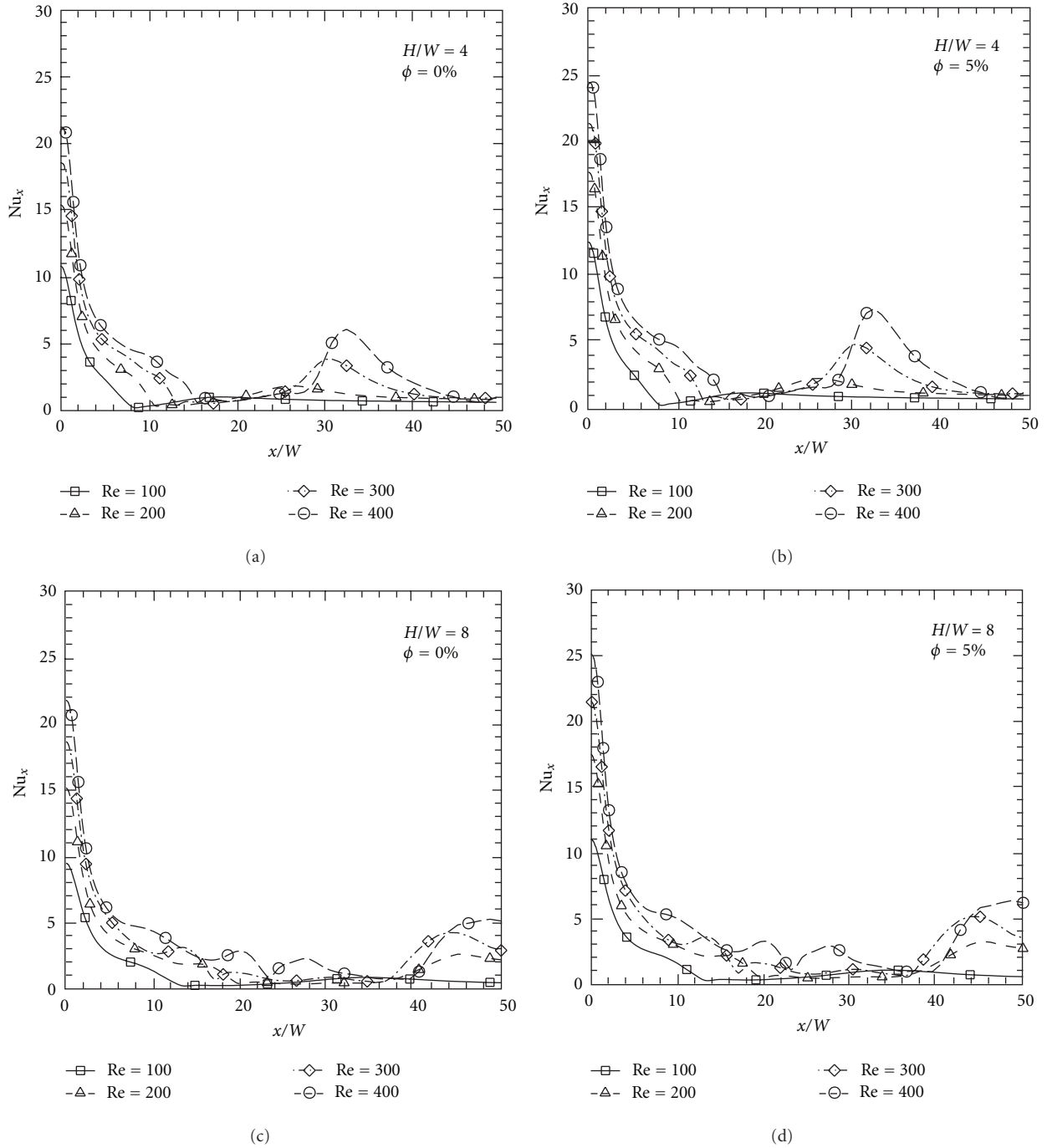


FIGURE 8: Local Nusselt number profiles along x/W , $Re = 100, 200, 300$ and 400 : (a) $H/W = 4, \phi = 0\%$; (b) $H/W = 4, \phi = 5\%$; (c) $H/W = 8, \phi = 0\%$; (d) $H/W = 8, \phi = 5\%$.

Figure 9 as a function of Reynolds number for $H/W = 4$ and 8 , and $\phi = 0\%, 1\%, 4\%$ and 5% . If Figure 9(a) is observed, h_0 is equal to about $1020, 1450, 1800$, and $2020 \text{ W/m}^2\text{K}$ at $\phi = 0\%$ and $1315, 1850, 2280$, and $2600 \text{ W/m}^2\text{K}$ at $\phi = 5\%$, respectively, for $H/W = 4$ and $Re = 100, 200, 300$, and 400 . The consequent Nu_0 values at $H/W = 4$ are equal to $10.8, 15.2, 18.1$, and 21.2 and $12.5, 17.8, 21.8$ and 24.7 , for $\phi = 0\%$ and 5% , respectively, as pointed out in Figure 9(c).

For $H/W = 8$, the stagnation point heat transfer coefficients and Nusselt number values are slightly lower than the ones calculated in the cases with $H/W = 4$ except for Reynolds numbers equal to 300 and 400 , as described in Figure 9(b) and 9(d).

The average values of convective heat transfer coefficient and Nusselt number increase as H/W ratio increases as shown in Figure 10, which reports the profiles as a function

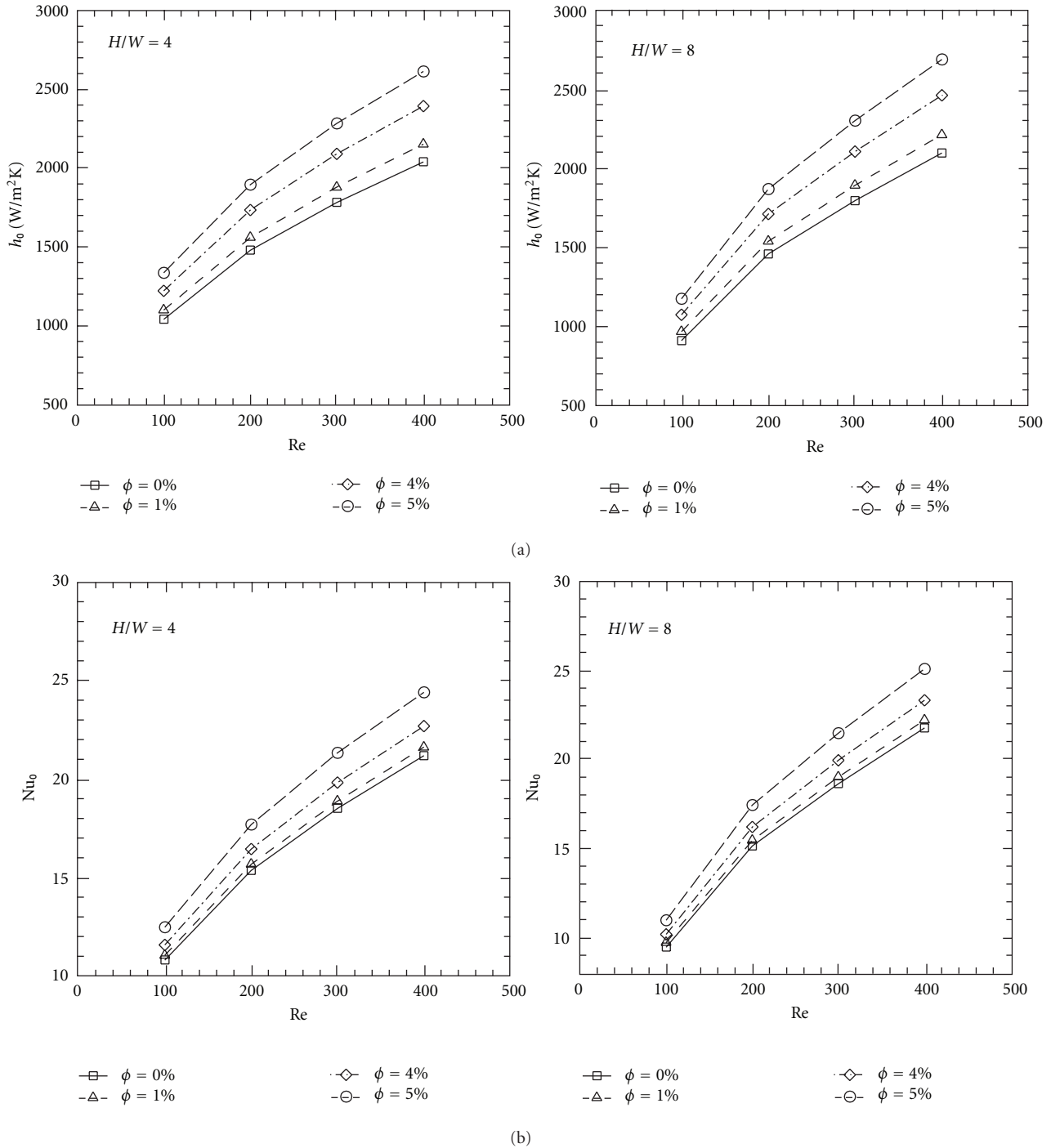


FIGURE 9: Profiles of stagnation point convective heat transfer coefficients and Nusselt number, as a function of Re for different concentrations: (a) convective heat transfer coefficients, $H/W = 4$ and 8; (b) Nusselt number, $H/W = 4$ and 8.

of Reynolds number at different values of particle volume fractions. Profiles increase linearly as Re increases and higher values are detected for larger nanoparticle volume fractions. For example, for $H/W = 4$ h_{avg} is equal to about 120 and 330 W/m²K for $\phi = 0\%$ while it is 155 and 435 W/m²K for $\phi = 5\%$, respectively, at Re = 100 and 400, as reported in Figure 10(a). Thus, an average increase of 8%, 17% and 32%

is calculated in comparison with pure water heat transfer coefficients for $\phi = 1\%$, 4%, and 5%, respectively. The average Nusselt number improvement results in being less remarkable, as observed in Figure 10(b). In fact, at $H/W = 8$, an enhancement of 3%, 10%, and 19% in terms of average Nusselt number is evaluated in comparison with pure water cases.

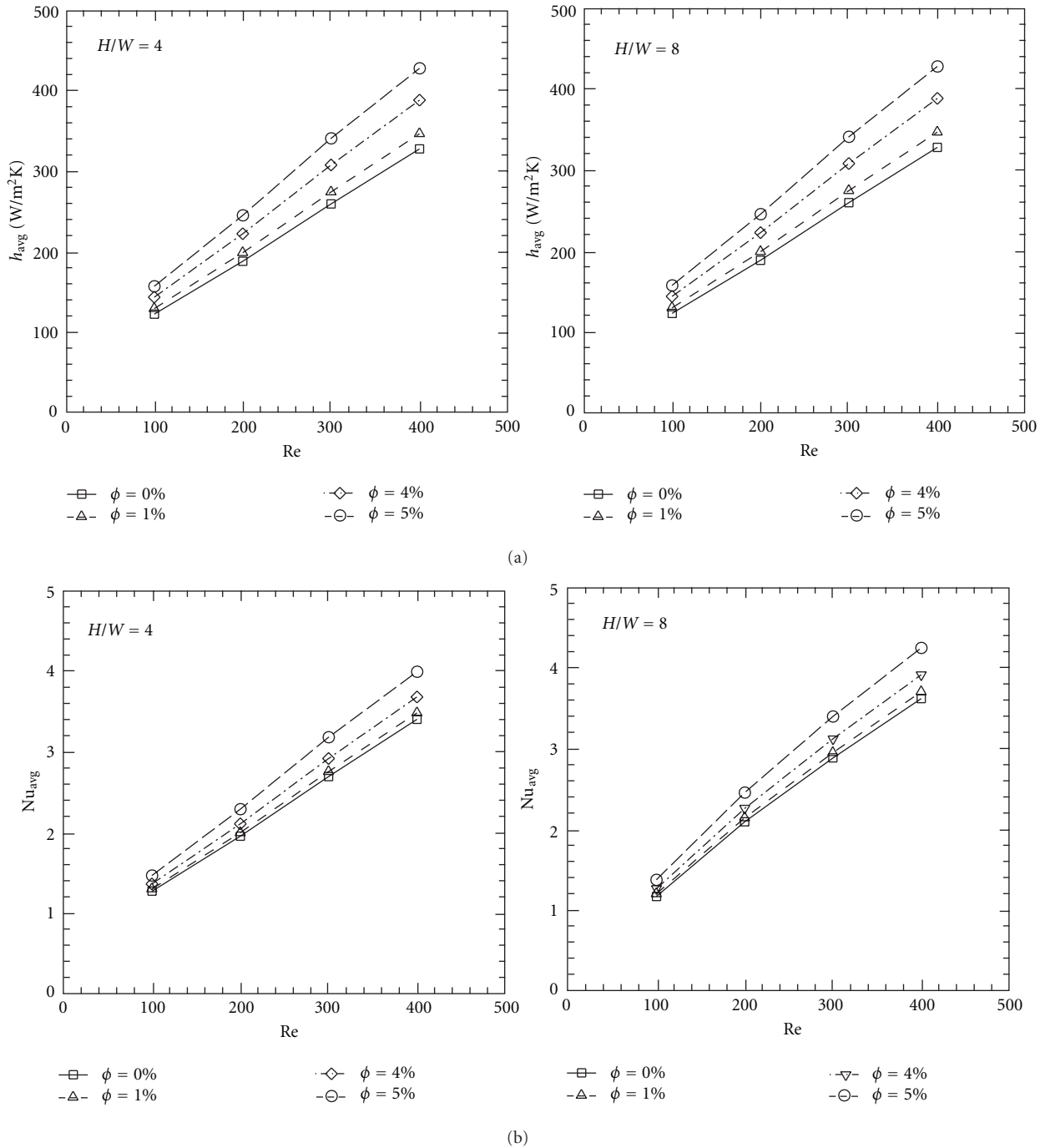


FIGURE 10: Profiles of average heat transfer coefficients and Nusselt number, as a function of Re for different concentrations: (a) convective heat transfer coefficients, $H/W = 4$ and 8 ; (b) Nusselt number, $H/W = 4$ and 8 .

The pumping power ratio, referred to the base fluid values is described in Figure 11 for $H/W = 4$ and 8 and for different values of particle concentrations. The required pumping power is defined as $PP = \dot{V}\Delta P$ and it has a square dependence on Re. However, it is observed that the ratio does not seem to be dependent on Re and H/W ratio. PP_{nf}/PP_{bf} ratio grows as concentration increases, as expected. In fact, at $Re = 200$, the required pumping power is 1.3, 2.1 and 3.9 times

greater than the values calculated in case of water for $\phi = 1\%$, 4% , and 5% , respectively.

7. Conclusions

A numerical analysis of a two-dimensional model on a confined impinging slot jet with nanofluids has been performed in order to evaluate the thermal and fluid-dynamic

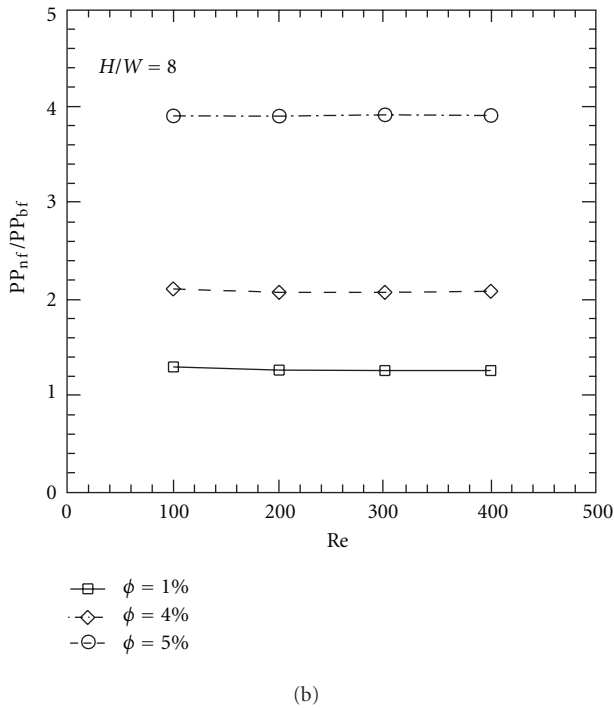
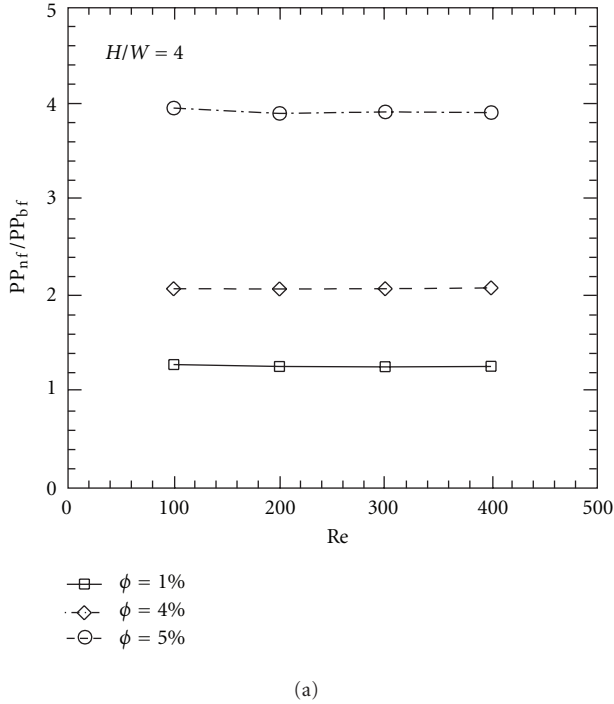


FIGURE 11: Pumping power profiles, referred to the base fluid values, as a function of Re , $\phi = 1\%$, 4% , and 5% : (a) $H/W = 4$; (b) $H/W = 8$.

behaviours. A uniform temperature is applied on the target surface and jet Reynolds number ranges from 100 to 400. The base fluid is water, and different volume concentrations of Al_2O_3 nanoparticles are taken into account by adopting the single-phase model. Furthermore, the confining effects are considered by adopting H/W ratios equal to 4 and 8.

The dimensionless stream function contours showed that the vortex intensity and size depend on the confinement, Reynolds number, and particle concentration values. The introduction of nanoparticle produces an increase of fluid bulk temperature because of the elevated thermal conductivity of nanofluids. The local heat transfer coefficient and Nusselt number values are the highest at the stagnation point and they increase as particle concentrations and Reynolds numbers increase. A maximum increase of 32% in terms of average heat transfer coefficients is detected at $\phi = 5\%$ for $H/W = 8$. The required pumping power increases as well as the Reynolds number and particle concentration and they are at most 3.9 times greater than the values calculated in the case of water.

It should be underlined that the present investigation present the following limits.

- (1) Thermo-physical properties of fluids have been considered constant with temperature because of the small difference between the temperature of the heated target surface and the fluid one in the inlet section. However, temperature-dependent properties for nanofluids could be adopted in future works.
- (2) The use of a two-dimensional slot jet is fair when the lateral length, in the orthogonal direction in respect to the jet, is significant. In particular, Zhou and Lee [61] suggested dimensionless lateral distances, referred to the nozzle width, greater than 6-7 in order to neglect the effect of lateral distance, as also remarked previously.

Nomenclature

Symbols

c_p :	Specific heat (J/kg K)
C_p :	Pressure coefficient Equation(13)
H :	Channel height (m)
h :	Heat transfer coefficient ($W/m^2 K$)
L :	Channel length (m)
Nu :	Nusselt number Equation(11)
P :	Pressure (Pa)
PP :	Required pumping power (W)
$Pr = \nu/a$:	Prandtl number
q :	Target surface heat flux (W/m^2)
Re :	Reynolds number Equation(10)
T :	Temperature (K)
u :	Velocity component (m/s)
\dot{V} :	Volume flow rate (m^3/s)
W :	Jet width (m)
x, y :	Spatial coordinates (m).

Greek Symbols

δ :	Particle distance (m)
θ :	Dimensionless temperature Equation(12)

λ : Thermal conductivity (W/mK)
 μ : Dynamic viscosity (Pa s)
 ν : Kinematic viscosity (m²/s)
 ρ : Density (kg/m³)
 τ : Wall shear stress (kg/m)
 ϕ : Nanoparticle concentration.

Subscripts

0 : Stagnation point
 av : Average
 bf : Base fluid
 f : Fluid
 H : Heated
 j : Jet
 nf : Nanofluid
 p : Particle.

Acknowledgments

This work was supported by SUN with a 2010 grant and by MIUR with Articolo D.M. 593/2000 Grandi Laboratori “EliosLab”.

References

- [1] H. Martin, “Heat and mass transfer between impinging gas jets and solid surfaces,” *Advances in Heat Transfer*, vol. 13, pp. 1–60, 1977.
- [2] S. J. Downs and E. H. James, “Jet impingement heat transfer—a literature survey,” Tech. Rep. 1987-HT-35, ASME, 1987.
- [3] K. Jambunathan, E. Lai, M. A. Moss, and B. L. Button, “A review of heat transfer data for single circular jet impingement,” *International Journal of Heat and Fluid Flow*, vol. 13, no. 2, pp. 106–115, 1992.
- [4] R. Viskanta, “Heat transfer to impinging isothermal gas and flame jets,” *Experimental Thermal and Fluid Science*, vol. 6, no. 2, pp. 111–134, 1993.
- [5] B. W. Webb and C. F. Ma, “Single-phase liquid jet impingement heat transfer,” *Advances in Heat Transfer*, vol. 26, pp. 105–117, 1995.
- [6] V. Tesar and Z. Travnicek, “Increasing heat and/or mass transfer rates in impinging jets,” *Journal of Visualization*, vol. 8, no. 2, pp. 91–98, 2005.
- [7] C. F. Ma and A. E. Bergles, “Convective heat transfer on a small vertical heated surface in an impingement circular liquid jet,” in *Heat Transfer Science and Technology*, B. Wang, Ed., pp. 193–200, Hemisphere, 1990.
- [8] C. F. Ma, “Fundamental research on extremely small size liquid jet impingement heat transfer,” in *Proceedings of the 3rd International Thermal Energy Congress*, pp. 195–202, Kitakyushu, Japan, 1997.
- [9] J. Punch, E. Walsh, R. Grimes, N. Jeffers, and D. Kearney, “Jets and rotary flows for single-phase liquid cooling: an overview of some recent experimental findings,” in *Proceedings of the 11th International Conference on Thermal, Mechanical and Multi-Physics Simulation, and Experiments in Microelectronics and Microsystems (EuroSimE ’10)*, article 5464505, Bordeaux, France, 2010.
- [10] C. F. Ma, J. Yu, D. H. Lei, Y. P. Gan, F. K. Tsou, and H. Auracher, “Transient jet impingement boiling heat transfer on hot surfaces,” in *Multiphase flow and Heat Transfer—Second International Symposium*, X.-J. Chen, T. N. Veziroglu, and L. T. Chang, Eds., pp. 349–357, Hemisphere, 1990.
- [11] R. Viskanta, “Heat transfer in material processing,” in *Handbook of Heat Transfer*, W. M. Rohsenow, J. P. Hartnett, and Y. Cho, Eds., McGraw-Hill, New York, NY, USA, 3rd edition, 1998.
- [12] S. Schuettenberg, F. Krause, M. Hunkel, H. W. Zoch, and U. Fritsching, “Quenching with fluid jets,” *Materialwissenschaft und Werkstofftechnik*, vol. 40, no. 5-6, pp. 408–413, 2010.
- [13] X. Liu, J. H. Lienhard, and J. S. Lombara, “Convective heat transfer by impingement of circular liquid jets,” *Journal of Heat Transfer*, vol. 113, no. 3, pp. 571–582, 1991.
- [14] C. F. Ma, Y. H. Zhao, T. Masuoka, and T. Gomi, “Analytical study on impingement heat transfer with single-phase free-surface circular liquid jets,” *Journal of Thermal Science*, vol. 5, no. 4, pp. 271–277, 1996.
- [15] Y. C. Chen, C. F. Ma, M. Qin, and Y. X. Li, “Theoretical study on impingement heat transfer with single-phase free-surface slot jets,” *International Journal of Heat and Mass Transfer*, vol. 48, no. 16, pp. 3381–3386, 2005.
- [16] Z. H. Lin, Y. J. Chou, and Y. H. Hung, “Heat transfer behaviors of a confined slot jet impingement,” *International Journal of Heat and Mass Transfer*, vol. 40, no. 5, pp. 1095–1107, 1997.
- [17] V. A. Chiriac and A. Ortega, “A numerical study of the unsteady flow and heat transfer in a transitional confined slot jet impinging on an isothermal surface,” *International Journal of Heat and Mass Transfer*, vol. 45, no. 6, pp. 1237–1248, 2002.
- [18] T. H. Park, H. G. Choi, J. Y. Yoo, and S. J. Kim, “Streamline upwind numerical simulation of two-dimensional confined impinging slot jets,” *International Journal of Heat and Mass Transfer*, vol. 46, no. 2, pp. 251–262, 2003.
- [19] D. Sahoo and M. A. R. Sharif, “Numerical modeling of slot-jet impingement cooling of a constant heat flux surface confined by a parallel wall,” *International Journal of Thermal Sciences*, vol. 43, no. 9, pp. 877–887, 2004.
- [20] H. G. Lee, H. S. Yoon, and M. Y. Ha, “A numerical investigation on the fluid flow and heat transfer in the confined impinging slot jet in the low Reynolds number region for different channel heights,” *International Journal of Heat and Mass Transfer*, vol. 51, no. 15-16, pp. 4055–4059, 2008.
- [21] A. Sivasamy, V. Selladurai, and P. R. Kanna, “Jet impingement cooling of a constant heat flux horizontal surface in a confined porous medium: mixed convection regime,” *International Journal of Heat and Mass Transfer*, vol. 53, no. 25-26, pp. 5847–5855, 2010.
- [22] D. Lytle and B. W. Webb, “Air jet impingement heat transfer at low nozzle-plate spacings,” *International Journal of Heat and Mass Transfer*, vol. 37, no. 12, pp. 1687–1697, 1994.
- [23] M. Behnia, S. Parneix, Y. Shabany, and P. A. Durbin, “Numerical study of turbulent heat transfer in confined and unconfined impinging jets,” *International Journal of Heat and Fluid Flow*, vol. 20, no. 1, pp. 1–9, 1999.
- [24] K. S. Choo and S. J. Kim, “Comparison of thermal characteristics of confined and unconfined impinging jets,” *International Journal of Heat and Mass Transfer*, vol. 53, no. 15-16, pp. 3366–3371, 2010.
- [25] M. A. R. Sharif and A. Banerjee, “Numerical analysis of heat transfer due to confined slot-jet impingement on a moving plate,” *Applied Thermal Engineering*, vol. 29, no. 2-3, pp. 532–540, 2009.

- [26] K. Ibuki, T. Umeda, H. Fujimoto, and H. Takuda, "Heat transfer characteristics of a planar water jet impinging normally or obliquely on a flat surface at relatively low Reynolds numbers," *Experimental Thermal and Fluid Science*, vol. 33, no. 8, pp. 1226–1234, 2009.
- [27] F. T. Dórea and M. J. S. de Lemos, "Simulation of laminar impinging jet on a porous medium with a thermal non-equilibrium model," *International Journal of Heat and Mass Transfer*, vol. 53, no. 23-24, pp. 5089–5101, 2010.
- [28] Y. T. Yang, T. C. Wei, and Y. H. Wang, "Numerical study of turbulent slot jet impingement cooling on a semi-circular concave surface," *International Journal of Heat and Mass Transfer*, vol. 54, no. 1–3, pp. 482–489, 2011.
- [29] L. B. Y. Aldabbagh and A. A. Mohamad, "A three-dimensional numerical simulation of impinging jet arrays on a moving plate," *International Journal of Heat and Mass Transfer*, vol. 52, no. 21-22, pp. 4894–4900, 2009.
- [30] P. Naphon and S. Wongwises, "Investigation on the jet liquid impingement heat transfer for the central processing unit of personal computers," *International Communications in Heat and Mass Transfer*, vol. 37, no. 7, pp. 822–826, 2010.
- [31] M. F. Koseoglu and S. Baskaya, "Experimental and numerical investigation of natural convection effects on confined impinging jet heat transfer," *International Journal of Heat and Mass Transfer*, vol. 52, no. 5-6, pp. 1326–1336, 2009.
- [32] D. W. Colucci and R. Viskanta, "Effect of nozzle geometry on local convective heat transfer to a confined impinging air jet," *Experimental Thermal and Fluid Science*, vol. 13, no. 1, pp. 71–80, 1996.
- [33] N. Gao and D. Ewing, "Investigation of the effect of confinement on the heat transfer to round impinging jets exiting a long pipe," *International Journal of Heat and Fluid Flow*, vol. 27, no. 1, pp. 33–41, 2006.
- [34] S. U. S. Choi, "Enhancing thermal conductivity of fluids with nanoparticles, developments and applications of non-newtonian flows," *ASME: Fluids Engineering Division*, vol. 231, pp. 99–105, 1995.
- [35] J. Buongiorno, "Convective transport in nanofluids," *Journal of Heat Transfer*, vol. 128, no. 3, pp. 240–250, 2006.
- [36] W. Yu, D. M. France, J. L. Routbort, and S. U. S. Choi, "Review and comparison of nanofluid thermal conductivity and heat transfer enhancements," *Heat Transfer Engineering*, vol. 29, no. 5, pp. 432–460, 2008.
- [37] S. U. S. Choi, "Nanofluids: from vision to reality through research," *Journal of Heat Transfer*, vol. 131, no. 3, pp. 1–9, 2009.
- [38] J. Buongiorno, D. C. Venerus, N. Prabhat et al., "A benchmark study on the thermal conductivity of nanofluids," *Journal of Applied Physics*, vol. 106, no. 9, Article ID 094312, 2009.
- [39] S. Özerinç, S. Kakaç, and A. G. Yazıcıoğlu, "Enhanced thermal conductivity of nanofluids: a state-of-the-art review," *Microfluidics and Nanofluidics*, vol. 8, no. 2, pp. 145–170, 2010.
- [40] L. Wang and J. Fan, "Nanofluids research: key issues," *Nanoscale Research Letters*, vol. 5, no. 8, pp. 1241–1252, 2010.
- [41] L. Godson, B. Raja, D. M. Lal, and S. Wongwises, "Enhancement of heat transfer using nanofluids—an overview," *Renewable and Sustainable Energy Reviews*, vol. 14, no. 2, pp. 629–641, 2010.
- [42] A. V. Kuznetsov and D. A. Nield, "Natural convective boundary-layer flow of a nanofluid past a vertical plate," *International Journal of Thermal Sciences*, vol. 49, no. 2, pp. 243–247, 2010.
- [43] D. A. Nield and A. V. Kuznetsov, "The onset of convection in a horizontal nanofluid layer of finite depth," *European Journal of Mechanics B-Fluids*, vol. 29, no. 3, pp. 217–223, 2010.
- [44] A. V. Kuznetsov and D. A. Nield, "Double-diffusive natural convective boundary-layer flow of a nanofluid past a vertical plate," *International Journal of Thermal Sciences*, vol. 50, pp. 712–717, 2011.
- [45] P. Koblinski, R. Prasher, and J. Eapen, "Thermal conductance of nanofluids: is the controversy over?" *Journal of Nanoparticle Research*, vol. 10, no. 7, pp. 1089–1097, 2008.
- [46] I. Gherasim, G. Roy, C. T. Nguyen, and D. Vo-Ngoc, "Heat transfer enhancement and pumping power in confined radial flows using nanoparticle suspensions (nanofluids)," *International Journal of Thermal Sciences*, vol. 50, pp. 369–377, 2011.
- [47] Z. H. Liu and Y. H. Qiu, "Boiling heat transfer characteristics of nanofluids jet impingement on a plate surface," *Heat and Mass Transfer/Waerme und Stoffuebertragung*, vol. 43, no. 7, pp. 699–706, 2007.
- [48] Z. H. Liu and Y. H. Qiu, "The boiling heat transfer of water based nanofluid jet impingement on a plate surface," *Journal of Shanghai Jiaotong University*, vol. 41, no. 10, pp. 1658–1661, 2007.
- [49] G. C. Roy, C. T. Nguyen, and M. Comeau, "Numerical investigation of electronic component cooling enhancement using nanofluids in a radial flow cooling system," *Journal of Enhanced Heat Transfer*, vol. 13, no. 2, pp. 101–115, 2006.
- [50] G. Roy, C. T. Nguyen, and P. R. Lajoie, "Numerical investigation of laminar flow and heat transfer in a radial flow cooling system with the use of nanofluids," *Superlattices and Microstructures*, vol. 35, no. 3–6, pp. 497–511, 2004.
- [51] S. J. Palm, G. Roy, and C. T. Nguyen, "Heat transfer enhancement with the use of nanofluids in radial flow cooling systems considering temperature-dependent properties," *Applied Thermal Engineering*, vol. 26, no. 17-18, pp. 2209–2218, 2006.
- [52] G. Roy, S. J. Palm, and C. T. Nguyen, "Heat transfer and fluid flow of nanofluids in laminar radial flow cooling systems," *Journal of Thermal Science*, vol. 14, no. 4, pp. 362–367, 2005.
- [53] P. Vaziei and O. Abouali, "Numerical study of fluid flow and heat transfer for Al_2O_3 -water nanofluid impinging jet," in *Proceedings of the 7th International Conference on Nanochannels, Microchannels, and Minichannels (ICNMM '09)*, pp. 977–984, Pohang, Korea, June 2009.
- [54] Y. Feng and C. Kleinstreuer, "Nanofluid convective heat transfer in a parallel-disk system," *International Journal of Heat and Mass Transfer*, vol. 53, no. 21-22, pp. 4619–4628, 2010.
- [55] Y. T. Yang and F. H. Lai, "Numerical study of heat transfer enhancement with the use of nanofluids in radial flow cooling system," *International Journal of Heat and Mass Transfer*, vol. 53, no. 25-26, pp. 5895–5904, 2010.
- [56] Y. T. Yang and F. H. Lai, "Numerical investigation of cooling performance with the use of Al_2O_3 /water nanofluids in a radial flow system," *International Journal of Thermal Sciences*, vol. 50, no. 1, pp. 61–72, 2011.
- [57] O. Manca, P. Mesolella, S. Nardini, and D. Ricci, "Numerical study of a confined slot impinging jet with nanofluids," *Nanoscale Research Letters*, vol. 6, no. 1, p. 188, 2011.
- [58] C. T. Nguyen, N. Galanis, G. Polidori, S. Fohanno, C. V. Popa, and A. Le Behec, "An experimental study of a confined and submerged impinging jet heat transfer using Al_2O_3 -water nanofluid," *International Journal of Thermal Sciences*, vol. 48, no. 2, pp. 401–411, 2009.
- [59] I. Gherasim, G. Roy, C. T. Nguyen, and D. Vo-Ngoc, "Experimental investigation of nanofluids in confined laminar radial flows," *International Journal of Thermal Sciences*, vol. 48, no. 8, pp. 1486–1493, 2009.

- [60] FLUENT *Computational Fluid Dynamic Code Version 6.3 User Guide*, Fluent Inc., <http://www.fluent.com/>.
- [61] D. W. Zhou and S. J. Lee, "Forced convective heat transfer with impinging rectangular jets," *International Journal of Heat and Mass Transfer*, vol. 50, no. 9-10, pp. 1916–1926, 2007.
- [62] W. M. Rohsenow, J. P. Hartnett, and Y. I. Cho, *Handbook of Heat Transfer*, McGraw-Hill, New York, NY, USA, 3rd edition, 1998.
- [63] B. C. Pak and Y. I. Cho, "Hydrodynamic and heat transfer study of dispersed fluids with submicron metallic oxide particles," *Experimental Heat Transfer*, vol. 11, no. 2, pp. 151–170, 1998.
- [64] S. E. B. Maïga, C. T. Nguyen, N. Galanis, G. Roy, T. Maré, and M. Coqueux, "Heat transfer enhancement in turbulent tube flow using Al_2O_3 nanoparticle suspension," *International Journal of Numerical Methods for Heat and Fluid Flow*, vol. 16, no. 3, pp. 275–292, 2006.
- [65] N. Masoumi, N. Sohrabi, and A. Behzadmehr, "A new model for calculating the effective viscosity of nanofluids," *Journal of Physics D*, vol. 42, 2009.
- [66] C. H. Chon, K. D. Kihm, S. P. Lee, and S. U. S. Choi, "Empirical correlation finding the role of temperature and particle size for nanofluid (Al_2O_3) thermal conductivity enhancement," *Applied Physics Letters*, vol. 87, no. 15, Article ID 153107, pp. 1–3, 2005.
- [67] Y. J. Chou and Y. H. Hung, "Impingement cooling of an isothermally heated surface with a confined slot jet," *Journal of Heat Transfer*, vol. 116, no. 2, pp. 479–482, 1994.

Research Article

Remarks on Constitutive Modeling of Nanofluids

Mehrdad Massoudi and Tran X. Phuoc

U.S. Department of Energy, National Energy Technology Laboratory (NETL), 626 Cochran Mill Road, P.O. Box 10940, Pittsburgh, PA 15236, USA

Correspondence should be addressed to Mehrdad Massoudi, mehrdad.massoudi@netl.doe.gov

Received 23 February 2011; Accepted 12 July 2011

Academic Editor: Oronzio Manca

Copyright © 2012 M. Massoudi and T. X. Phuoc. This is an open access article distributed under the Creative Commons Attribution License, which permits unrestricted use, distribution, and reproduction in any medium, provided the original work is properly cited.

We discuss briefly the constitutive modeling of the stress tensor for nanofluids. In particular, we look at the viscosity of nanofluids containing multiwalled carbon nanotubes (MWCNTs) stabilized by cationic chitosan. MWCNTs can be used either to enhance or reduce the fluid base viscosity depending on their weight fractions. By assuming that MWCNT nanofluids behave as generalized second-grade fluid where the viscosity coefficient depends upon the rate of deformation, a theoretical model is developed. A simplified version of this model, similar to the traditional power-law model, is used in this study. It is observed that the theoretical results agree well with the experimental data.

1. Introduction

Nanofluids are made by adding nanoscale particles in low volumetric fractions to a fluid in order to enhance or improve their rheological, mechanical, optical, and thermal properties. The base fluid can be any liquid such as oil, water, ethylene glycol, or conventional fluid mixtures. Limited available studies on nanofluid viscosity have been reported [1–19]. In most of these studies, the behavior of the viscosity and the shear stress of nanofluids have been interpreted using the widely used empirical model developed by Casson [20]

$$\tau^{1/2} = \tau_0^{1/2} + \mu_\infty^{1/2} \dot{\gamma}^{1/2}. \quad (1)$$

In this equation, τ_0 is the yield stress, μ_∞ is the suspension viscosity at infinite shear rate, and $\dot{\gamma}$ is the shear rate. One of the inherent limitations of such empirical models is that they are, in general, one-dimensional in nature and it is not that easy or straightforward to generalize and obtain the appropriate 3-dimensional form, which are often necessary to solve general 3-dimensional problems. Nevertheless, this equation has been found to be successful for a range of parameters and a class of fluids. Phuoc and Massoudi [14] used this equation and obtained the values for μ_∞ being 0.1225 cp and 0.0225 cp for Fe_2O_3 —deionized water nanofluids with polyvinylpyrrolidone (PVP) or polyethylene

oxide (PEO) as a dispersant, respectively. These values are about two orders of magnitude lower than the viscosity of the base fluid (a liquid prepared with PVP as a dispersant (DW-0.2% PVP) had a viscosity similar to that of water, while the viscosity of water with PEO as a dispersant (DW-0.2% PEO) was about 12.5 cp). Choi et al. [8] used this equation and calculated the intrinsic viscosities of CrO_2 —ethylene glycol, γ - Fe_2O_3 , α - Fe_2O_3 —EG and Ba-ferrite-EG nanofluids at infinite shear rate and reported a decrease of the viscosity with an increase in the particle volume fraction. This could be problematic, since the intrinsic viscosity should reach the viscosity of the base fluid in case of dilute suspensions or increase as the particle volume fraction increases if the suspension is dense enough.

In general, most complex, that is, nonlinear, materials exhibit unusual and peculiar characteristics such as viscoelasticity (as, for example, identified by creep or relaxation experiments, often exhibiting memory effects), yield stress, normal stress differences. The science of studying nonlinear fluids is “Rheology” and according to Reiner [21, p. 457]: “rheology started when Bingham in 1916 investigated concentrated clay-suspensions, and Bingham and Green in 1919 investigated oilpaints.” The non-linear time-dependent response of complex fluids constitutes an important area of mathematical modeling of non-Newtonian fluids. For many

practical engineering cases, where complex fluids such as paint and slurries are used, the shear viscosity can be a function of one or all of the following:

- (i) Time,
- (ii) shear rate,
- (iii) concentration,
- (iv) temperature,
- (v) pressure,
- (vi) electric field,
- (vii) magnetic field,
- (viii)

Thus, in general, $\mu = \mu(t, \pi, \theta, \phi, p, \mathbf{E}, \mathbf{B}, \dots)$, where t is the time, π is some measure of the shear rate, θ the temperature, ϕ the concentration, p the pressure, \mathbf{E} the electric field, and \mathbf{B} the magnetic field. Of course, in certain materials or under certain conditions, the dependence of one or more of these can be dropped. A more appropriate question is not what the shear viscosity should be, but rather, what the stress tensor of a given fluid should be. Bingham [22] was one of the first scientists who proposed a constitutive relation for the stress tensor of a viscoplastic material in a simple one dimensional shear flow, where the relationship between the shear stress and the rate of shear was described in terms of a yield function $F = 1 - \tau_0/|\tau|$ where τ_0 is the yield stress and τ is the shear stress. For many fluids such as polymers, slurries, and suspensions, some generalizations have been made to model shear-dependent viscosities. These fluids are known as the power-law or the generalized Newtonian fluid models; these widely used models are deficient in many ways; for example, they cannot predict the normal stress differences or yield stresses and they cannot capture the memory or history effects [23, 24].

In an effort to obtain a model that does exhibit both normal stress effects and shear-thinning/thickening, Man [25] modified the constitutive equation developed by Rivlin and Ericksen [26] (see also [27, 28]) for a second-grade fluid by allowing the viscosity coefficient to depend upon the rate of deformation; that is, $\mu_{\text{eff}} = \mu\Pi^{m/2}$, where Π is the second invariant of the symmetric part of the velocity gradient, and m is a material parameter. When $m < 0$, the fluid is shear-thinning, and if $m > 0$, the fluid is shear-thickening. In this paper, the viscosity of nanofluids containing multiwalled carbon nanotubes (MWCNTs) stabilized by cationic chitosan is studied. MWCNTs can be used either to enhance or reduce the fluid base viscosity depending on their weight fractions. By assuming that MWCNT nanofluids behave as a generalized second-grade fluid, where the viscosity coefficient depends upon the rate of deformation, a theoretical model is developed, and comparisons are made with the experimental data.

2. Constitutive Modeling

Mathematically, the purpose of constitutive relations in mechanics is to supply connections between kinematic,

mechanical, and thermal fields providing a suitable formulation of a problem which can be solved for properly posed problems. Just as different figures in geometry are defined as idealizations of natural objects, continuum mechanics seeks to establish particular relations between the stress tensor and the motion of the body for "ideal materials" [27]. In some instances, it may be necessary to represent the same real material by different ideal materials in different circumstances. A classic example is that of the theory of incompressible viscous fluids, which gives an excellent description of the behavior of water flowing through pipes but is useless for the study of the propagation of sound waves through water. While a constitutive equation is a postulate or a definition from the mathematical standpoint, physical experience remains the first guide, perhaps reinforced by experimental data. Constitutive relations are required to satisfy some general principles. Wang and Truesdell [29, page 135] list six general principles: (1) determinism, (2) local action, (3) equipresence, (4) universal dissipation, (5) material frame indifference, and (6) material symmetry. Constitutive relations should hold equally in all inertial coordinate systems at any given time (often referred to as coordinate invariance requirement). This would guard against proposing a relation in which a mere change of coordinate description would imply a different response in the material. Many of the so-called "power-law" models used in describing non-Newtonian fluids are not coordinate invariant. In general, this difficulty can easily be overcome by stating the equations either in tensorial form or by using direct notations not employing coordinates at all. The principle of material frame-indifference (sometimes referred to as objectivity), which requires that the constitutive equations be invariant under changes of frame, is perhaps the most important of all. It is a consequence of a fundamental principle of classical physics that material properties are indifferent, that is, independent of the frame of reference of the observer. This principle requires that constitutive relations depend only on frame-indifferent forms (or combinations thereof) of the variables pertaining to the given problem (see Massoudi [30] for further details). Among other approaches to model complex materials, one can list (i) using physical and experimental models, (ii) doing numerical simulations, (iii) using statistical mechanics approaches, and (iv) ad hoc approaches.

In general, based on available experimental observations, it can be said that many nanofluids exhibit characteristics similar to those of non-linear materials such as colloidal suspensions, polymers, rubber, and granular materials. The main points of departure from linear behavior are the following:

- (1) the ability to shear-thin or shear-thicken,
- (2) the ability to creep,
- (3) the ability to relax stresses,
- (4) the presence of normal stress differences in simple shear flows,
- (5) the presence of yield stress.

To the best of our knowledge, it has not been reported whether nanofluids exhibit normal stress effects, the non-linear phenomena related to the stresses that are developed orthogonal to the planes of shear. Therefore, we propose to use a general model that can exhibit both the normal stress effects and the shear-thinning/thickening effects. To do so, we assume that nanofluids, such as the one studied in the present work, behave as generalized second-grade fluids. For a second grade fluid, the Cauchy stress tensor is given by [26–28]

$$\mathbf{T} = -p\mathbf{1} + \mu\mathbf{A}_1 + \alpha_1\mathbf{A}_2 + \alpha_2\mathbf{A}_1^2, \quad (2)$$

where p is the indeterminate part of the stress due to the constraint of incompressibility, $\mathbf{1}$ is the identity tensor, μ is the coefficient of viscosity, α_1 and α_2 are material moduli which are commonly referred to as the normal stress coefficients. The kinematical tensors \mathbf{A}_1 and \mathbf{A}_2 are defined through

$$\begin{aligned} \mathbf{A}_1 &= \mathbf{L} + \mathbf{L}^T, \\ \mathbf{A}_2 &= \frac{d\mathbf{A}_1}{dt} + \mathbf{A}_1\mathbf{L} + \mathbf{L}^T\mathbf{A}_1, \\ \mathbf{L} &= \text{gradu}. \end{aligned} \quad (3)$$

where d/dt is the total time derivative, given by $d(\cdot)/dt = \partial(\cdot)/\partial t + [\text{grad}(\cdot)]\mathbf{u}$, where \mathbf{u} is the velocity vector. The thermodynamics and stability of fluids of second grade have been studied in detail [28], where it is shown that if the fluid is to be thermodynamically consistent in the sense that all motions of the fluid meet the Clausius-Duhem inequality and that the specific Helmholtz free energy of the fluid be a minimum in equilibrium, then

$$\begin{aligned} \mu &\geq 0, \\ \alpha_1 &\geq 0, \\ \alpha_1 + \alpha_2 &= 0. \end{aligned} \quad (4)$$

By allowing the viscosity coefficient to depend on the rate of deformation, Man [25] modified the constitutive equation, (2) and proposed the following:

$$\mathbf{T} = -p\mathbf{1} + \mu\Pi^{m/2}\mathbf{A}_1 + \alpha_1\mathbf{A}_2 + \alpha_2\mathbf{A}_1^2, \quad (5)$$

where

$$\Pi = \frac{1}{2} \text{tr} \mathbf{A}_1^2 \quad (6)$$

is the second invariant of the symmetric part of the velocity gradient, and m is a material parameter. When $m < 0$, the fluid is shear-thinning, and if $m > 0$, the fluid is shear-thickening. A subclass of models given by (7) is the generalized power-law model, which can be obtained by setting $\alpha_1 = \alpha_2 = 0$ in (7) (see [31–34] for further discussions of this model). Notice that if the normal stress parameters α_1 and α_2 are zero, then

$$\mathbf{T} = -p\mathbf{1} + \mu\Pi^{m/2}\mathbf{A}_1. \quad (7)$$

In this paper, we will use this simplified form, which can also be considered as a generalized power-law fluid model. Using

the cylindrical coordinate system for our present measurements and assuming $\mathbf{u} = w(r)\mathbf{e}_z$ where \mathbf{e}_z denotes a unit vector along the z direction yields the following calculations

$$\begin{aligned} \mathbf{A}_1 &= \begin{bmatrix} 0 & 0 & \frac{\partial w}{\partial r} \\ 0 & 0 & 0 \\ \frac{\partial w}{\partial r} & 0 & 0 \end{bmatrix}, \\ \mathbf{A}_1^2 &= \begin{bmatrix} \left(\frac{\partial w}{\partial r}\right)^2 & 0 & 0 \\ 0 & 0 & 0 \\ 0 & 0 & \left(\frac{\partial w}{\partial r}\right)^2 \end{bmatrix}, \\ \Pi &= \frac{1}{2} \left[2 \left(\frac{\partial w}{\partial r} \right)^2 \right]. \end{aligned} \quad (8)$$

The z -component of the stress tensor becomes

$$T_{rz} = \mu \left[\left(\frac{\partial w}{\partial r} \right)^2 \right]^{m/2} \left(\frac{\partial w}{\partial r} \right) = (\mu\dot{\gamma}^m)\dot{\gamma}, \quad (9)$$

where the shear-dependent viscosity is defined as

$$\mu_{\text{eff}} = \mu \left[\left(\frac{\partial w}{\partial r} \right)^2 \right]^{m/2} = \mu\dot{\gamma}^m. \quad (10)$$

In the next section, we will briefly discuss the results of our experimental investigation and show how this model can be used to describe the observed behavior of the fluid.

3. Experimental Evaluation

In Figures 1 and 2, we present the results on the calculated and measured viscosity and shear stress for water-based nanofluids containing Multiwalled carbon nanotubes (MWCNT) stabilized by low molecular weight chitosan (>75% deacetylation). The measured data were reported by Phuoc et al. [15]. The calculated results are carried out using (9) for the shear stress and (10) for the viscosity with $m = -0.547, -0.65,$ and -0.647 and $\mu = 0.134, 0.331,$ and 0.523 when CNTs weight percent increased from 1 to 3 and the weight percent of the chitosan was 0.1. While using 0.2 wt% chitosan, it was found that $m = -0.584$ and -0.678 and $\mu = 0.354$ and 0.641 for 2 wt% and 3 wt% CNTs, respectively. It is seen that using the generalized power-law model, with (7) as a subclass of the generalized second-grade fluid models, the measured experimental values compare well with the theoretical model. For a given weight percent of the stabilizer, increasing the CNTs weight percent has a strong effect on the value of μ . For a given value of CNTs weight percent, increasing the weight percent of the stabilizer increases both m and μ .

4. Concluding Remarks

The two important constitutive relations needed for the study of flow and heat transfer in complex fluid-like

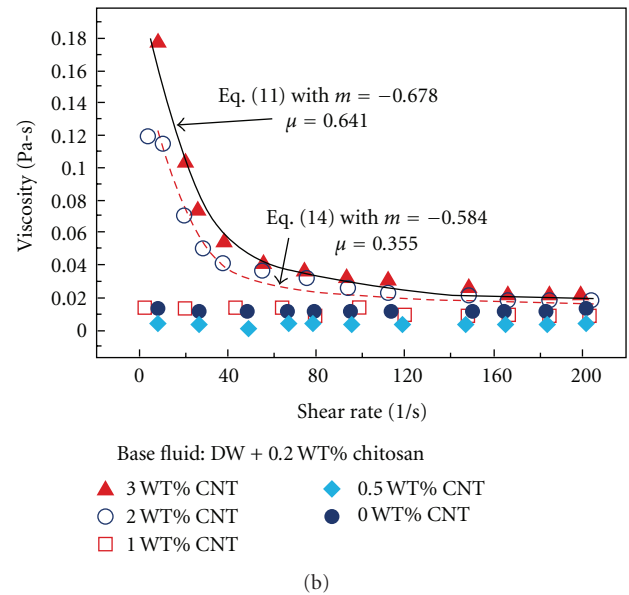
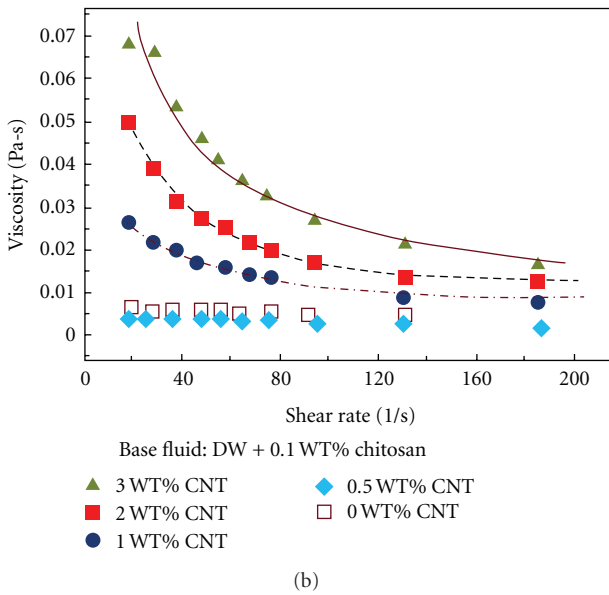
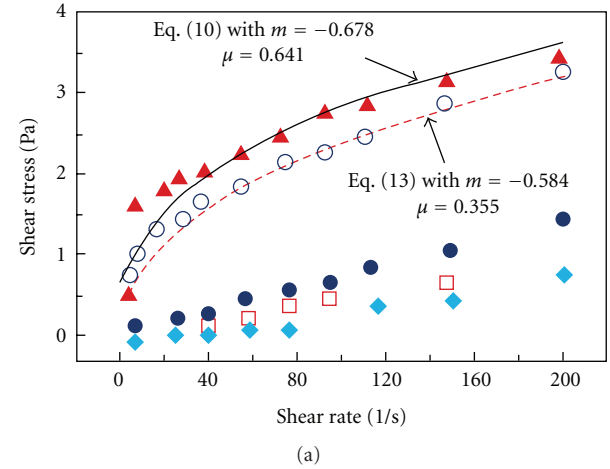
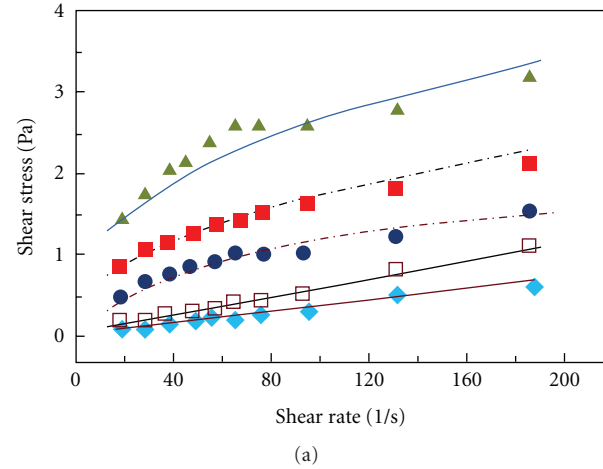


FIGURE 1: Viscosity and shear stress as a function of shear rate showing the effect of the MWCNT weight percent. The base fluid is DW + 0.1 wt% chitosan. The measured values are shown by symbols, while the calculated values are shown by the solid and dotted lines. These calculated viscosity values were obtained using (10) and the shear stresses were calculated using (9) with $m = -0.547, -0.65,$ and -0.647 and $\mu = 0.134; 0.331;$ and 0.523 for MWCNT weight percent increased from 1%, 2%, and to 3%, respectively.

FIGURE 2: Viscosity and shear stress as a function of shear rate showing the effect of the MWCNT weight percent. The base fluid is DW + 0.2 wt% chitosan. The measured values are shown by symbols, while the calculated values are shown by the solid and dotted lines. These calculated viscosity values were obtained using (10) and the shear stresses were calculated using (9) with $m = -0.584$ and -0.678 and $\mu = 0.354$ and 0.641 for 2 wt% and 3 wt% CNTs, respectively.

materials, where the effects of radiation are ignored, are the stress tensor and the heat flux vector. From an engineering perspective, this oftentimes translates into measuring viscosity and thermal conductivity. As a result, most researchers have attempted to generalize Newton's law of viscosity and Fourier's law of heat conduction to various and more complicated cases by assuming that the shear viscosity and/or thermal conductivity could depend on a host of parameters such as shear rate, temperature, and porosity. This unfortunately does not fully take into account the non-linear and time-dependent nature (such as normal stress effects or visco-elastic response) of these complex

materials, as these generalizations cannot give rise to implicit constitutive relations.

Nanofluids represent one of the newest complex materials of the modern era. In many ways, constitutive modeling of these fluids, from a macroscopic point of view, is still at its infancy, perhaps similar to the early days of polymer rheology, rubber viscoelasticity or composite materials. With intense interest and research in the past two decades, great strides have been made, and nanofluids, due to their peculiar heat transfer and rheological properties, have been shown to contribute in many diverse ways to many industrial processes and to our lives [35]. An often neglected, yet extremely important, conceptual question, and perhaps still

an open question, is whether the same governing macroscopic balance equations can be used for nanofluids. For a recent discussion of this issue, see [36]. Since nanofluids form suspensions, theoretically from the point of view of mechanics, their thermorheological responses can be modeled either using the non-Newtonian approach or the multicomponent approach [37].

To better understand the various mechanisms in the heat transfer processes involving nanofluids, in addition to studying the thermal conductivity or radiation effects, an understanding of the mechanism for viscous dissipation is also important. A proper constitutive model for the stress tensor \mathbf{T} , represents the first step in this direction, since the term $\mathbf{T} \cdot \mathbf{D}$ (where $2\mathbf{D} = \mathbf{A}_1$) appears in the energy equation. By assuming that nanofluids in general can behave as generalized second-grade fluids whose viscosity coefficient depends on the rate of deformation, a theoretical model has been developed. The experimental results indicate that the two important parameters in this study are related to the effects of the solid concentration on the viscosity of the base fluid and the degree of the nonlinearity of the fluid (measured through m and μ). By comparing with the measured data, the present model was found to be suitable for describing the fluid behavior. To test to see whether a particular nanofluid is capable of displaying normal stress differences, an orthogonal rheometer is needed.

Acknowledgments

This work was supported by DOE-NETL under the EPact Complementary program.

References

- [1] J. H. Lee, K. S. Hwang, S. P. Jang et al., "Effective viscosities and thermal conductivities of aqueous nanofluids containing low volume concentrations of Al₂O₃ nanoparticles," *International Journal of Heat and Mass Transfer*, vol. 51, no. 11-12, pp. 2651–2656, 2008.
- [2] R. Prasher, D. Song, J. Wang, and P. Phelan, "Measurements of nanofluid viscosity and its implications for thermal applications," *Applied Physics Letters*, vol. 89, no. 13, Article ID 133108, 2006.
- [3] P. K. Namburu, D. P. Kulkarni, D. Misra, and D. K. Das, "Viscosity of copper oxide nanoparticles dispersed in ethylene glycol and water mixture," *Experimental Thermal and Fluid Science*, vol. 32, no. 2, pp. 397–402, 2007.
- [4] S. M. S. Murshed, K. C. Leong, and C. Yang, "Investigations of thermal conductivity and viscosity of nanofluids," *International Journal of Thermal Sciences*, vol. 47, no. 5, pp. 560–568, 2008.
- [5] K. Kwak and C. Kim, "Viscosity and thermal conductivity of copper oxide nanofluid dispersed in ethylene glycol," *Korea Australia Rheology Journal*, vol. 17, no. 2, pp. 35–40, 2005.
- [6] D. P. Kulkarni, D. K. Das, and G. A. Chukwu, "Temperature dependent rheological property of copper oxide nanoparticles suspension," *Journal of Nanoscience and Nanotechnology*, vol. 6, no. 4, pp. 1150–1154, 2006.
- [7] B. Wang, L. Zhou, and X. Peng, "Viscosity, thermal diffusivity and Prandtl number of nanoparticle suspensions," *Progress in Natural Science*, vol. 14, no. 10, pp. 922–926, 2004.
- [8] H. J. Choi, T. M. Kwon, and M. S. Jhon, "Effects of shear rate and particle concentration on rheological properties of magnetic particle suspensions," *Journal of Materials Science*, vol. 35, no. 4, pp. 889–894, 2000.
- [9] T. M. Kwon, M. S. Jhon, and H. J. Choi, "Viscosity of magnetic particle suspension," *Journal of Molecular Liquids*, vol. 75, no. 2, pp. 115–126, 1998.
- [10] M. C. Yang, L. E. Scriven, and C. W. Macosko, "Some rheological measurements on magnetic iron-oxide suspensions in silicon oil," *Journal of Rheology*, vol. 30, no. 5, pp. 1015–1029, 1986.
- [11] J. Avsec and M. Oblak, "The calculation of thermal conductivity, viscosity and thermodynamic properties for nanofluids on the basis of statistical nanomechanics," *International Journal of Heat and Mass Transfer*, vol. 50, no. 21-22, pp. 4331–4341, 2007.
- [12] C. T. Nguyen, F. Desgranges, N. Galanis et al., "Viscosity data for Al₂O₃-water nanofluid-hysteresis: is heat transfer enhancement using nanofluids reliable?" *International Journal of Thermal Sciences*, vol. 47, no. 2, pp. 103–111, 2008.
- [13] H. Chen, Y. Ding, and C. Tan, "Rheological behavior of nanofluids," *New Journal of Physics*, vol. 9, pp. 367–382, 2007.
- [14] T. X. Phuoc and M. Massoudi, "Experimental observations of the effects of shear rates and particle concentration on the viscosity of Fe₂O₃-deionized water nanofluids," *International Journal of Thermal Sciences*, vol. 48, no. 7, pp. 1294–1301, 2009.
- [15] T. X. Phuoc, M. Massoudi, and R. H. Chen, "Viscosity and thermal conductivity of nanofluids containing multi-walled carbon nanotubes stabilized by chitosan," *International Journal of Thermal Sciences*, vol. 50, no. 1, pp. 12–18, 2011.
- [16] V. Bianco, O. Manca, and S. Nardini, "Numerical simulation of water/ Al₂O₃ nanofluid turbulent convection," *Advances in Mechanical Engineering*, vol. 2010, Article ID 976254, 10 pages, 2010.
- [17] C. H. Li and G. P. Peterson, "Experimental studies of natural convection heat transfer of Al₂O₃/DI water nanoparticle suspensions (Nanofluids)," *Advances in Mechanical Engineering*, vol. 2010, Article ID 742739, 10 pages, 2010.
- [18] S. Torii, "Turbulent heat transfer behavior of nanofluid in a circular tube heated under constant heat flux," *Advances in Mechanical Engineering*, vol. 2010, Article ID 917612, 7 pages, 2010.
- [19] K. V. Wong and M. J. Castillo, "Heat transfer mechanisms and clustering in nanofluids," *Advances in Mechanical Engineering*, vol. 2010, Article ID 795478, 9 pages, 2010.
- [20] N. Casson, "A flow equation for pigment-oil suspensions of the printing ink type," in *Rheology of Disperse Systems*, C. C. Mill, Ed., Pergamon, New York, NY, USA, 1959.
- [21] M. Reiner, "Rheology," in *Handbuch Der Physik*, S. Flugge, Ed., vol. VI, Springer, Berlin, Germany, 1958.
- [22] E. C. Bingham, *Fluidity and Plasticity*, McGraw-Hill, New York, NY, USA, 1922.
- [23] R. G. Larson, *The Structure and Rheology of Complex Fluids*, Oxford University Press, New York, NY, USA, 1999.
- [24] R. B. Bird, R. C. Armstrong, and J. Hassager, *Dynamics of Polymeric Liquids*, vol. 1, John Wiley & Sons, New York, NY, USA, 1977.
- [25] C. S. Man, "Nonsteady channel flow of ice as a modified second-order fluid with power-law viscosity," *Archive for*

- Rational Mechanics and Analysis*, vol. 119, no. 1, pp. 35–57, 1992.
- [26] R. S. Rivlin and J. L. Ericksen, “Stress deformation relations for isotropic materials,” *Journal of Rational Mechanics and Analysis*, vol. 4, pp. 323–425, 1955.
- [27] C. Truesdell and W. Noll, *The Non-Linear Field Theories of Mechanics*, Springer, New York, NY, USA, 2nd edition, 1992.
- [28] J. E. Dunn and R. L. Fosdick, “Thermodynamics, stability, and boundedness of fluids of complexity 2 and fluids of second grade,” *Archive for Rational Mechanics and Analysis*, vol. 56, no. 3, pp. 191–252, 1974.
- [29] C.-C. Wang and C. Truesdell, *Introduction to Rational Elasticity*, Noordhoff International Publishing, Leyden, The Netherlands, 1973.
- [30] M. Massoudi, “On the importance of material frame-indifference and lift forces in multiphase flows,” *Chemical Engineering Science*, vol. 57, no. 17, pp. 3687–3701, 2002.
- [31] G. Gupta and M. Massoudi, “Flow of a generalized second grade fluid between heated plates,” *Acta Mechanica*, vol. 99, no. 1–4, pp. 21–33, 1993.
- [32] M. Massoudi and T. X. Phuoc, “Fully developed flow of a modified second grade fluid with temperature dependent viscosity,” *Acta Mechanica*, vol. 150, no. 1-2, pp. 23–37, 2001.
- [33] M. Massoudi and A. Vaidya, “On some generalizations of the second grade fluid model,” *Nonlinear Analysis*, vol. 9, no. 3, pp. 1169–1183, 2008.
- [34] C. S. Man and M. Massoudi, “On the thermodynamics of some generalized second-grade fluids,” *Continuum Mechanics and Thermodynamics*, vol. 22, no. 1, pp. 27–46, 2010.
- [35] K. V. Wong and O. De Leon, “Applications of nanofluids: current and future,” *Advances in Mechanical Engineering*, vol. 2010, Article ID 519659, 11 pages, 2010.
- [36] J. Fan and L. Wang, “Is classical energy equation adequate for convective heat transfer in nanofluids?” *Advances in Mechanical Engineering*, vol. 2010, Article ID 719406, 5 pages, 2010.
- [37] M. Massoudi, “A mixture theory formulation for hydraulic or pneumatic transport of solid particles,” *International Journal of Engineering Science*, vol. 48, no. 11, pp. 1440–1461, 2010.

Research Article

Natural Convection of Nanofluids in a Square Enclosure with a Protruding Heater

J. Guiet,¹ M. Reggio,^{1,2} and P. Vasseur^{1,3}

¹ *Ecole Polytechnique, Université de Montréal, C.P. 6079, Succ. "Centre Ville", Montréal, QC, Canada H3C 3A7*

² *Département de Génie Mécanique, École Polytechnique, Université de Montréal, C.P. 6079, Succ. "Centre Ville", Montréal, QC, Canada H3C 3A7*

³ *Laboratoire des Technologies Innovantes, Université de Picardie Jules Verne d'Amiens, rue des facultés, le Bailly, 80025 Amiens Cedex, France*

Correspondence should be addressed to M. Reggio, marcelo.reggio@polymtl.ca

Received 17 March 2011; Accepted 26 June 2011

Academic Editor: Yogesh Jaluria

Copyright © 2012 J. Guiet et al. This is an open access article distributed under the Creative Commons Attribution License, which permits unrestricted use, distribution, and reproduction in any medium, provided the original work is properly cited.

This paper reports a numerical study on natural convection from a protruding heater located at the bottom of a square cavity filled with a copper-water nanofluid. The vertical walls of the cavity are cooled isothermally; the horizontal ones are adiabatic, and the heater is attached to the bottom wall. The heat source is assumed either to be isothermal or to have a constant heat flux. The effective viscosity and thermal conductivity of the nanofluid are modeled according to Brinkman and Patel, respectively. Numerical solutions of the full-governing equations, based on the lattice Boltzmann method, are obtained for a wide range of the governing parameters: the Rayleigh number, Ra ; the Prandtl number, Pr ; the geometrical parameters specifying the heater; the volume fraction of nanoparticles, Φ . For a particular geometry, it has been found that, for a given Ra , heat transfer is enhanced with increasing Φ , independently of the thermal boundary condition applied on the heater.

1. Introduction

The convection of nanofluids, which are a mixture of nanoparticles in a base fluid [1], has recently been an active field of research, because of reports of greatly enhanced thermal properties. Compared with other techniques for enhancing heat transfer in practical applications, nanofluids have the advantage of behaving like pure fluids, because of the small size of nanoparticles. As a result, the possibility of using them as heat transfer fluids for various applications, such as advanced nuclear systems or microchannel and minichannel heat sinks, is currently under consideration.

A review of the literature (see, e.g., Godson et al. [2]) indicates that most studies on this topic are concerned mainly with forced convection applications, but relatively little attention has been devoted to the natural convection of nanofluids. The first study on the natural convection of a nanofluid confined in a differentially heated enclosure seems to be that of Khanafer et al. [3]. The same problem was considered by Jou and Tzeng [4]. The Khanafer et al. model was

used to investigate convective heat transfer enhancement in rectangular enclosures filled with an Al_2O_3 -water nanofluid. It was reported that increasing the buoyancy parameter and volume fraction causes an increase in the average heat transfer coefficient. Heat transfer in nanofluids by natural convection in a square cavity heated isothermally from the vertical sides has been investigated numerically by Ho et al. [5] and Santra et al. [6]. Two different formulas have been considered by Ho et al. [5], for the effective viscosity, and thermal conductivity of the nanofluids, while the Ostwald-de Waele model for a non-Newtonian shear-thinning fluid has been used by Santra et al. [6] to calculate the shear stress. It was found that the uncertainties associated with the various expressions adopted to model nanofluids have a major influence on the characteristics of heat transfer by natural convection in the enclosure. Heat transfer enhancement in a differentially heated enclosure using the variable thermal conductivity and variable viscosity of Al_2O_3 -water and Cu-water nanofluids has been investigated numerically by Abu-Nada et al. [7]. The impact of both variable viscosity and

variable thermal conductivity, derived from experimental data, has been studied. It was observed that, at high Rayleigh numbers, the Nusselt number is more sensitive to viscosity models than to thermal conductivity models. Numerical study of natural convection in partially heated rectangular enclosures has been performed by Abu-Nada et al. [8]. Different types of nanoparticles were tested. They found that the heater location affects the flow and temperature fields when nanofluids are used. The same configuration was considered recently by Ghasemi and Aminossadati [9] for the case of an oscillating heat source embedded on the vertical wall of the enclosure. Recently, Alloui et al. [10] investigated natural convection, both analytically and numerically, in a shallow rectangular cavity filled with nanofluids. The critical Rayleigh number for the onset of supercritical convection of nanofluids is predicted explicitly by these authors. Also, results are obtained from the analytical model for finite amplitude convection for which the flow and heat transfer are presented in terms of the governing parameters of the problem.

Natural convection heat transfer in partially divided cavities filled with ordinary fluids has been the subject of many studies in the past, because of its importance in many engineering fields. Applications include thermal control of electric components, nuclear reactors, and so forth. Moukalled and Acharya [11] and Moukalled and Darwish [12] numerically investigated buoyancy-induced heat transfer in partially divided trapezoidal cavities representing attic spaces. The effects of the Rayleigh number, baffle height, and baffle location on heat transfer were discussed for various thermal boundary conditions. An experimental investigation concerning laminar convection in a box, with differentially heated end walls, which is divided by a barrier into two connected chambers, was carried out by Coman et al. [13]. They found that heat transfer diminishes rapidly when the barrier is high and also that it changes little when the lateral position of the barrier varies. Oztop and Bilgen [14] studied heat transfer numerically in a differentially heated and partitioned square cavity containing heat-generating fluid. It was found that the flow field and heat transfer are modified considerably with partial dividers. Natural convection heat transfer from a protruding heater located in a triangular enclosure has been analyzed numerically by Varol et al. [15]. They reported that, in order to obtain better heat removal, the heater must be located at the center of the bottom wall. The same problem was considered by AlAmiri et al. [16] for the case of a square cavity. Their investigation revealed that, as well as location, increasing the height and width of the heater results in the enhancement of heat transfer owing to the increase in the surface area of the heater. All the above investigations are concerned only with partially divided enclosures filled with ordinary fluids. To the author's knowledge, the influence of nanofluids on this flow configuration has not yet been studied.

In our investigation here, we consider natural convection in a square enclosure with a protruding heater subjected to various thermal boundary conditions. A numerical study is carried out to predict the effect of the location and dimension of the heat source on the flow and temperature fields in

a cavity filled with a Cu-water nanofluid. The paper is organized as follows. The formulation of the problem and the numerical method are presented in Sections 2 and 3, respectively. In Section 4, the results obtained for the flow and heat transfer are discussed in terms of the geometry of the system. The final last section presents some concluding remarks related to optimum heat transfer enhancement based on the nanoparticle volume fraction, the length and the width of the enclosure, the Rayleigh number, and the location of the protruding heater.

2. Mathematical Formulation

Figure 1(a) schematically represents the flow configuration with a coordinate system. The square enclosure is of height H' . The vertical walls of the enclosure are cooled isothermally, at temperature T'_c , while the horizontal walls are adiabatic. A protruding heater of height l' and width w' is placed at a distance d' from the left wall, as shown in the graph. The cavity is filled with Newtonian, incompressible nanofluid. The thermophysical properties of the mixture considered in this study are assumed constant, except for the density variation, which is determined based on the Boussinesq approximation. Also, it is supposed that the base fluid and the nanoparticles are in thermal equilibrium and that no slip occurs between them.

The governing macroscopic equations that describe the system behavior are those of conservation of mass, momentum, and energy, which are given as

$$\begin{aligned} \frac{\partial^2 \Psi'}{\partial x'^2} + \frac{\partial^2 \Psi'}{\partial y'^2} &= -\omega', \\ \frac{\partial \omega'}{\partial t'} + u' \frac{\partial \omega'}{\partial x'} + v' \frac{\partial \omega'}{\partial y'} &= \frac{1}{\rho_{nf}} \left[\mu_{nf} \left(\frac{\partial^2 \omega'}{\partial x'^2} + \frac{\partial^2 \omega'}{\partial y'^2} \right) + (\rho \beta')_{nf} g \frac{\partial T'}{\partial x'} \right], \\ \frac{\partial T'}{\partial t'} + u' \frac{\partial T'}{\partial x'} + v' \frac{\partial T'}{\partial y'} &= \alpha_{nf} \left(\frac{\partial^2 T'}{\partial x'^2} + \frac{\partial^2 T'}{\partial y'^2} \right), \end{aligned} \quad (1)$$

in terms of stream function Ψ' , vorticity ω' , and temperature T' . As usual, in order to satisfy the continuity equation, the stream function Ψ' is defined such that $u' = \partial \Psi' / \partial y'$, $v' = -\partial \Psi' / \partial x'$.

The appropriate boundary conditions applied on the walls of the cavity are

$$\begin{aligned} x' = 0, H', \quad 0 \leq y' \leq H', \\ \Psi' = \frac{\partial \Psi'}{\partial x'} = 0, \quad \omega' = -\frac{\partial^2 \Psi'}{\partial x'^2}, \quad T' = T'_c, \\ y' = H', \quad 0 \leq x' \leq H', \\ \Psi' = \frac{\partial \Psi'}{\partial y'} = 0, \quad \omega' = -\frac{\partial^2 \Psi'}{\partial y'^2}, \quad \frac{\partial T'}{\partial y'} = 0, \end{aligned}$$

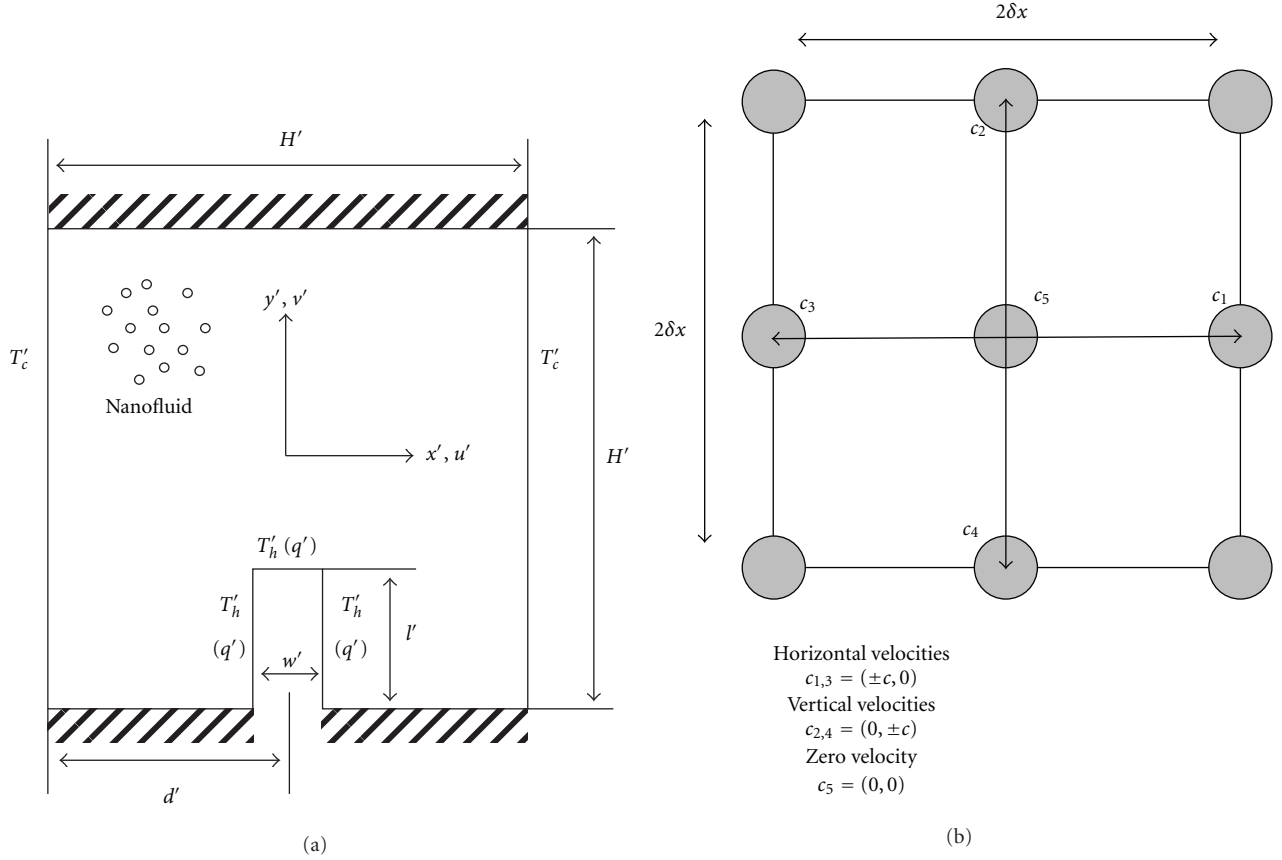


FIGURE 1: (a) Schematic diagram for physical model with coordinate system. (b) Diagram of the discrete D2Q5 phase space.

$$y' = 0 \begin{cases} 0 \leq x' \leq d' - \frac{w'}{2} \\ d' + \frac{w'}{2} \leq x' \leq H', \end{cases}$$

$$\Psi' = \frac{\partial \Psi'}{\partial y'} = 0, \quad \omega' = -\frac{\partial^2 \Psi'}{\partial y'^2}, \quad \frac{\partial T'}{\partial y'} = 0. \quad (2)$$

On the heater walls, the hydrodynamic boundary conditions are given by

$$\Psi' = \frac{\partial \Psi'}{\partial n'} = 0, \quad \omega' = -\frac{\partial^2 \Psi'}{\partial n'^2}, \quad (3)$$

while the two following thermal boundary conditions are considered:

- (1) a constant temperature T'_h , such that

$$T' = T'_h, \quad (4)$$

- (2) a constant heat flux q' , such that

$$\frac{\partial T'}{\partial n'} = -\frac{q'}{k_{nf}}. \quad (5)$$

In these equations, n' represents the normal to the heater walls, and the constant k_{nf} is the characteristic thermal conductivity of the fluid considered.

The effective density of the nanofluid is given as

$$\rho_{nf} = (1 - \Phi)\rho_f + \Phi\rho_{np}, \quad (6)$$

where Φ is the solid volume fraction of nanoparticles.

The thermal diffusivity of the nanofluid is

$$\alpha_{nf} = \frac{k_{nf}}{(\rho C_P)_{nf}}, \quad (7)$$

where the heat capacitance of the nanofluid is given by

$$(\rho C_P)_{nf} = (1 - \Phi)(\rho C_P)_f + \Phi(\rho C_P)_{np}. \quad (8)$$

The thermal expansion coefficient of the nanofluid can be determined by:

$$(\rho\beta')_{nf} = (1 - \Phi)(\rho\beta')_f + \Phi(\rho\beta')_{np}. \quad (9)$$

The effective dynamic viscosity of the nanofluid is calculated using Brinkman's model [17] as follows:

$$\mu_{nf} = \frac{\mu_f}{(1 - \Phi)^{2.5}}, \quad (10)$$

which gives an estimation of the viscosity of a nanofluid containing a dilute suspension of small, rigid, spherical particles.

The thermal conductivity of the nanofluid is calculated using a model proposed by Patel et al. [18] as follows:

$$\frac{k_{nf}}{k_f} = 1 + \frac{k_{np}A_{np}}{k_f A_f} + ck_{np}Pe \frac{A_{np}}{k_f A_f}, \quad (11)$$

where $c = 25000$ is a constant determined experimentally, and A_{np}/A_f is defined as

$$\frac{A_{np}}{A_f} = \frac{d_f}{d_{np}} \frac{\Phi}{(1 - \Phi)}, \quad (12)$$

with d_{np} being the diameter of the solid nanoparticles in the fluid, assumed here to be equal to $d_{np} = 100$ nm, and $d_f = 2 \text{ \AA}$ being the size of the liquid molecules, namely, those of water.

The Péclet number in (11) is defined as

$$Pe = \frac{u_{np}d_{np}}{\alpha_f}, \quad (13)$$

with u_{np} expressing the Brownian motion velocity of nanoparticle, defined as

$$u_{np} = \frac{2k_b T'}{\pi\mu_f d_{np}^2}, \quad (14)$$

where $k_b = 1.38065 \times 10^{-23}$ is the Boltzmann constant.

The governing equations with the above models are made dimensionless by scaling the length by H' and the velocity by $\alpha_f Ra^{1/2}/H'$, with α_f being the thermal diffusivity of pure fluid, and time by $H'^2/\alpha_f Ra^{1/2}$. Also, we introduce the reduced temperature $T = (T' - T'_0)/\Delta T'$, where $\Delta T' = (T'_h - T'_c)$ for an isothermal heater and $\Delta T' = q'H'/k_f$ for a heater with a constant heat flux. The wall temperature of the enclosure is set arbitrarily to $T'_0 = 22^\circ\text{C}$, and the characteristic temperature difference is fixed to $\Delta T' = 30^\circ\text{C}$.

The dimensionless equations governing the present problem then read

$$\frac{\partial^2 \Psi}{\partial x^2} + \frac{\partial^2 \Psi}{\partial y^2} = -\omega, \quad (15)$$

$$\frac{\partial \omega}{\partial t} + u \frac{\partial \omega}{\partial x} + v \frac{\partial \omega}{\partial y} = \bar{\nu} \frac{\text{Pr}}{\text{Ra}^{1/2}} \left(\frac{\partial^2 \omega}{\partial x^2} + \frac{\partial^2 \omega}{\partial y^2} \right) + \bar{\beta} \text{Pr} \frac{\partial T}{\partial x}, \quad (16)$$

$$\frac{\partial T}{\partial t} + u \frac{\partial T}{\partial x} + v \frac{\partial T}{\partial y} = \frac{\bar{\alpha}}{\text{Ra}^{1/2}} \left(\frac{\partial^2 T}{\partial x^2} + \frac{\partial^2 T}{\partial y^2} \right), \quad (17)$$

where

$$\bar{\nu} = \frac{\nu_{nf}}{\nu_f}, \quad \bar{\beta} = \frac{(\rho\beta')_{nf}}{(\rho_{nf}\beta'_f)}, \quad \bar{\alpha} = \frac{\alpha_{nf}}{\alpha_f}. \quad (18)$$

The corresponding boundary conditions are

$$\begin{aligned} x = 0, 1, \quad 0 \leq y \leq 1, \\ \Psi = \frac{\partial \Psi}{\partial x} = 0, \quad \omega = -\frac{\partial^2 \Psi}{\partial x^2}, \quad T = 0, \\ y = 1, \quad 0 \leq x \leq 1, \\ \Psi = \frac{\partial \Psi}{\partial y} = 0, \quad \omega = -\frac{\partial^2 \Psi}{\partial y^2}, \quad \frac{\partial T}{\partial y} = 0, \\ y = 0 \quad \begin{cases} 0 \leq x \leq D - \frac{W}{2} \\ D + \frac{W}{2} \leq x \leq 1, \end{cases} \\ \Psi = \frac{\partial \Psi}{\partial y} = 0, \quad \omega = -\frac{\partial^2 \Psi}{\partial y^2}, \quad \frac{\partial T}{\partial y} = 0, \end{aligned} \quad (19)$$

and the no slip condition on the heater wall yields

$$\Psi = \frac{\partial \Psi}{\partial n} = 0, \quad \omega = -\frac{\partial^2 \Psi}{\partial n^2}, \quad (20)$$

while the dimensionless thermal boundary conditions are as follows:

$$(1) \text{ the constant temperature applied on the heater} \quad T = 1 \quad (21)$$

(2) the constant heat flux on the heater

$$\frac{\partial T}{\partial n} = -\frac{k_f}{k_{nf}}. \quad (22)$$

The heat transfer rates along the vertical walls are expressed in terms of the local and average Nusselt's numbers Nu and \bar{Nu} , respectively. Depending on the thermal boundary conditions applied on the heater, these parameters are computed as follows:

(3) on the left vertical wall of the heater for a constant temperature,

$$Nu = -\frac{k_{nf}}{k_f} \frac{\partial T}{\partial x} \Big|_{x=0}, \quad (23)$$

$$\bar{Nu} = \int_0^1 Nu \, dy, \quad (24)$$

(4) on the heater for a constant heat flux,

$$Nu = \frac{1}{T} \Big|_{\text{heater}}, \quad (25)$$

$$\bar{Nu} = \frac{\int_{\text{Heater}} Nu \, dl}{\int_{\text{Heater}} dl}, \quad (26)$$

with dl representing an elementary length along the walls of the heater.

From the above equations, we can see that the present problem is governed by six dimensionless parameters, namely, the thermal Rayleigh number $Ra = g\beta'_f \Delta T' H'^3 / \alpha_f \nu_f$, the Prandtl number $Pr = \nu_f / \alpha_f$, the solid volume fraction of nanoparticles Φ , and the geometrical parameters for the heater, that is, $L = (l'/H')$, $W = (w'/H')$, and $D = (d'/H')$. Naturally, the type of nanoparticles considered must also be specified, which introduces another parameter.

3. Numerical Solution

The solution of the governing equations, (15) to (17), is obtained using the lattice Boltzmann method (LBM). The LBM, developed two decades ago, examines fluids in the molecular state instead of at the classical macroscopic level and makes it possible to simulate flows by solving the Boltzmann transport equation for particle distribution functions on a simplified phase space, called the lattice [19, 20].

In this study, we used the LBM to solve the stream function, vorticity, and temperature equations, instead of the classical Navier-Stokes equations for velocity and temperature. This approach, recently proposed by Chai and Shi [21] and Chen et al. [22, 23], enables us to solve the advection-diffusion equations, (16) and (17), and the Poisson equation, (15), using particle distribution functions and applying the lattice Boltzmann approach on the D2Q5-phase space described in Figure 1(b).

We considered three sets of particle distribution functions. One set describes the temperature T and another the vorticity ω , both of them evolving following the collision and propagation steps described by Chen et al. [22, 23]. The third set of particle distribution functions is used for the stream function Ψ and is computed by iterating the collision and propagation steps, as described by Chai and Shi [21].

The parameters characterizing the nanofluid, that is, to say thermal diffusivity $\bar{\alpha}$, kinematic viscosity $\bar{\nu}$, and thermal expansion coefficient $\bar{\beta}$, are introduced in the model with the definition of characteristic relaxation times. These characteristic parameters, which make it possible to link the macroscopic formulation of the Navier-Stokes equations to the mesoscopic formulation of the LBM, were modified to take into account the influence of the nanoparticles on the fluid in the LBM framework for the various models studied (see e.g., Guet et al. [24]).

With the present approach, a wide range of simulations were conducted for the simulation of natural convection in partially divided square enclosures. For these simulations, the convergence was considered to be reached when the relative error on variables $V = \Psi$, ω , and T between two successive iterations, t and $t + 1$, was smaller than a chosen tolerance:

$$ERR_V = \frac{\sum_x \sum_y |V_{x,y}^{t+1} - V_{x,y}^t|}{\sum_x \sum_y |V_{x,y}^{t+1}|} < 10^{-6}. \quad (27)$$

The calculations were performed on 101×101 regular grids using D2Q5 lattices, this refinement being a good compromise between computational time and accuracy.

To check the ability of this LBM formulation to simulate flows in partially divided cavities, various simulations were conducted for pure fluid and compared with results provided by AlAmiri et al. [16]. The accuracy of the LBM was checked for various Rayleigh's numbers, Ra , in different configurations with various heights L , widths W , and positions D of an isothermal heater. The results are summarized in Table 1. Good agreement is observed, with the maximum deviation being of the order of 1.7% for the 101×101 grid. We can note that, while increasing Ra , the stream function amplitude $\Psi_{\max} - \Psi_{\min}$ reaches a maximum at $Ra = 10^5$ and then decreases. This can be explained by the fact that, increasing $Ra < 10^5$, the conduction is not negligible compared to the convection; the presence of the heater affects more and more fluid in the cavity (by conduction) inducing a convection of more and more fluid in the cavity. A maximum is reached where all the fluid in the cavity is convected. Then, increasing Ra , the conduction becomes negligible, and the convection occurs more and more close from the vertical walls (cooled fluid) and above the heater (warmed fluid), leaving larger areas of the cavity where the fluid is not affected by the convection. The stream function amplitude $\Psi_{\max} - \Psi_{\min}$ tends to reduce ($Ra > 10^5$).

4. Results and Discussion

The results presented in this paper were obtained for pure fluid and a copper (Cu)-water mixture. The thermophysical properties of the base fluid, that is, water, and the nanoparticles, are reported in Table 2. Since this study is limited to water-based solutions, it is assumed that the Prandtl number (Pr) equals 7. As discussed by many authors (see, e.g., Trevisan and Bejan [25]), this type of convective heat transfer is independent of this parameter, provided that this latter is of order one or greater. The results are presented for Rayleigh's numbers varying from 10^3 to 10^6 , for various geometries, $0.25 \leq L \leq 0.8$, $0.1 \leq W \leq 0.8$, and positions, $0.15 \leq D \leq 0.5$, of the heater, while the nanoparticle volume fraction covers the $0 \leq \Phi \leq 0.05$ range.

Typical numerical results are presented in Figure 2 for $Ra = 10^5$, $D = 0.5$, and $W = 0.2$. On the graphs, streamlines and isotherms are presented from left to right. The calculated maximum stream functions ($|\Psi_{\max}|$) and heat transfer (\overline{Nu}) are also given with each graph for reference. In these figures, the streamlines are equally spaced between $\Psi = 0$ on the boundaries and the maximum (minimum) value Ψ_{\max} (Ψ_{\min}). Also, the isotherms are equally spaced between $T_{\max} = 1$ and $T_{\min} = 0$. Figure 2(a) shows the results obtained for a cavity with a protruding isothermal heater of height $L = 0.25$, filled with a pure solution ($\Phi = 0$). The resulting flow and temperature fields are similar to those reported in the literature in the past (see, e.g., AlAmiri et al. [16]). Since the heater is centrally located in the middle of the bottom wall ($D = 0.5$), symmetrical flow and temperature patterns, about a vertical line passing

TABLE 1: Comparison with results provided by Alimiri et al. [16] of the stream function extremes (Ψ_{\min}, Ψ_{\max}) for various heat source configurations ($Pr = 0.71$).

Ra	W	L	D	Reference [16]	Present	Difference
10^4	0.2	0.25	0.5	(-0.0333, 0.0333)	(-0.0330, 0.0330)	0.9%
10^5	0.2	0.25	0.5	(-0.0459, 0.0459)	(-0.0458, 0.0458)	0.22%
10^6	0.2	0.25	0.5	(-0.0290, 0.0290)	(-0.0289, 0.0289)	0.34%
10^6	0.1	0.25	0.5	(-0.0292, 0.0292)	(-0.0291, 0.0291)	0.34%
10^6	0.4	0.25	0.5	(-0.0299, 0.0299)	(-0.0299, 0.0299)	0%
10^6	0.2	0.05	0.5	(-0.0331, 0.0331)	(-0.0330, 0.0330)	0.34%
10^6	0.2	0.5	0.5	(-0.0239, 0.0239)	(-0.0235, 0.0235)	1.7%
10^6	0.2	0.25	0.2	(-0.0334, 0.0288)	(-0.0328, 0.0286)	1.3%

TABLE 2: Thermophysical properties of water and Cu-nanoparticles [8].

	ρ (kg m^{-3})	C_p ($\text{J kg}^{-1} \text{K}^{-1}$)	k ($\text{Wm}^{-1} \text{K}^{-1}$)	$\beta \times 10^5$ (K^{-1})
H ₂ O	997.1	4179	0.613	21
Cu	8933	385	401	1.67

through the axis of symmetry of the heated element, are observed in the enclosure. The streamlines are seen to occupy the entire cavity body. The field of isotherms indicates that these are mostly parallel to the heated and cooled boundaries, except above the heated element. As the solid volume fraction is increased to $\Phi = 0.05$, the resulting streamlines and isotherms are depicted as in Figure 2(b). It is found that, as expected, the flow and temperature patterns are influenced by the addition of nanoparticles, which enhances the buoyancy forces, owing to the increase in the effective thermal conductivity of the mixture. As a result, the strength of convective heat transfer is improved with an increase in solid concentration. In fact, the increase in the Nusselt number is about 33.5% for a concentration of nanoparticles as low as $\Phi = 0.05$. Figure 2(c) shows the results obtained when the heater height is increased to $L = 0.50$ for $\Phi = 0.05$. A comparison between Figures 2(b) and 2(c) indicates that, as the height of the heater increases, the intensity of the convective motion diminishes, as indicated by the values of the maximum and minimum stream function patterns. This is because an increase in the length of the heated element results in an increase in resistance to the flow. However, the average Nusselt-number is found to be enhanced from $\overline{Nu} = 4.356$ to $\overline{Nu} = 5.839$ as the heater height is increased from $L = 0.25$ to $L = 0.50$. Similar data were obtained for the same conditions, but for the case of a block heated by a constant heat flux. The obtained results (not presented here) indicate that the streamline patterns were qualitatively similar to those reported for the isothermal heater. Naturally, the isotherm patterns are quite different, especially in the vicinity of the heater, where the surface temperature of this latter is not constant.

Figure 3 illustrates the variation in \overline{Nu} with the solid volume fraction Φ at various Rayleigh's numbers. The specific geometrical configuration of the heating source

considered is $D = 0.5$, $L = 0.25$, and $W = 0.2$. The results obtained for the isothermal heater and the constant heat flux heater are depicted in Figures 3(a) and 3(b), respectively. In general, past studies on this topic have demonstrated that the addition of nanoparticles to a base fluid leads to the occurrence of two opposing effects on the convective heat transfer within the cavity. The first effect, resulting from the enhanced thermal conductivity of the mixture owing to the presence of the nanoparticles, improves \overline{Nu} . The second effect, owing to the increase in viscosity caused by the addition of nanoparticles, eliminates the convective motion and thus reduces \overline{Nu} . Which of these two antagonist mechanisms prevails depends on the type of particles used, the convection intensity (Ra), and the models considered to approximate the viscosity and thermal conductivity of the mixture. In this study, the results depicted in Figure 3 show that, for a given Ra value, a monotonic increase in \overline{Nu} is obtained with the addition of nanoparticles. For the isothermal heater, Figure 3(a) indicates that, at $\Phi = 0.05$, the Nusselt number is enhanced by about 38% for $Ra = 10^3$ and by about 32% for $Ra = 10^6$. The case of a constant heat flux heater, Figure 3(b), is discussed next. For this situation, the temperatures of the surface of the heater, T , are not constant. As a matter of fact, its maximum value, T_{\max} , is an important parameter in the thermal design of electronic devices. For a given value of Φ , Figure 3(b) shows that increasing monotonically Ra enhances \overline{Nu} . This follows from the fact that increasing the Rayleigh number enhances convection, that is, heat removal from the heater. As a result, the temperatures on the surface of the heated element are reduced, resulting in an enhancement of the heat transfer. Specifically, it is found that, at $\Phi = 0.05$, the Nusselt number is enhanced by about 36% for $Ra = 10^3$ and by about 22% for $Ra = 10^6$. Note that in that case the computed average Nusselt numbers for $Ra = 10^3$ and 10^4 are almost identical. This is due to the weak impact of natural convection on the heat transfer for these two cases, the heat exchange being due to conduction. The impact of the convection starts appearing for the simulations at $Ra = 10^5$.

This result indicates that the cooling performance of nanofluids is more effective at low Rayleigh's numbers than at

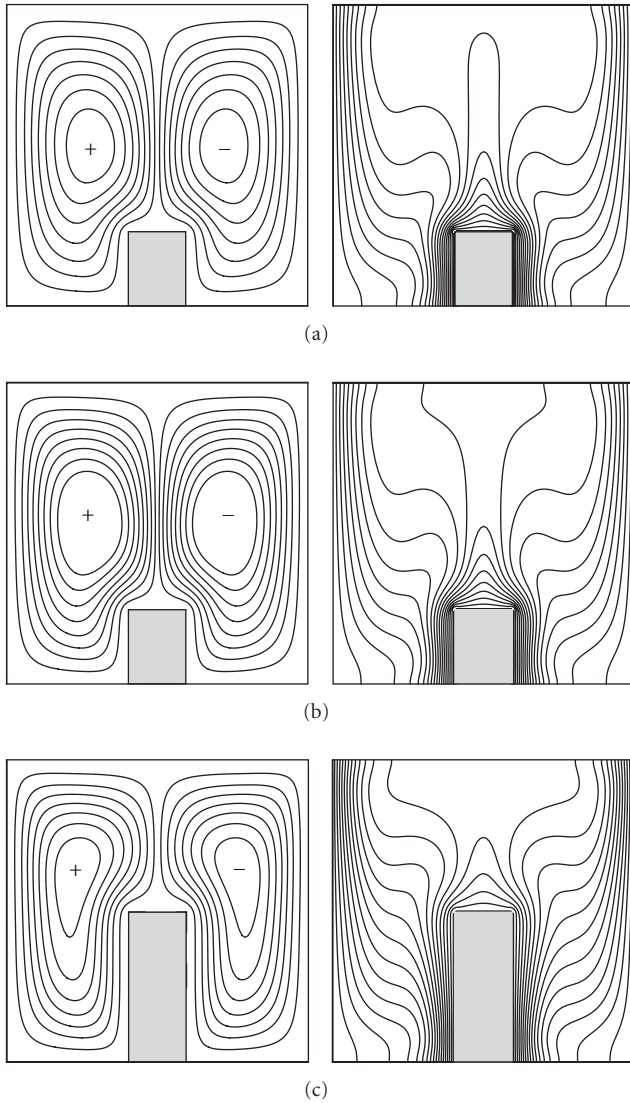
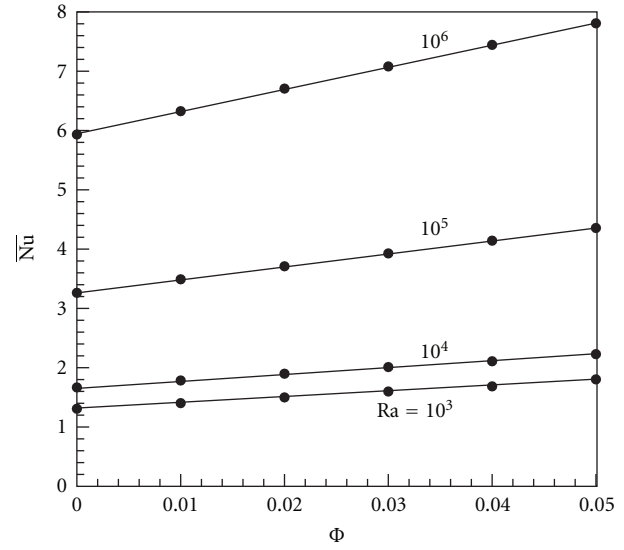
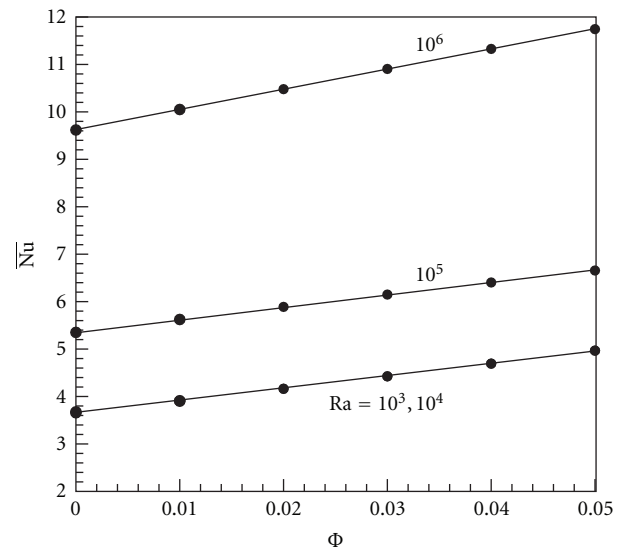


FIGURE 2: Effect of varying the ratio of nanoparticles, Φ , and the length, L , of an isothermally heated heater on the streamlines (left) and isotherms (right) for $Ra = 10^5$, $D = 0.5$, $W = 0.2$, and (a) $L = 0.25$ and $\Phi = 0$: $|\Psi_{\max}| = 0.0391$, $\overline{Nu} = 3.264$, (b) $L = 0.25$ and $\Phi = 0.05$: $|\Psi_{\max}| = 0.0506$, $\overline{Nu} = 4.356$, (c) $L = 0.50$ and $\Phi = 0.05$: $|\Psi_{\max}| = 0.0392$, $\overline{Nu} = 5.839$.

high ones, independently of the heating conditions imposed on the heater. This behavior of \overline{Nu} with Φ is in good agreement with the results reported in previous studies, especially when the Rayleigh number is small enough that convection is weak ($Ra \leq 10^4$). For this situation, for which heat transfer by conduction prevails, the increase in \overline{Nu} with Φ is due to the enhancement in thermal conductivity of the nanofluid. This trend has been found to be independent of the models used to characterize the mixture. It must be mentioned that a review of the literature indicates that, at higher Ra values for which heat transfer is dominated by convection, the effects of the nanoparticle volume fraction on the Nusselt number was found to be either beneficial or detrimental, depending on the formulas adopted to model



(a)



(b)

FIGURE 3: Variation of the average Nusselt number \overline{Nu} with solid volume fraction Φ at various Rayleigh's number's Ra for $D = 0.5$, $L = 0.25$, $W = 0.2$, and for, (a) isothermal heater; (b) heater with a constant heat flux.

the effective thermal conductivity and dynamic viscosity of the nanofluid.

Figure 4 illustrates the variation of \overline{Nu} for $Ra = 10^5$, in terms of the geometry and position of the heat source and Φ of the mixture, for a heater with a constant heat flux. Figures 4(a) and 4(b) show the variation of \overline{Nu} with the height L of the heated element. It can be seen that, for a given solid volume fraction, the Nusselt number decreases as the height increases. This follows from the fact that the temperature at the surface of the element increases as the height of the element increases, owing to the higher heat flux generated by the heat source. The influence of the heater width W on \overline{Nu} is presented in Figure 4(b). For a given Φ , it is found

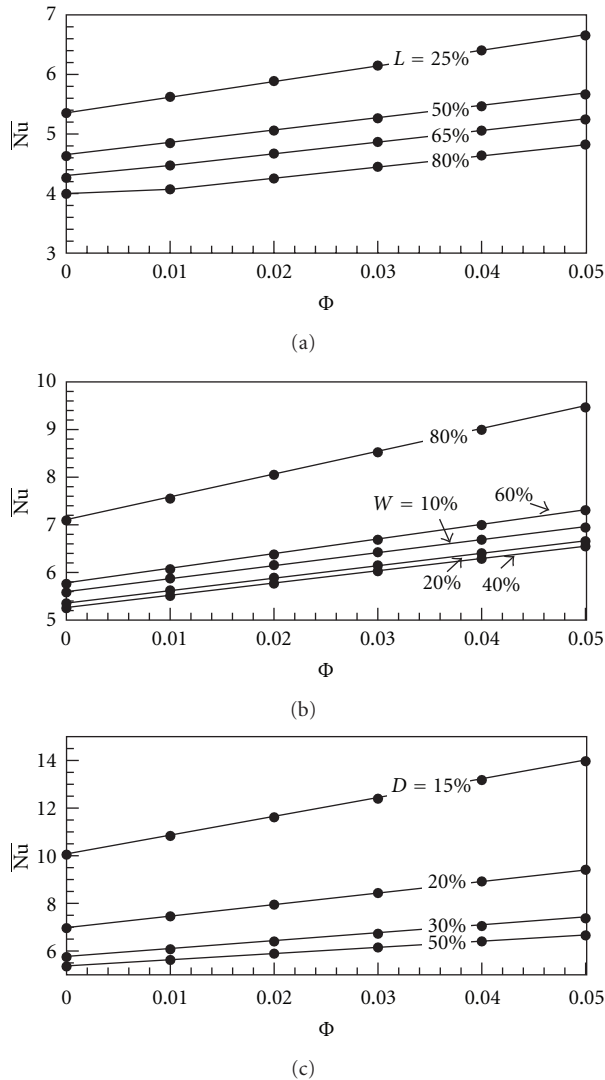


FIGURE 4: Variation of the average Nusselt number \overline{Nu} , for the case of a heater with a constant heat flux, with solid volume fraction Φ for $Ra = 10^5$: (a) effect of the heater height L for $D = 0.5$ and $W = 0.2$; (b) effect of the heater width W for $D = 0.5$ and $L = 0.25$; (c) effect of the heater position D for $L = 0.25$ and $W = 0.2$.

that, as the width of the heater increases from $W = 0.10$ to $W = 0.80$, the Nusselt number first decreases to reach a minimum at about $W = 0.40$. Above this value, \overline{Nu} is found to increase sharply with W . Concerning the influence of Φ , Figure 4(a) indicates that, with an increase of 5% in this parameter, the Nusselt number grows by about 24% at $L = 0.25$ and by about 21% at $L = 0.80$. Similarly, it is observed from Figure 4(b) that \overline{Nu} improves by 24% at $W = 0.10$ and 33% at $W = 0.80$. Figure 4(c) presents the effect of the location of the heat source D on \overline{Nu} . Independently of the concentration Φ of the solution, the average Nusselt number is minimum for $D = 0.50$, that is, when the heater is centrally located at the bottom of the enclosure. Naturally, symmetrical flow and temperature patterns are generated in the enclosure in this case (Figure 5(a)). As the

heat source moves towards the left vertical isothermal wall ($D < 0.5$), the flow patterns consist of two nonsymmetrical counterrotating cells of unequal strengths (Figures 5(b) and 5(c)). The isotherm patterns indicate that, as the heater is moved to the left cold wall, the temperature of the heat source, which is not uniform since it is heated by a constant heat flux, decreases. Moving the heat source to the vicinity of the cooled boundary enhances heat removal considerably, which reduces the temperatures on the surface of the heater. As a result, the average Nusselt number increases sharply as it moves away from the central position, $D = 0.50$. Also, Figure 4(c) shows that the average Nusselt number increases monotonically with the solid volume, independently of the position of the heater. With an increase of 5% in solid volume fraction, the Nusselt number grows by about 40% at $D = 0.15$ and by about 24% at $D = 0.5$.

Figure 6 illustrates the results obtained for the same conditions as those of Figure 4, but for the case of an isothermal heater. A bird's eye view of the graphs indicates that, independently of the geometry and position of the heat source, the Nusselt number increases with an increase in the volume fraction Φ , that is, the thermal conductivity of the solution. Thus, as expected, this behavior is independent of the thermal boundary conditions applied on the heat source. The effect of the size of the heater on heat transfer is shown in Figures 6(a) and 6(b), which indicate that \overline{Nu} improves with an increase in the dimensions of the heating surface. The fact that the average Nusselt number improves with an increase in the height and width of an isothermal heater located at the bottom of a cavity has already been reported by AlAmiri et al. [16] for pure fluid. The influence of the position D of the block heater on the heat transfer is depicted in Figure 6(c). Qualitatively, the results are similar to those reported for the case of the block when heated by a constant heat flux (Figure 4(c)). Quantitatively, Figure 6(c) indicates that, when Φ increases from 0 to 5%, the Nusselt number grows by about 35% at $D = 0.15$ and by about 33% at $D = 0.5$.

5. Conclusions

In this paper, a numerical study of natural convection heat transfer in a square enclosure filled with a suspension of copper-water nanofluid is carried out. The simulations were performed using the lattice Boltzmann approach. The system is heated, by a protruding heater located at the bottom of the system, and cooled isothermally from the two vertical walls. The heater is assumed either to be isothermal or to generate a constant heat flux. The governing parameters of the problem are the thermal Rayleigh number, Ra , the solid volume fraction of nanoparticles, Φ , the size (L and W) of the heater and its position, D . The main conclusions of the present analysis are as follows.

- (1) In the range of the governing parameters considered in this study, for a given geometry and position of the heater, the heat transfer is improved by enhancing both the Rayleigh number and the nanoparticle volume fraction.

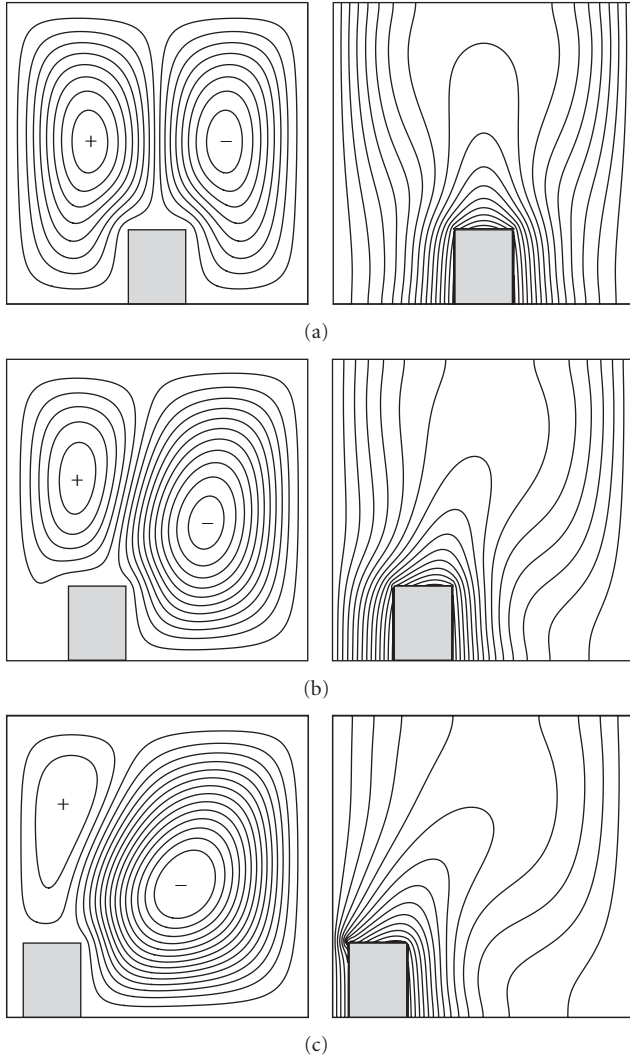


FIGURE 5: Effect of varying the position D of the constant heat flux heater on the streamlines (left) and isotherms (right) for $Ra = 10^5$, $\Phi = 0.05$, $L = 0.25$, $W = 0.2$ and: (a) $D = 0.50$: $\Psi_{\max} = 0.0153$, $\Psi_{\min} = -0.0153$, $T_{\max} = 0.1677$, $\bar{Nu} = 6.6556$; (b) $D = 0.30$: $\Psi_{\max} = 0.0092$, $\Psi_{\min} = -0.0190$, $T_{\max} = 0.1526$, $\bar{Nu} = 7.3719$; (c) $D = 0.15$: $\Psi_{\max} = 0.0036$, $\Psi_{\min} = -0.0199$, $T_{\max} = 0.1476$, $\bar{Nu} = 13.9672$.

- (2) For the case of an isothermal heater, the numerical results indicate that, for a given solid volume fraction of nanoparticles, the heat transfer is improved when the size of the heating source increases. Also, the average Nusselt number is enhanced as the position of the heating block is moved from the center position toward the vertical isothermal boundaries of the enclosure.
- (3) For the case of a heater with a constant heat source, for a given Rayleigh number and solid volume fraction of nanoparticles, the increase in the height of the heater results in a rise in the maximum surface temperature of the element. Consequently, the average Nusselt number decreases with the increase

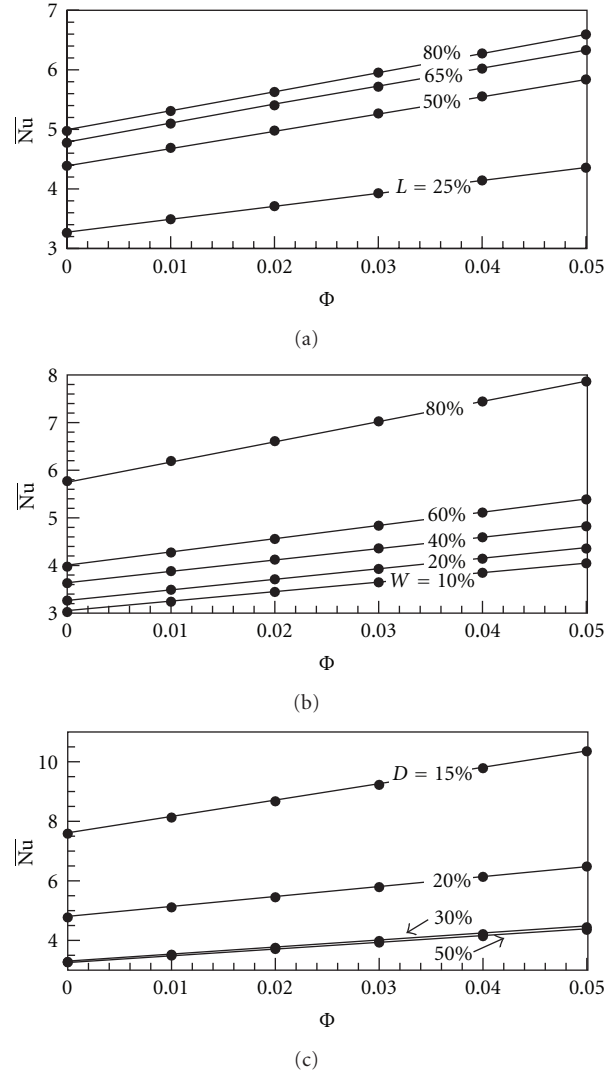


FIGURE 6: Variation of the average Nusselt number \bar{Nu} (computed on the left vertical wall), for an isothermal heater, with solid volume fraction Φ for $Ra = 10^5$: (a) effect of the heater height L for $D = 0.5$ and $W = 0.2$; (b) effect of the heater width W for $D = 0.5$ and $L = 0.25$; (c) effect of the heater position D for $L = 0.25$ and $W = 0.2$.

in the height of the heat source. The influence of the width, W , on \bar{Nu} is more complex. When it increases from $W = 0.1$, \bar{Nu} first decreases to reach a minimum at $W \approx 0.4$, above which the heat transfer increases monotonically with W . As in the case of the isothermal heater, as the position D of the heating block is moved from the center of the bottom wall of the cavity towards the left (right) vertical cooled wall, the maximum temperature of the element decreases, which improves \bar{Nu} .

Nomenclature

- C_p : Heat capacitance
- D : Dimensionless location of the heater (d'/H')

d' : Distance of the heat element from the left wall
 d_{np} : Diameter of a solid nanoparticle
 d_f : Diameter of a liquid molecule
 g : Gravitational acceleration
 H' : Height of cavity
 k : Thermal conductivity
 k_b : Boltzmann's constant ($k_b = 1.38065 \times 10^{-23}$)
 L : Dimensionless height of the heater (l'/H')
 l' : Height of the heater
 Nu : Nusselt number (23) and(25)
 \bar{Nu} : Average Nusselt number (24) and(26)
 Pe : Péclet number, ($u_{np}d_{np}/\alpha_f$)
 Pr : Prandtl number of pure fluid (ν_f/α_f)
 q' : Constant heat flux per unit area
 Ra : Thermal Rayleigh number ($g\beta'_f\Delta T'H'^3/\alpha_f\nu_f$)
 t : Dimensionless time ($t'\alpha_f Ra^{1/2}/H'^2$)
 T : Dimensionless temperature ($(T' - T'_0)/\Delta T'$)
 T'_0 : Reference temperature
 u : Dimensionless velocity in x direction ($u'H'/\alpha_f Ra^{1/2}$)
 u_{np} : Brownian motion velocity of nanoparticles
 v : Dimensionless velocity in y direction ($v'H'/\alpha_f Ra^{1/2}$)
 W : Dimensionless width of the heater (w'/H')
 w' : Width of the heater
 x : Dimensionless coordinate axis (x'/H')
 y : Dimensionless coordinate axis (y'/H').

Greek Symbols

α : Thermal diffusivity
 $\bar{\alpha}$: Dimensionless parameter (α_{nf}/α_f)
 β' : Thermal expansion coefficient
 $\bar{\beta}$: Dimensionless parameter ($(\rho\beta')_{nf}/(\rho\beta')_f$)
 ν : Kinematic viscosity of fluid
 $\bar{\nu}$: Dimensionless parameter (ν_{nf}/ν_f)
 ρ : Density of fluid
 Φ : Nanoparticle volume fraction
 Ψ : Dimensionless stream function ($\Psi'/\alpha_f Ra^{1/2}$)
 ω : Dimensionless vorticity ($\omega'/\alpha_f Ra^{1/2}$).

Subscript

0 : Reference state
 f : Pure fluid
 max : Maximum values
 min : Minimum values
 nf : Nanofluid
 np : Nanoparticle.

Superscript

' : It refers to a dimensional variable.

References

- [1] S. U. S. Choi, "Enhancing thermal conductivity of fluids with nanoparticles," *Flow*, vol. 66, pp. 99–105, 1995.
- [2] L. Godson, B. Raja, D. Mohan Lal, and S. Wongwises, "Enhancement of heat transfer using nanofluids—an overview," *Renewable and Sustainable Energy Reviews*, vol. 14, no. 2, pp. 629–641, 2010.
- [3] K. Khanafer, K. Vafai, and M. Lightstone, "Buoyancy-driven heat transfer enhancement in a two-dimensional enclosure utilizing nanofluids," *International Journal of Heat and Mass Transfer*, vol. 46, no. 19, pp. 3639–3653, 2003.
- [4] R. Y. Jou and S. C. Tzeng, "Numerical research of nature convective heat transfer enhancement filled with nanofluids in rectangular enclosures," *International Communications in Heat and Mass Transfer*, vol. 33, no. 6, pp. 727–736, 2006.
- [5] C. J. Ho, M. W. Chen, and Z. W. Li, "Numerical simulation of natural convection of nanofluid in a square enclosure: effects due to uncertainties of viscosity and thermal conductivity," *International Journal of Heat and Mass Transfer*, vol. 51, no. 17-18, pp. 4506–4516, 2008.
- [6] A. K. Santra, S. Sen, and N. Chakraborty, "Study of heat transfer augmentation in a differentially heated square cavity using copper-water nanofluid," *International Journal of Thermal Sciences*, vol. 47, no. 9, pp. 1113–1122, 2008.
- [7] E. Abu-Nada, Z. Masoud, H. F. Oztop, and A. Campo, "Effect of nanofluid variable properties on natural convection in enclosures," *International Journal of Thermal Sciences*, vol. 49, no. 3, pp. 479–491, 2010.
- [8] E. Abu-Nada, Z. Masoud, and A. Hijazi, "Natural convection heat transfer enhancement in horizontal concentric annuli using nanofluids," *International Communications in Heat and Mass Transfer*, vol. 35, no. 5, pp. 657–665, 2008.
- [9] B. Ghasemi and S. M. Aminossadati, "Periodic natural convection in a nanofluid-filled enclosure with oscillating heat flux," *International Journal of Thermal Sciences*, vol. 49, no. 1, pp. 1–9, 2010.
- [10] Z. Alloui, P. Vasseur, and M. Reggio, "Natural convection of nanofluids in a shallow cavity heated from below," *International Journal of Thermal Sciences*, vol. 50, no. 3, pp. 385–393, 2011.
- [11] F. Moukalled and S. Acharya, "Buoyancy-induced heat transfer in partially divided trapezoidal cavities," *Numerical Heat Transfer; Part A*, vol. 32, no. 8, pp. 787–810, 1997.
- [12] F. Moukalled and M. Darwish, "Natural convection in a partitioned trapezoidal cavity heated from the side," *Numerical Heat Transfer; Part A*, vol. 43, no. 5, pp. 543–563, 2003.
- [13] M. A. Coman, G. O. Hughes, R. C. Kerr, and R. W. Griffiths, "The effect of a barrier on laminar convection in a box with differentially heated endwalls," *International Journal of Heat and Mass Transfer*, vol. 49, no. 17-18, pp. 2903–2911, 2006.
- [14] H. Oztop and E. Bilgen, "Natural convection in differentially heated and partially divided square cavities with internal heat generation," *International Journal of Heat and Fluid Flow*, vol. 27, no. 3, pp. 466–475, 2006.
- [15] Y. Varol, H. F. Oztop, and T. Yilmaz, "Natural convection in triangular enclosures with protruding isothermal heater," *International Journal of Heat and Mass Transfer*, vol. 50, no. 13-14, pp. 2451–2462, 2007.
- [16] A. AlAmiri, K. Khanafer, and I. Pop, "Buoyancy-induced flow and heat transfer in a partially divided square enclosure," *International Journal of Heat and Mass Transfer*, vol. 52, no. 15-16, pp. 3818–3828, 2009.

- [17] H. C. Brinkman, "The viscosity of concentrated suspensions and solutions," *The Journal of Chemical Physics*, vol. 20, no. 4, pp. 571–581, 1952.
- [18] H. E. Patel, T. Sundararajan, T. Pradeep, A. Dasgupta, N. Dasgupta, and S. K. Das, "A micro-convection model for thermal conductivity of nanofluids," *Pramana—Journal of Physics*, vol. 65, no. 5, pp. 863–869, 2005.
- [19] S. Succi, *The Lattice Boltzmann Equation for Fluid Dynamics and Beyond*, Oxford University Press, Oxford, UK, 2001.
- [20] D. A. Wolf-Gladrow, *Lattice-Gas Cellular Automata and Lattice Boltzmann Models: An Introduction*, Springer, Berlin, Germany, 2000.
- [21] Z. Chai and B. Shi, "A novel lattice Boltzmann model for the Poisson equation," *Applied Mathematical Modelling*, vol. 32, no. 10, pp. 2050–2058, 2008.
- [22] S. Chen, J. Tölke, and M. Krafczyk, "Simulation of buoyancy-driven flows in a vertical cylinder using a simple lattice Boltzmann model," *Physical Review E*, vol. 79, no. 1, Article ID 016704, 2009.
- [23] S. Chen, J. Tölke, and M. Krafczyk, "Simple lattice Boltzmann subgrid-scale model for convectional flows with high Rayleigh numbers within an enclosed circular annular cavity," *Physical Review E*, vol. 80, no. 2, Article ID 026702, 2009.
- [24] J. Quiet, M. Reggio, P. Vasseur, and S. Leclaire, "Application of the lattice Boltzmann method to calculate the natural convection of nanofluids in a shallow cavity," in *Proceedings of the 18th Annual Conference of the CFD Society of Canada*, 2010.
- [25] O. V. Trevisan and A. Bejan, "Natural convection with combined heat and mass transfer buoyancy effects in a porous medium," *International Journal of Heat and Mass Transfer*, vol. 28, no. 8, pp. 1597–1611, 1985.